AN ABSTRACT OF THE DISSERTATION OF

Stephen A. Drake for the degree of Doctor of Philosophy in Ocean, Earth and Atmospheric Sciences presented on April 29, 2016.

Title: An Experimental Investigation of Interstitial Air Movement in Seasonal Snow

Abstract approved:

_____

Chad W. Higgins

Atmospheric pressure changes do not stop at the permeable snow surface but rather propagate into it. These pressure changes range from high amplitude, low-frequency events caused by seasonal cycles and synoptic weather systems to small amplitude, high-frequency events caused by topographic features and turbulence. The effect of pressure changes on interstitial air movement is locally weak but geographically pervasive and temporally persistent so the cumulative impact may be significant over seasonal timescales. Near the snow surface, pressure changes in the high-frequency range caused by turbulence and windflow over topographic features can enhance fluxes of chemically and radiatively active trace species between the snow and atmosphere. Deeper, in multi-year snow that overlays continental ice sheets, low-frequency pressure changes can stimulate air movement. This ventilation process adds complexity for paleoclimate analysis of ice cores to the extent that air trapped in ice has a different age structure than the ice matrix. For decades, investigators have recognized ventilation as a mechanism that enhances mass flux and interstitial air mixing but its effects are indeterminate because the relationship between wind forcing and interstitial air response is poorly constrained.

This dissertation addresses the experimental question: what is the effect of wind on interstitial air movement in snow? To address this question, *in situ* field experiments were designed and performed to measure the depth in seasonal snow affected by wind-generated pressure changes as a function of frequency of the

pressure changes. One experimental result was that high-frequency pressure changes have greater amplitude than theory predicted. At first, this result may seem to indicate that high-frequency pressure changes affect interstitial air motion more than predicted but for another finding that high-frequency pressure changes (perturbations) also attenuate more with depth than current theory predicts. Therefore, strong high-frequency attenuation relegates the effect of high-frequency pressure changes to a very thin air layer near the snow surface. Enhanced perturbation pressure attenuation at high frequencies does not directly address the question of the degree to which low frequencies attenuate with depth. However, the high-frequency mismatch between experimental evidence and theory underscores the necessity for future endeavors to test anticipated low-frequency perturbation pressure attenuation with deep snow pressure measurements.

More accurate measures of the relationship between wind forcing and the spectral response of pressure changes acquired in this series of field experiments enabled characterization of the distribution of perturbation pressure amplitude as a function of frequency and wind forcing. It was found that kinetic energy of the wind as given by the horizontal and vertical components of the wind is a better diagnostic for perturbation pressure than vertical velocity variance. This finding is relevant when parameterizing perturbation pressure forcing using wind characteristics. A simplified model that convolves perturbation frequency with the spectral distribution of amplitude was used to diagnose frequencies for which water vapor flux (sublimation) is maximized for hydrostatic pressure changes. Applying the meteorological conditions measured in the case studies for this experiment sublimation enhancement was maximized for pressure oscillations with period ranging from 5 to 20 minutes. For shorter time periods the amplitude was too small to achieve a threshold (taken as the roughness length) and for longer time periods amplitude was sufficient but the frequency of the oscillation was insufficient to drive much air exchange between the snow and atmosphere.

Finally, interstitial air movement was calculated under various wind conditions by measuring the evolution of a trace gas plume (carbon monoxide) as detected by a network of thin film sensors. Near surface data revealed an advection

signature oriented with the prevailing wind. The plume centroid propagated downwind but upwind dispersion was greater than crosswind dispersion. This dispersion signature is consistent with turbulent eddies that propagate downwind. When the measurement network was oriented in a vertical plane, the center of mass of the plume propagated upwards indicating that upward vertical dispersion was enhanced relative to downward dispersion. This finding indicates that the residence time of a neutrally buoyant gas in the upper portion of the snow column is significantly shorter than the same gas located lower in the snowpack.

An Experimental Investigation of Interstitial Air Movement in Seasonal Snow

by
Stephen A. Drake

A DISSERTATION

submitted to

Oregon State University

in partial fulfillment of
the requirements for the
degree of

Doctor of Philosophy

Presented April 29, 2016
Commencement June 2016

Doctor of Philosophy dissertation of Stephen A. Drake presented on April 29, 2016.

APPROVED:

Major Professor, representing Ocean, Earth and Atmospheric Sciences

---

Dean of the College of Earth, Ocean and Atmospheric Sciences

Dean of the Graduate School

I understand that my dissertation will become part of the permanent collection of Oregon State University libraries. My signature below authorizes release of my dissertation to any reader upon request.

Stephen A. Drake, Author

ACKNOWLEDGEMENTS

For their devotion in time and energy towards helping me complete this dissertation I sincerely thank my principal advisor, Dr. Chad Higgins, and committee members: Dr. Jennifer Hutchings, Dr. John Selker and Dr. Eric Skyllingstad. For his inspiration, insights and initiation in this field of endeavor I thank my academic grandfather, Dr. Marc Parlange. Others who guided me along the way included Dr. Hendrik Huwald, Dr. Michael Lehning, Dr. Noah Molotch, Dr. Christoph Thomas and their students. This dissertation would not have been possible without their contributions. Thanks to Robert Allan and Lori Hartline for their assistance. Thanks to my wife, Dr. Anne Nolin, and son, Seth Drake, for their patience while I pursued an advanced degree. Finally, thanks to my parents for sparking my appreciation of the natural world.

Research conducted for the paper described in chapter 2 was funded by the Laboratory of Environmental Fluid Mechanics and Hydrology at École Polytechnique Fédérale de Lausanne and the Landolt et Cie Endowed Chair for Sustainable Futures, Switzerland. Crans-Montana ski area provided key logistical support during the field campaign. We thank V. Piovano for measuring the relaxation time constant of the pressure reference and Dr. D. Chelton for guidance on the spectral error assessment. We are grateful to Dr. E. D. Waddington and an anonymous reviewer for providing constructive comments that greatly improved the paper.

We thank FXI Corporation for providing the reticulated foam samples that we used to perform the permeability calibrations used in chapter 3. We are grateful to Dr. Noah Molotch for his support during the Colorado campaign that contributed to chapters 4 and 5. We thank Ms. Lisa Dilley (USFS) for coordinating access to Dutchman Flat SnoPark. Thanks to Dr. Ziru Liu and Ms. Rebecca Hochreutener for field assistance.

CONTRIBUTION OF AUTHORS

In Chapter 2, Dr. Hedrik Huwald, Dr. Chad Higgins and Dr. Anne Nolin collected some of the field measurements and edited the scientific paper. V. Piovano measured the time constant for the pressure sink.

In Chapter 3, Dr. Chad Higgins and Dr. John Selker provided technical advice and edited the scientific paper.

In Chapter 4, Dr. Chad Higgins, Dr. Eric Skyllingstad and Jason Kelley edited the scientific paper.

In Chapter 5, Dr. Chad Higgins edited the scientific paper. Dr. John Selker built the snow pickets and provided calibration advice.

TABLE OF CONTENTS

TABLE OF CONTENTS (Continued)

LIST OF FIGURES

LIST OF FIGURES (Continued)

LIST OF FIGURES (Continued)

LIST OF FIGURES (Continued)

LIST OF FIGURES (Continued)

LIST OF TABLES

LIST OF SYMBOLS

Symbol	Units	Description
C	kg-m^{-3}	concentration
D	m^2-s	Diffusion coefficient
e	Pa	vapor pressure deficit
e_a	Pa	actual vapor pressure
e_s	Pa	saturation vapor pressure
f	s^{-1}	frequency
H	m	pressure diffusion length scale
k	m^2	intrinsic permeability
m	kg	mass
M	m-s^{-1}	wind speed
n	dimensionless	number of moles
ϕ	dimensionless	porosity
ρ	kg-m^{-3}	density
P	Pa	pressure
$\bar{p}$	Pa	mean pressure
p_0	Pa	perturbation pressure at snow surface
p_{10}	Pa	perturbation pressure at 10 cm depth
p'	Pa	perturbation pressure
r	m	radial distance
R	J-mol^{-1}-K^{-1}	ideal gas law constant
σ_p	Pa	standard deviation of pressure
σ_{pe}	Pa-s-m^{-2}	flow resistivity
σ_w	m-s^{-1}	standard deviation of vertical wind component
s_f	dimensionless	pore shape factor
t	s	time
t_{MAX}	s	time elapsed to reach maximum concentration
T	K	temperature
τ	dimensionless	tortuosity
U	m-s^{-1}	x-component of velocity
v	m-s^{-1}	velocity
$\tilde{v}$	m^3	volume
V	m-s^{-1}	y-component of velocity
ω	s^{-1}	angular frequency
W	m-s^{-1}	z-component of velocity
μ	Pa-s	dynamic air viscosity
z	m	depth

LIST OF APPENDIX FIGURES

DEDICATION

This dissertation is dedicated to those who wonder.

1 Introduction

This dissertation addresses the experimental question: what is the effect of wind on interstitial air movement in snow? This question is important and broadly relevant because it applies to near-surface, seasonal snow processes as well as deep firn mixing in continental ice sheets. Near the snow surface, wind can enhance mobility and fluxes of water vapor and radiatively and chemically reactive trace species (Thompson, 1995). Increased mobility can enhance water vapor flux (Albert, 2002; Town et al., 2008) and increase efficiency of radiatively important chemical reactions (Hutterli et al., 1999). At depth, it has been postulated that pressure changes spawn air movement, which can confound the age congruence between ice and the air trapped in it (Bales and Choi, 1996; Kawamura et al., 2006; Severinghaus et al., 2010). Paleoclimate analysis of ice cores at low accumulation zones is therefore complicated by an age mismatch between the air bubbles trapped in ice and the ice matrix. Complete answers to these important questions are beyond the scope of this endeavor. Instead, I concentrate on constraining the magnitude of interstitial air movement for a given wind forcing and given snow permeability. Several investigators (e.g. Colbeck 1989, Waddington et al., 1996) have theoretically surmised this relationship and experiments have been attempted but experimental evidence with sufficient precision to test these theories is lacking.

I was introduced to this topic while preparing for an experiment on Plaine Morte Glacier during the 2010-2011 winter/spring season, which was organized by Dr. Marc Parlange's EPFL/EFLUM lab. Our experimental design and deployments leveraged some lessons learned from the previous field season during which Dr. John Selker (Oregon State University) and a post-doc who would later become my advisor, Dr. Chad Higgins, collaborated with EFLUM. As I hope will become clear from the four papers contained in this document, direct experimental data of the stated experimental question are difficult to obtain because we are studying processes that have small instantaneous magnitude at a given locale yet are temporally persistent and geographically pervasive over vast, snow-covered regions. So the integrated

effects of wind forcing on interstitial air movement are relevant for snow-covered regions over seasonal time scales.

In the study of wind interactions with snow technical and theoretical challenges abound. For example, in paper 3 (P3) I describe in detail the mismatch between perturbation pressure measurements and velocity measurements that complicate establishing a clear mathematical relationship between the two. Technological improvements such as improved accuracy of the absolute pressure sensors used in P3 over the relative pressure sensors used in P1 benefited this investigation. However, to compensate for a macroscale version of the Heisenberg Uncertainty principle, that is: if you put a probe in it then you change the thing you are measuring - we strove to design these experiments such that we could discern the relevant signal from the effect of the given probe and from background noise.

In P1 and P3 we measured the effect of wind on spectral pressure changes in snow. P1 was written based on data acquired during the Plaine Morte 2010-2011 experiment. We quantitatively documented the spectral dependency of perturbation pressure attenuation with depth, however, snow layering complicated the result. The analysis given in P3 is based on measurements using fewer (4 rather than 28) but higher precision absolute pressure sensors in deployments during the 2013-2014 and 2014-2015 seasons at Hogg Pass, Oregon, Dutchman Flat, Oregon and Storm Peak Lab, Colorado. For these deployments we generally monitored single homogenous snow layers to minimize complications due to snow layering.

Snow permeability is an important parameter when considering how wind affects interstitial air movement in snow. Surface permeability is particularly important because it regulates the amplitude of pressure waves that propagate through the snowpack. However, measuring snow permeability is an experiment in itself that is fraught with sampling errors such as fracturing and representativeness of pint-sized samples. We therefore developed a low-cost acoustic permeameter to give expedited measurements of surface snow permeability and describe this system in P2.

Wind and pressure are tightly bound such that it is often difficult to deconvolve the effect of one from the other. In the atmosphere, air motions spawn pressure changes, which, in turn, induce changes in the wind field. So when the wind

blows over the snow it is not intuitively obvious whether wind shear directly generates interstitial air movement through molecular momentum transfer or whether wind shear spawns pressure gradients, which, in turn, induce interstitial air movement. Clifton et al. (2008) found that wind shear directly affects only the top few millimeters of a highly permeable snow proxy. This result suggests that pressure gradients rather than molecular transfer drive interstitial air movement. If this is the case then the pressure field in the snow should define the speed and direction of Darcian flow, which may be contrary to the prevailing wind direction. We further investigate the linkage between above snow wind speed and interstitial air motion within the snow by correlating wind speed above the snow with the in-snow concentration evolution of carbon monoxide tracer releases in P4.

Each of the four papers that comprise this dissertation is presented as a separate chapter. The following preambles detail relevant introductory information not contained in the four scientific papers. Field notes for the Plaine Morte and Storm Peak Lab experiments are documented in separate web pages. Details for the Hogg Pass and Dutchman Flat experiments are contained in a separate PDF document, 'FieldReport_SPE_2014.pdf'. These notes are important for documentation but are separated from this document for brevity.

1.1 Preamble to Paper 1

Snow is a permeable medium so mass, momentum, and energy can propagate through it. For example, as a synoptic high-pressure system builds into a region of interest the atmospheric column compresses and some of the air that was formerly above the snow is compressed into the snow. Then, as the high-pressure system weakens and low pressure develops in the region of interest the atmospheric column relaxes and some of the air that formerly resided in the snow translates into the atmosphere. In this manner, successive changes in atmospheric pressure cause the snow to "breathe". If we consider a simplified example similar to that given in Colbeck (1989), hereafter referred to as CB89, in which the air above the snow is isothermal and we imagine an adjustable mass on top of an atmospheric air column to

simulate atmospheric pressure changes, then the air column will expand and contract by Boyle's Law:

$$P_1\tilde{v}_1 = P_2\tilde{v}_2 \;\rightarrow\; \tilde{v}_2 = \frac{P_1\tilde{v}_1}{P_2} \qquad (1.1)$$

where the subscripts indicate initial and final states of pressure (P) and volume ($\tilde{v}$). (Note: see also the list of symbols in the pre-text pages of this document.) Plugging in approximations that span a realistic range of synoptic pressure changes we have:

$$\tilde{v}_2 = \tilde{v}_1 \frac{1030mb}{990mb} = 1.04\,\tilde{v}_1 \qquad (1.2)$$

So the pressure and volume of air in the snow will change by upwards of 4% between high and low pressure systems. For small changes in pressure and height, air density and gravity can be considered constant so the hydrostatic equation dictates that a 4% change in pressure equates to a 4% change in the thickness of the air layer in snow:

$$dP = -\rho g\, dz \;\rightarrow\; \frac{dP}{dz} = const \qquad (1.3)$$

For a 1-meter snowpack a 4% depth change corresponds to only a 4 cm change in the hydrostatic depth of the air column. A rough estimate for the water vapor lost in one 3-day synoptic cycle for a 4-cm deep air layer with 50% relative humidity at 0 °C is given by the Clausius-Clapyron and ideal gas equations. The vapor pressure deficit of the air layer above the snow in this case is:

$$e = e_s - e_a = 6.11mb - (0.5)(6.11mb) \approx 3mb \qquad (1.4)$$

where we have assumed that the interstitial air is saturated per Pomeroy & Brun (2001). A mid-density snowpack of 250 kg-m^3 has porosity ~ 0.7 so the number of moles within the 4-cm column over a 1 m^2 area is:

$$n = \frac{\phi e \tilde{v}}{RT} = \frac{(0.7)(300\ Pa)(0.04\ m^3)}{(8.314\ J - mol^{-1} - K^{-1})(273\ K)} = 3.70\ x\ 10^{-3} mol - m^{-2} \quad (1.5)$$

This gives a mass of:

$$\frac{mass}{area} = (3.70\ x\ 10^{-3} mol - m^{-2})(18\ g - mol^{-1}) = 6.66\ x\ 10^{-2} g - m^{-2} \quad (1.6)$$

and a vapor loss rate of:

$$\frac{6.66\ x\ 10^{-2} g - m^{-2}}{3\ days} \approx 2\ x\ 10^{-2} g - m^{-2} day^{-1} \quad (1.7)$$

where we assumed a generously fast synoptic time scale change of three days. At this rate, it would take:

$$\frac{250\ x\ 10^3\ g - m^3}{(2\ x\ 10^{-2} g - m^{-2} - day^{-1})(365\ day - yr^{-1})} \approx 34{,}246\ years \quad (1.8)$$

or ~ 34,000 years for a moderately dense 1-m deep snowpack to sublimate by this process. So, synoptic hydrostatic changes have a negligible effect on vapor exchange.

The maximum depth of snow/firn is on the order of 70 m (Dr. Christo Buizert, personal communication) so, using the 4% estimate, an air column would translate up to ±2.8 m vertically in deep snow/firn. This vertical displacement is not sufficient to account for the mixing depths calculated for high wind, low accumulation zones in Antarctica. For example, by comparing the ratio of nitrogen isotopes with that expected for diffusion, Kawamura et al. (2006) inferred convective depths of greater than 8 meters for two such sites (Fuji Dome and YM85). At a megadunes site in Antarctica, Severinghaus et al. (2010) found a convective depth of 23 m, which they

attributed to wind-aided ventilation and cracks in the ice matrix that enabled deep air movement.

These examples show that hydrostatic pressure changes at synoptic frequency lack sufficient amplitude either to enhance sublimation rate from surface snow or to account for observed interstitial air mixing in deep snow/firn. However, it is not intuitively clear what effect wind and pressure changes would have on surface sublimation rate or deep air movement when the air in snow responds slower than atmospheric pressure changes and thus is no longer hydrostatic. This condition is referred to as "windpumping". We note that while some authors generically refer to wind effects on interstitial air as windpumping, in this manuscript we adopt a narrower definition that excludes hydrostatic effects.

The depth below which windpumping occurs depends on the frequency of pressure changes and permeability of the snow. Synoptic pressure changes are slow enough that air in near-surface, permeable snow "breathes" and remains in hydrostatic balance with the surface pressure gradient. But permeability decreases with depth so at some depth the permeability is too low for air movement to keep up with surface pressure changes. As the frequency of surface pressure changes increase, the depth at which air movement cannot maintain hydrostatic balance decreases.

Both CB89 and Waddington et al. (1995), hereafter referred to as WD95 deduced that windpumping could be modeled as a diffusive process. By combining Darcy's law, mass continuity and the ideal gas law one can form a linearized approximation for airflow in porous media:

Darcy's Law: $$v = -\frac{k}{\mu}\frac{\partial P}{\partial \mathrm{z}} \qquad (1.9)$$

Mass continuity: $$\frac{\partial (\rho v)}{\partial z} + \phi \frac{\partial \rho}{\partial \mathrm{t}} = 0 \qquad (1.10)$$

Equation of state: $$P = \rho RT \quad (1.11)$$

Combining these three equations we have:

$$\frac{1}{RT}\left[\frac{k}{\mu}\frac{\partial}{\partial z}\frac{P\partial P}{\partial z}\right] = \frac{\phi}{RT}\frac{\partial P}{\partial \mathrm{t}} \quad (1.12)$$

Linearizing and simplifying:

$$\frac{k}{\mu\phi}\left[\frac{\partial}{\partial z}\left((\bar{p}+p')\left(\frac{\partial(\bar{p}+p')}{\partial z}\right)\right)\right] = \frac{\partial(\bar{p}+p')}{\partial \mathrm{t}} \quad (1.13)$$

$$\frac{k}{\mu\phi}\left[\frac{\partial}{\partial z}\left(\frac{\bar{p}\partial\bar{p}}{\partial z}\right)+\frac{\partial}{\partial z}\left(\frac{\bar{p}\partial p'}{\partial z}\right)+\frac{\partial}{\partial z}\left(\frac{p'\partial\bar{p}}{\partial z}\right)+\frac{\partial}{\partial z}\left(\frac{p'\partial p'}{\partial z}\right)\right] = \frac{\partial\bar{p}}{\partial \mathrm{t}}+\frac{\partial p'}{\partial \mathrm{t}} \quad (1.14)$$

$$\frac{k\bar{p}}{\mu\phi}\left[\frac{\partial^2 p'}{\partial z^2}\right] = \frac{\partial p'}{\partial \mathrm{t}} \quad (1.15)$$

Both CB89 and WD95 solve Eq. (1.15) but apply different boundary conditions thus deriving different solutions. CB89 assumes a thin snow layer whereas WD95 assumes an infinitely deep layer. Both authors draw their solutions to this differential equation from "Conduction of heat in solids" by Carslaw and Jaeger (1959).

In the first paper in this thesis (P1) we compare the solutions from CB89 and WD95 with near surface pressure measurements. These high-frequency pressure measurements are the first measurements that show how both static pressure and perturbation pressure attenuate with depth in snow. The vertical profile of static pressure delineates the depth in snow that is affected by quasi-static circulation patterns that develop as wind blows over surface roughness features. The vertical

profile of perturbation pressure shows the amplitude and spectral distribution of turbulently generated perturbation pressure that is available to induce interstitial air movement. Strictly speaking, the WD95 solution does not apply to the seasonal snow that we measured yet it yields an instructive comparison. We assume snow depth is large relative to the wavelength of the surface feature and thereby ignore the degenerate case of longwave surface features over a shallow snowpack.

1.2 Preamble to Paper 2

In the Plaine Morte Experiment described in paper 1 (P1), we utilized an empirical formula to derive a time series of snow permeability from snow grain characteristics measured in snowpits. These derivations yielded permeability profiles that were qualitatively consistent but the values were systematically low compared with previously published results (Sommerfeld and Rocchio, 1993; Arakawa et al., 2009). Also, snowpits are time consuming to analyze and consume precious time that could otherwise be used acquiring other measurements. We concluded that we needed a more expedient measure of snow permeability in order to establish a quantitative relationship between atmospheric state and interstitial air response in snow. Besides the empirical method that we used in the Plaine Morte experiment, other methods of determining snow permeability involve either direct measurement with a flow-through permeameter or casting and subsequent scanning of small (~ 1 liter-sized) samples.

Lacking the manpower that would be required to obtain permeability measurements by standard means for each deployment we therefore contemplated an alternate method. After reviewing the literature (see P2) and testing alternatives we concluded that we could infer permeability from the acoustic backscatter at frequencies between 50Hz and 2000Hz. We accept the tradeoff of a more timely volume-averaged measure of permeability over a more precise but perhaps less representative measurement given by a flow-through permeameter or tomography.

1.3 Preamble to Paper 3

With improved methods of measuring snow permeability and the in-snow response to wind forcing we return to the question: to what degree does turbulence above the snow induce pressure changes in the snow? When meteorological conditions allowed, the acoustic permeameter described in P2 was used to characterize surface snow permeability. Additionally, we used four high precision, Paroscientific (model 216B) absolute pressure sensors rather than 28 relative pressure sensors used in P1. Notably, these absolute pressure sensors did not require a pressure reference (sink) and measured pressure with sufficient precision that sub-Pascal fluctuations were resolvable. This capability eliminates potential error introduced by a pressure reference that smooths the amplitude of lower frequency pressure changes and enabled us to resolve lower frequency pressure changes than was possible with relative pressure sensors. What we sacrificed in vertical resolution with 28 relative pressure sensors was compensated for with precision of the absolute pressure sensors.

Whereas in the Plaine Morte experiment described in P1 we synthetically amplified the perturbation pressure field by exposing the top portion of snow pickets to the wind field, in this experiment we did not use snow pickets so that we could attempt to measure the natural, turbulently generated perturbation pressure field. This allowed us to directly relate wind forcing (e.g. speed, vertical velocity variance) with in-snow pressure perturbation amplitude and frequency. With these measurements we could infer how the amplitude and frequency of hydrostatic pressure changes could enhance water vapor flux from the snow into the atmosphere.

1.4 Preamble to Paper 4

In P1 and P3 we verified that wind stimulates fluctuating pressure gradients in snow that cause air movement through pore space. Air motions considered in these two papers was oscillatory. In P4, we examine the possibility that wind forcing enhances in-snow dispersion by a rate that is greater than would be expected if diffusion were the only process at work. Bowling and Massmann (2011) found enhanced diffusion of CO_2 through snow and attributed this enhancement to wind.

But the wind-driven process or processes that drove this enhanced diffusion was not identified.

In a wind tunnel experiment using reticulated foam as a proxy for snow, Clifton et al. (2008) found that the effect of shear above the snow does not propagate further than a few millimeters into the snow. If this is the case, then a shear-driven molecular transfer would be inhibited with depth and preferential above-snow wind direction would affect interstitial Darcian flow only within a thin layer of surface snow. This result does not preclude the possibility that in-snow pressure gradients could drive Darcian velocity with a preferred direction. But a flat surface lacks a forcing mechanism to generate in-snow pressure gradients.

When we compare processes that mix particles in the free atmosphere with the same processes acting in a permeable medium, we find some analogs and some distinct differences. As in the free atmosphere, isotropic molecular diffusion spreads a plume in all directions but the center of mass remains in the same place over time. Advection translates the mass centroid but does not spread out the plume in the free atmosphere. However, advection through a permeable medium such as snow can enhance plume spreading by mechanical dispersion as particles translate through tortuous pathways. Eddy diffusion disperses a plume much faster than molecular diffusion in the atmosphere but turbulence is lacking in snow except for perhaps over a thin surface layer.

Because some of these processes exhibit different behavior in the snow and atmosphere, we cannot directly translate results acquired in atmospheric flows to flow through a porous medium. Therefore, in P4 we correlate the movement of carbon monoxide (CO) releases with snow and wind properties. We determine the affects of different processes by comparing the measured plume evolution with model simulations. Since different processes affect plume evolution differently, we isolate the effect of a given process in model simulations.

A complete form of the solution to the advection/diffusion equation in three dimensions can be written as:

$$C(x,y,z,t) = \frac{M}{4\pi t\sqrt{4\pi t D_x D_y D_z}} \exp\left[-\frac{\left((x-x_1)-Ut\right)^2}{4tD_x} - \frac{((y-y_1)-Vt)^2}{4tD_y} - \frac{((z-z_1)-Wt)^2}{4tD_z}\right] - kU - kV - kW \quad (1.16)$$

If we assume that in the snow the eddy diffusion and vertical advection are negligible and we orient the reference system with the wind direction we can form a uni-directional solution to the advection/diffusion equation:

$$C(x,y,z,t) = \frac{M}{4\pi t\sqrt{4\pi t D_x D_y D_z}} \exp\left[-\frac{\left((x-x_1)-Ut\right)^2}{4tD_x} - \frac{(y-y_1)^2}{4tD_y} - \frac{(z-z_1)^2}{4tD_z}\right], \quad (1.17)$$

which describes the dispersion of a point source of mass M. We simplify Eq. (1.17) by defining variables A and B:

let $A = \frac{M}{4\pi\sqrt{4\pi D^3}}$ and $B = \frac{1}{4D}$

$$C = \frac{A}{t^{3/2}}\, exp\left[-Bt^{-1}[((x-x_1)-Ut)^2 + (y-y_1)^2 + (z-z_1)^2]\right] \quad (1.18)$$

taking the derivative w.r.t. time:

let $D = \left[-Bt^{-1}[((x-x_1)-Ut)^2 + (y-y_1)^2 + (z-z_1)^2]\right]$

At peak concentration, the derivative of the concentration is zero:

$$\frac{dC}{dt} = \frac{d}{dt}\left\{\frac{A}{t^{3/2}}\ exp[D]\right\} = 0 \qquad (1.19)$$

$$\begin{aligned}\frac{dC}{dt} = & -\frac{3A}{2t^{5/2}}exp[D] + \frac{A}{t^{3/2}}\exp[D]\frac{dD}{dt} = -\frac{3A}{2t^{5/2}} + \frac{A}{t^{3/2}}\ \frac{dD}{dt} \\ & = -\frac{3}{2t} + \frac{dD}{dt}\end{aligned} \qquad (1.20)$$

We can solve for the derivative for the geometric portion of the equation:

$$\begin{aligned}\frac{dD}{dt} = Bt^{-2}[\big((x - x_1) - Ut)^2 + (y - y_1)^2 + \ (z - z_1)^2\big] \\ - Bt^{-1}[2((x - x_1) - Ut)(-U)]\end{aligned} \qquad (1.21)$$

$$\begin{aligned}\frac{dD}{dt} = Bt^{-2}[((x - x_1)^2 - 2Ut(x - x_1) + \ U^2t^2 + (y - y_1)^2 \\ + (z - z_1)^2] - Bt^{-1}[2(-U)((x - x_1) - Ut)]\end{aligned} \qquad (1.22)$$

$$\frac{dD}{dt} = Bt^{-2}[(r^2 - 2Ut(x - x_1) + \ U^2t^2\ ] + 2UBt^{-1}(x - x_1) - 2BU^2)] \qquad (1.23)$$

$$\frac{dD}{dt} = Bt^{-2}r^2 - 2UBt^{-1}(x - x_1) + BU^2 + 2UBt^{-1}(x - x_1) - 2BU^2)] \qquad (1.24)$$

$$\frac{dD}{dt} = Bt^{-2}r^2 \ \cancel{- 2UBt^{-1}(x - x_1)} + \cancel{BU^2} + \cancel{2UBt^{-1}(x - x_1)} - \cancel{2}BU^2)] \qquad (1.25)$$

$$\frac{dD}{dt} = Bt^{-2}r^2 - BU^2 \quad (1.26)$$

Substituting (1.26) into (1.20) we can solve for the advection speed of air in the interstitial snow:

$$\frac{dC}{dt} = -\frac{3}{2t} + Bt^{-2}r^2 - BU^2 = 0 \quad (1.27)$$

$$U^2 = -\frac{3}{2tB} + \frac{r^2}{t^2} = \frac{-6D}{t} + \frac{r^2}{t^2} = \frac{r^2 - 6D}{t^2} \quad (1.28)$$

$$U = \frac{\pm\sqrt{r^2 - 6Dt}}{t} \quad (1.29)$$

If wind speed is zero, we can solve this equation for the predicted time span required to reach maximum concentration:

$$t_{MAX} = \frac{r^2}{6D} \quad (1.30)$$

Application of Eq. (1.30) to a case for which the wind speed is non-zero would yield an enhanced streamwise diffusion coefficient. Following similar reasoning, non-zero wind in the horizontal plane gives an analogous solution:

$$\sqrt{U^2 + V^2} = \frac{\pm\sqrt{r^2 - 6Dt}}{t} \quad (1.31)$$

We can compare this result with measurements to infer the relative effect of molecular diffusion and advection. One advantage of this method is that it does not

rely upon accurate concentration measurements; only the time required to reach maximum concentration is relevant.

Other processes modify the measured dispersion from that expected using this derivation. For example, vertical diffusion tends to increase towards the snow surface as density decreases, causing molecular diffusion rate to increase towards the surface. Eddy diffusion caused by turbulence above the snow surface has a non-zero effect in a thin layer of snow near the snow surface. Additionally, mechanical dispersion manifested as divergence of a plume as it meanders through a tortuous media increases dispersion rate. All of these processes will not only change the mass available in a horizontal plane but also change the horizontal gradient and feedback to change the horizontal dispersion rate. These processes will affect the perceived center of mass when viewed through the lens of a horizontal measurement network.

We track the position of the center of mass relative to the release position to measure the effect of wind direction on plume movement. The center of mass of plume in a Cartesian plane coordinate system can be approximated from mass-weighted point measurements:

$$\bar{x} = \frac{1}{M}\sum_i m_i x_i\,, \qquad \bar{y} = \frac{1}{M}\sum_i m_i y_i \tag{1.32}$$

If advection is sufficiently robust then an advection signature may be detectable even though these competing processes are modifying plume dispersion in different ways.

In P4, we use the following mass-weighted RMS error as a measure of plume dispersion in the horizontal plane:

$$\hat{\sigma} = \frac{1}{M}\sqrt{\sum_i m_i^2[(x_i - \bar{x})^2 + (y_i - \bar{y})^2]} \tag{1.33}$$

2 Attenuation of wind-induced pressure perturbations in alpine snow

Attenuation of wind-induced pressure perturbations in alpine snow

Stephen A. Drake[1], Hendrik Huwald[2], Marc B. Parlange[3], John S. Selker[1], Anne W. Nolin[1], Chad W. Higgins[1]

[1]Oregon State University, Corvallis, OR, United States
[2]École Polytechnique Fédérale de Lausanne, Lausanne, Switzerland
[3]University of British Columbia, Vancouver, Canada

Accepted for publication: Feb 15, 2016

Journal of Glaciology

2.1 Abstract

Windpumping has been identified as a process that could potentially enhance sublimation of surface snow at high forcing frequency and spawn air movement deeper in firn at lower frequencies. We performed an experiment to examine the relationship between high-frequency wind and pressure measurements within the top meter of an alpine snowpack and compared experimental results with two theoretical predictions. We find that both theoretical predictions underestimate high-frequency perturbation pressure attenuation with depth in the near-surface snowpack and the discrepancy between theory and measurement increases with perturbation pressure frequency. The impact of this result for near-surface snow is that potential enhanced sublimation will occur over a shallower snow depth than these two theories predict. Correspondingly, interstitial air mixing at depth in firn will be driven by lower frequencies than these two theories predict. While direct measurement of these energy-rich lower frequencies is beyond the scope of this paper, stationary pressure measurements validate the presence of a pressure field that could drive near-surface circulation.

2.2 Introduction

Sculpted formations such as sastrugi give visual clues to the nature of wind blowing over a snow surface yet the effects of ventilation beneath the snow surface remain poorly understood. Vetted theories describe how ventilation could potentially enhance sublimation from surface snow and also stimulate air movement at depth. For example, Albert (2002) modeled topographically induced snow ventilation in a megadunes site in Antarctica, simulating quasi-stationary pressure patterns and vapor flux that formed zones of preferential sublimation and deposition beneath the snow surface. In a wind tunnel experiment, Sokratov & Sato (2000) attributed airflow through the snow pore space to turbulence although others have cast doubt on the role of turbulence in producing interstitial air movement (Clifton and others, 2008; Bartlett and others, 2011). More recently, Bowling and Massman (2011) examined CO_2 flux through seasonal snow cover and correlated enhanced diffusion of stable isotopes with windpumping, a process that can enhance gaseous transport through the

snow when pressure changes occur faster than the in-snow air movement response. However, in a laboratory vapor diffusion study Pinzer and others (2012) attributed sublimation and deposition rates across a snow sample to temperature gradients and suggested that wind-enhanced sublimation does not occur through a snow layer. Both Kawamura and others (2006) and Severinghaus and others (2010) suggested that windpumping might account for deeper than expected convection zones in polar firn. Taken together, these studies suggest that pressure differences across several scales of motion spawn air movement in the snowpack but with a great degree of uncertainty in magnitude and effect.

When modeling in-snow response to ventilation Colbeck (1989, hereafter referred to as CB89) and Waddington and others (1996, hereafter referred to as WD96) hypothesized an exponential decrease in perturbation pressure with depth, reaching zero amplitude at the lower boundary. These upper and lower boundary conditions constrain the modeled perturbation pressure field as well as the vertical profile of Darcian flow over the entire depth of the snowpack. In this paper, we test the CB89 and WD96 1-D models using field-based measurements in which we examine the degree to which wind-induced pressure perturbations attenuate with depth in snow. These results provide insights into how perturbation pressure energy is delivered to the snowpack, and they help constrain the depth within which ventilation can stimulate air movement within the snowpack.

2.3 Method

2.3.1 Site Description

We performed *in situ* measurements of wind forcing and pressure response on Plaine Morte Glacier, Switzerland over the course of several weeks during early spring 2010. Plaine Morte Glacier is the largest plateau glacier in the European Alps (Huss and others, 2013) with an extent of ~ 5 km × 2 km and elevation, 2750 m. This site, part of the Crans-Montana ski area, has been used for several previous surface-atmosphere (Bou-Zeid and others, 2010; Huwald and others, 2012) and hydrologic (Finger and others, 2013) experiments. Seasonal snow typically overlies bare ice because net ablation in recent years has exhausted the firn layer. Plaine Morte Glacier

is on average ~ 100-m thick, 15-20 m near the glacier edge and up to 200 m at its center. Over the 6 week course of the experiment, the seasonal snowpack ranged in depth from 3 to 4 m at the instrument site. Prevailing wind measurements acquired from a wind vane and cup anemometer over a 3-week period from late February through mid-March informed a deployment footprint. The upwind fetch had a generally smooth surface with a gently rising inclination of several degrees punctuated by a ridgeline roughly 2 km upwind (Fig. 2.1).

2.3.2 Measurement method

To capture *in situ* measurements of pressure perturbations at known depths in the snow we fabricated four 1-m long wedge shaped snow "pickets" into which we embedded fittings with 10-25 cm spacing (Fig. 2.2). To each fitting we permanently fixed silicone tubing that was strung along the picket center and out the top of the picket (Fig. 2.3). The other tubing end was attached to a differential pressure transducer each time a deployment was initiated. Elliot's (1972) data and previous experience dictated the need for pressure transducers with fast response. Additionally we required a pressure sensor that spanned a range of tens of Pascals with measurement precision better than 1 Pa. For this purpose we employed Setra™ Model 264 differential pressure transducers, designed to operate with an accuracy of 1% full scale at temperatures ranging from -18 °C to 65 °C. Full-scale differential pressure measurements from -25 to +25 Pa were output as voltages ranging from 0 to 5 VDC. Laboratory tests revealed thermal drift somewhat larger than the advertised value of 0.033% full scale $°F^{-1}$ (= 0.06% full scale $°C^{-1}$), highlighting a need to perform in-field base calibration.

In all, 28 pressure transducers were mounted on aluminum rails and placed in a plastic storage container for protection from the elements during data acquisition, and to facilitate transport. The pressure transducers on pickets 1 and 2 had been used in a previous study and had experienced some wear. Results between the older and newer pressure sensors qualitatively agreed but the data scatter was greater for the older sensors. We therefore used measurements from pickets 1 and 2 for qualitative assessment only.

Before placing the pickets into the snowpack, we vertically inserted a thin aluminum plate against two support pipes into the snow. Each picket was then placed vertically with the side opposite the tubing ports positioned firmly against the aluminum plate. This configuration maintained the picket's vertical orientation and provided torque to continuously press the slightly tapered picket face against the snow, thus minimizing the likelihood of air pockets forming around the picket perimeter during placement. Once the snow pickets were in place, we positioned a Campbell Scientific CSAT3 sonic anemometer ~ 30 cm above the snowpack surface with respect to the center of the measurement volume and in close proximity to the snow pickets to characterize near-surface atmospheric turbulence (Fig. 2.3). This close proximity between the sonic anemometer and snow pickets was intended to maximize the coherence of turbulent structures detected by the sonic anemometer and pressure transducers. We acquired pressure transducer and sonic anemometer data at 10 Hz using a Campbell Scientific CR5000 data logger.

2.3.3 Reference Pressure

A differential pressure transducer measures the pressure difference between two points. Thus, a common reference is a critical requirement to inter-compare values collected from differential pressure transducers. The Setra 264 pressure transducer has two ports, which we refer to as the 'low' or reference port and a 'high' or measurement port. The low port of each differential pressure transducer was attached to a single common reference. Pressure perturbations were measured as the pressure difference between the reference (low port) and the high port. An ideal common reference removes pressure perturbations at the low port of each pressure transducer, thereby establishing a shared baseline such that high-port pressure measurements may be directly compared amongst different pressure transducers. The common reference was constructed as a double-walled vessel filled with small, irregularly shaped pieces of high-density foam to dampen in-container velocity and pressure fluctuations. The low-port tubing passed into the inner vessel with one pinprick hole providing air passage between the inner vessel and the outer vessel and a second pinprick hole connecting the outer vessel with the environment to minimize

high-frequency pressure changes while allowing for gradual, synoptic scale equilibration, which could otherwise easily exceed the full scale of the pressure transducers.

For each deployment the reference pressure chamber was placed in the same container as the logger, thus high-pass filtering free-atmospheric pressure changes. We measured the relaxation time constant for the pressure chamber in a laboratory environment to minimize noise due to turbulence. The relaxation time was measured by injecting a known volume of air (0.5 mL) through a 1-m long stainless steel capillary (to reduce heating) into the reference chamber port that would normally connect to the low port of the pressure transducers. We noted an exponential decay in pressure as the reference chamber responded to this imposed pressure perturbation. The relaxation time was taken as the time required for the measured pressure to decay to 0.37 (or e^{-1}) of the imposed pressure and was found to be 75 s ± 5s. This timeframe is short enough to respond to synoptic changes yet long enough to resolve high-frequency pressure changes. We cannot resolve the magnitude of pressure changes with frequency on the order of or below the chamber relaxation time because the reference chamber will equilibrate over the timespan of the fluctuation and synthetically dampen the measured response. Our setup is therefore tuned to measure high-frequency pressure responses. Changes to the relaxation time under changing environmental conditions were an unmeasured potential source of error.

2.4 Results

2.4.1 Snow State

To determine snowpack structure, we excavated a snowpit down to no less than 1-m depth and horizontally within 10 m of the snow picket location in each pressure picket deployment. Snowpits were excavated after the snow pickets had been placed; the pressure data acquired during snowpit excavation were not used in this analysis. We acquired vertical profiles describing layering, crystal properties, temperature and density to characterize the snow pack. The time/height cross-section in Fig. 2.4 summarizes the evolution of derived intrinsic permeability from Shimizu's (1970) formula for specific permeability ($B_0 = 0.077\ d_0^2 \exp\left[-7.8\ \rho_s^*\right]$, where $d_0$is

the grain diameter and ρ_s^* is the specific gravity of snow with respect to ice) over the time range of case studies. From literature reviews we expected that intrinsic permeability empirically derived using Shimizu's formula would yield calculated values in the range, 10^{-8} to 10^{-10} m^2. However, Shimizu's formula applied to our measurements gave permeability values down to 10^{-12} m^2 in deeper, denser snow. Clearly, Shimizu's formula yielded systematically low permeability values as snow density increased with depth. As Shimizu (1970) and Albert and others (2000) noted, the topology of the snow matrix evolves to a state that no longer complies with the fundamental assumption of packed spheres, rendering his formula inappropriate. To compare our results with the theoretical models of CB89 and WD96 we assume a constant intrinsic permeability of 10^{-9} m^2, which was a representative near-surface value over the course of the experiment (bold isopleth in Fig. 2.4). We present this result to underscore the notion that intrinsic permeability varied substantially over small changes in space and time at our experiment site.

2.4.2 Deployments

Between 16 March and 17 April 2010 we deployed our snow picket/sonic anemometer system 12 times for periods ranging from 3 to 44 h. Given that site access was available only when the Crans-Montana ski lifts were operating, most data were acquired during times between when the ski area opened in the morning and when it closed for the day. Six of the twelve deployments passed quality control constraints for time and wind directional continuity. We required consistent data intervals to accurately compute high-frequency correlations and for spectral analysis. Therefore, we did not use data that would have necessitated gap filling. Wind direction continuity was required because the relative pressure systematically changed with attack angle on a given picket. For example, wind forcing and in-snow pressure response at 100 cm depth shown between midnight on 12 April and midnight on 13 April in Fig. 2.5 indicate that relative pressure magnitude changed sign at noon when the wind direction changed from southeasterly to northerly. So when the wind direction varied substantially we could not discriminate between the influence of

wind speed and wind direction on the relative pressure measured within the snow. We further describe the objective criteria for wind direction selection later.

To facilitate references to particular deployments that met quality control constraints we define reference indices for the six deployments in Table 2.1.

2.4.3 Calibration

As noted earlier, the baseline voltage for each pressure transducer changed in a non-systematic stepwise manner at the initiation of each deployment when the pressure reference was engaged. Differences in hydrostatic pressure between the pressure reference and pressure measurements at difference depths in the snow also introduced a pressure offset. The baseline voltage was therefore defined such that measured pressure changes asymptote to zero with wind speed. The method of finding this baseline offset for each pressure transducer is delineated below in the section, “Stationary Pressure Response to Wind Forcing”. It could be argued that pressure changes will not be zero even at zero wind speed; however, this degree of precision is below the measurement capability of the pressure sensors used in this experiment.

2.4.4 Experimental Error

At the end of the first deployments we dug out the snow pickets to inspect picket air intake ports for icing and to verify that there was minimal air space around each picket by which pressure signals could bypass the snow medium and pass directly from the atmosphere into the pressure transducer intake (Fig. 2.6). By correlating visual inspections with pressure measurements we determined that leakage around a picket was only an issue for near surface ports (10 cm and 20 cm depth) in the later stage of longer deployments as snow melted, eroded or sublimated away from the picket face. This process manifested in the data as an apparent increase in perturbation pressure response to a given wind forcing and was thus marked as unreliable data. Icing of ports on the pickets was another source of experimental error. Snow could become impacted into a picket air intake port during placement, or an intake port could ice over during a data-acquisition period. In this event, the

variance in pressure measurements from iced ports had very low correlation with wind speed changes and was easily identifiable. Snow impaction/icing was a common source of experimental error that reduced the quantity of high quality data collected below 50 cm depth. For data collected at 10 cm, 20 cm, 30 cm, 40 cm, 50 cm, 75 cm and 100 cm depths, corrupted data accounted for 5%, 5%, 0%, 17%, 33%, 33% and 33% of the case data, respectively.

2.4.5 Stationary Pressure Response to Wind Forcing

We refer to stationary pressure as the relative pressure field that developed in response to constant wind blowing over a barrier, and we distinguish it from the perturbation pressure, which is variability in the pressure field caused by variations in wind forcing. CB89 and Albert (2002) theorized that topographic features generate a stationary pressure field that drives near-surface circulations in snow. To confirm the presence of a stationary pressure field we first needed to calibrate the baseline pressure for each pressure sensor for all six case studies in Table 2.1 such that we could inter-compare results between cases. Constant topographic forcing is simulated by flow distortion over 10 cm of exposed snow picket as shown in Figs. 2.2 and 2.3. To maximize the forcing/response signal, we removed the directional dependence of stationary pressure amplitude by excluding data greater than 5° from the prevailing wind direction. The wind direction relative to the picket face was not necessarily known to a precision of ±5°so we derived the optimal wind direction by iteration, choosing the orientation that gave highest stationary pressure response to wind-speed forcing.

Pressures were then bin-averaged in 0.25 m s^{-1} wind speed increments to determine a characteristic curve for each observation period defining the stationary pressure response to the wind forcing as well as the standard deviation, which defined the perturbation pressure response. Fig. 2.7 shows an example of the underlying data and the resulting characteristic curve for 18 March.

Inspired by the quadratic relationship between pressure and velocity in Bernoulli's equation, we fit a quadratic curve to the data and also tried linear and exponential curve fits. The curve fit was used to extrapolate wind speed to the y-

intercept. We found the R^2 value was maximized with an exponential fit when applying the constraint that relative pressure must be minimized at zero wind speed. Without this constraint a given quadratic fit could have a higher R^2 and also exhibit non-physical behavior that the relative pressure at zero wind speed could be greater than the relative pressure at non-zero wind speed. The difference between an exponential curve fit and a quadratic curve fit was typically small (< 1 Pa) but was larger for cases for which the quadratic fit was poor. In subsequent analysis we ignore results at the upper limit of the data range where we had insufficient data to resolve a characteristic curve.

Once the relative pressure at which wind speed asymptotes to zero was determined for all six cases, the y-intercept was subtracted from the y-coordinate (pressure) of the bin-averaged center points. This procedure defined a common origin and allowed us to overlay case results. A flowchart delineating steps in this procedure is shown in Fig. 2.8. Wind speed versus stationary pressure for all cases are compiled in Fig. 2.9 revealing a similar pressure response curve for each case. The general trend is that of an exponential response at low wind speed, transitioning to a linear response at higher wind speed. Largest stationary pressures were typically found closer to the snowpack surface as can be seen by the 5-cm deep measurement in Fig. 2.9. This is the only case with a 5-cm deep pressure measurement as for all other cases we acquired data at no less than 10-cm depth. Aggregating all cases, 1-min averaged wind speeds ranged up to 9 m s^{-1} with corresponding averaged pressure responses up to 11.5 Pa. With a 5 ms^{-1} wind forcing the average pressure response was 4 Pa, which was similar to the 5 Pa response Albert and others (2002) reported for 7 cm amplitude sastrugi. Since the magnitude of the pressure response to wind forcing depends on the shape and size of the topographic forcing we cannot directly compare our result with Albert's, other than to note an order of magnitude correspondence.

2.4.6 Stationary Pressure Attenuation

Although the magnitude and shape of the stationary pressure field depends on the nature of the topographic forcing, attenuation of the pressure field with depth

depends rather on the characteristics of the snow medium. For each case we determine stationary pressure attenuation by comparing the pressure magnitude near the surface with deeper measurements. The presence of attenuation was determined by subtracting stationary pressure magnitude at one depth from the measurement just above. We compiled this result for all cases in Fig. 2.10, which shows that, on average, the stationary pressure field decreases by 0.15 Pa m^{-1} below 10 cm. Monotonically decreasing stationary pressure was not typical because large excursions from a monotonic profile were common. These excursions obscured the decrease in stationary pressure with depth that is less ambiguously represented by ranking the pressure measurements. An ensemble average of all the cases indicates that the ordered rank for stationary pressure did attenuate with depth, consistent with Colbeck's and Albert's models. This result persists if we exclude any one of the cases from the ensemble result. The pressure sensors that we used had inadequate dynamic range to capture much larger near surface pressure changes. However, one can infer from case 2 (Table 2.1) for which we had measurements at 5-cm depth (Fig. 2.9) that topographically induced stationary pressure decreases most quickly near the air/snow interface and then attenuates more slowly with depth.

2.4.7 Perturbation Pressure Attenuation

We summarized the perturbation pressure energy given by the error bars in Fig. 2.7 for each case in Fig. 2.11, plotted against wind speed. Perturbation pressure increases superlinearly with wind speed. Rather than flattening out at high wind speed as seen for stationary pressure, the perturbation pressure curve maintains the same curvature at high values for all cases except case 6 (13 April in Fig. 2.11). For case 6 (Table 2.1) the perturbation pressure becomes less sensitive to wind speed as wind speed increases. Snow permeability at all depths was lowest for case 6, indicating that perturbation pressure is constrained in low permeability snow. We compared the arrival times of pressure perturbations at each depth by clipping out a 2-min (plus one data point) time period of 10-cm deep pressure data and a 1-min subset of pressure data from a deeper position and then sliding this subset index-by-index to find the position of best fit for the two signals as given by a Pearson correlation coefficient.

The best alignment between the time series occurred with zero time offset indicating there was no distinguishable time delay between the 10-cm deep and deeper measurements. This result is expected because pressure perturbations propagate at the speed of sound and our data acquisition rate (10 Hz) was not fast enough to resolve the propagation characteristics of high-speed pressure fluctuations.

2.4.8 Spectral Attenuation of Perturbation Pressure

As predicted by CB89 we find a spectral dependence of perturbation pressure attenuation within the snow wherein higher frequencies are more strongly attenuated with depth than are low frequencies. In Fig. 2.12 we plotted pressure spectra for picket 3 in case 3, which is representative for surface snow with moderately high permeability. A spectral diagram shows the fractional contribution to variance by each frequency and is plotted in log form because power rapidly decreases with increasing frequency. This plot displays pressure energy over frequencies ranging from a fundamental frequency of 0.01 Hz, which is defined by the averaging timespan, to the Nyquist frequency of 5 Hz, which is the highest resolvable frequency at a 10 Hz data acquisition rate. The data were initially subdivided into 30-min segments and 1024-point FFTs were then averaged. This averaged result represents a trade-off that improved signal-to-noise ratio at the expense of low-frequency resolution. The 1024 points acquired at 10 Hz corresponded to a 102.4 s averaging interval, which is slow enough for interstitial air movement to hydrostatically respond to pressure changes in a moderately permeable ~1 m deep snowpack. At the observed snow permeability and snow depth we capture the transition from a hydrostatic response to higher frequencies relevant to wind pumping.

As shown in Fig. 2.12, high-frequency pressure fluctuations are evident tens of centimeters deep in the snow. The spectra show that perturbation pressure energy decreases with depth in the snow down to 40-cm depth. Traces for the 40-cm, 50-cm and 75-cm depths overlay each other and suggest a noise floor, meaning that high-frequency energy had dissipated by this depth. In most cases we observed aliasing of higher frequency energy as well as evidence of a noise floor near the Nyquist frequency. For low permeability snow cases (not shown), differential spectral

attenuation is nearly absent, presumably because high frequencies had been attenuated in the 0-10 cm layer. For cases 1, 2, 4 and 6, the near-surface spectral slope (at 10 cm depth) was close to the -7/3 value predicted by similarity theory, as in Bachelor (1951). For cases 3 and 5 the magnitude of the spectral slope was less and closer to -5/3, consistent with values predicted by Van Atta and Wyngaard (1975). The decline in spectral slope at low frequencies is likely because the relaxation time scale of the pressure reference was similar to the time scale of the pressure fluctuations so the full magnitude of low-frequency pressure fluctuations was not captured. We did not find a systematic relationship that describes the dependency of spectral slope with other measured and derived parameters such as wind speed, turbulence intensity, atmospheric stability, surface snow density or permeability. We conclude that the perturbation pressure spectral slope also depends on snow characteristics for which we did not account, e.g. surface impedance, snow layering and tortuosity. That is, even with isotropic turbulence for which one might expect a -7/3 perturbation pressure spectral slope response, snow state may confound agreement between the measured and the expected spectral slope.

2.5 Discussion

CB89 developed a theoretical solution that describes the attenuation of perturbation pressure with depth for a thin snowpack. WD96 found an analogous solution for an infinitely deep snowpack. Both of these solutions use the same form of perturbation pressure diffusivity so we can compare our experimental results with these two theoretical results in that context. For both models the perturbation pressure diffusivity, κ_p is:

$$\kappa_p = \frac{K P_0}{\mu \phi} \qquad (2.1)$$

where K is intrinsic permeability, P_0 is atmospheric pressure, μ is air viscosity and ϕ is snow porosity. From WD96, diffusivity forms the basis for a diffusion scale length,

$$H(\omega_0) = \sqrt{\frac{2\,\kappa_p}{\omega_0}} \qquad (2.2)$$

where ω_0 is the forcing frequency. The diffusion length scale can be thought of as the depth to which air can diffuse for a given frequency of wind forcing. As the forcing frequency decreases, air has more time to diffuse and can diffuse through a thicker snow layer.

Using the diffusion length as a scaling parameter we compare the theoretical prediction for the ratio of perturbation pressure throughout the snow depth (denoted as p) with the near-surface value (denoted p_0) from CB89 and WD96 with our experimentally derived values. Both theoretical solutions assume constant permeability so for comparison we use a 10-20 cm value of 10^{-9} m^2, highlighted as a bold isopleth in Fig. 2.4. We assume a constant snow porosity ϕ=0.65, with other constants μ=1.65 × 10^{-4} Pl and P_0= 9.75 × 10^4 Pa, and h_0= 3 m consistent with experimental values.

We investigate the instantaneous perturbation pressure power at two representative frequencies, 0.04 Hz and 0.4 Hz, rather than the integral of the spectra (i.e. the variance) because the variability between cases at these frequencies is small thereby improving composite comparisons. These two frequencies bracket the 0.1 Hz frequency at which differential spectral attenuation typically increases (Fig. 2.12) and therefore represent solutions that bracket this kink point. We calculated attenuation with depth by dividing the instantaneous perturbation pressure at 10 cm from each deeper sensor. The experimental results show perturbation pressure attenuation with depth (box plots in Figs. 2.13 and 2.14). If the 10 cm sensor were located closer to the surface we anticipate the near-surface pressure measurement would be larger and the resultant p/p_0 ratio would then be smaller at each depth. Our measurements show larger attenuation with depth than predicted by either WD96 or by CB89 yet our measurements under-predict near-surface perturbation pressure attenuation. We obtain an estimate of the surface-relative attenuation by calculating the surface perturbation pressure that would yield the observed attenuation as given by the

comparison of perturbation pressure at 10 cm with deeper measurements. In both Figs. 2.13 and 2.14 the thin dashed curve represents an exponential curve fit to the data with p_0 given by the perturbation pressure at 10-cm depth. We solve this curve fit for the perturbation pressure at 1 mm depth to obtain an estimate of the surface perturbation pressure:

$$\frac{z}{H} = a \exp\left(b \frac{p_0}{p_{10}}\right) \qquad \rightarrow \qquad p_0 = \frac{p_{10}}{b} \ln\left(\frac{z}{Ha}\right). \tag{2.3}$$

We then recomputed the attenuation using this surface estimate to obtain the fit plotted as the solid curve in Figs. 2.13 and 2.14. At 0.04 Hz, an exponential curve fit of the form $a \times \exp(b \times p/p_0)$ gives coefficients a=-44.8 and b=-13.8. At 0.4 Hz, an exponential curve fit of the form $a \times \exp(b \times p/p_0)$ gives coefficients a=-0.11and b=-6.63.

The primary cause of variability in the ratio p/p_{10} between cases is not clear although we can discriminate several relevant parameters that are not the cause. For a given case, even large differences in density and intrinsic permeability with depth do not translate into large differences in perturbation pressure as seen by comparing Fig. 2.4 with Fig. 2.11. Likewise, wind turbulence spectra (not shown) do not indicate significantly different forcing that would lead to very different p/p_{10} ratios between cases. We suspect that differences in snow state other than density and intrinsic permeability such as surface hardness, tortuosity (microphysical structure) and layering account for much of the variability in p/p_{10} ratio between cases. For example, a thin, low permeability surface crust could inhibit turbulent energy and perturbation pressure transfer into the snowpack. In this instance, perturbation pressure entering the snowpack would be less than expected for a given bulk snow permeability and surface forcing.

An alternate analysis of pressure spectra presented by Clarke and Waddington (1991) supports this conclusion. The authors interpreted the difference in spectral magnitude between the surface and 10-cm deep pressure measurements as being due only to absorption by the snow medium. In the 10 cm pressure spectra, the spectral

slope of the deeper measurement is close to -7/3 whereas the spectral slope of the surface measurement is close to -1, suggesting that the near-surface pressure spectra capture dynamic pressure changes of airflow around the pressure sensor rather than an unfettered cascade of turbulently-generated perturbation pressure. An alternate interpretation of their results is that a significant portion of the energy difference between the surface and 10 cm depth measurements is due to scattering at the snow surface rather than solely due to attenuation through the snow layer.

In Fig. 2.14 we show theoretical and measured attenuation at 0.4 Hz, a frequency within the range of differential attenuation for all cases. Since the diffusion length scale is inversely proportional to forcing frequency, both theories predict greater attenuation at higher frequencies relative to lower frequencies but both theories still under-predict the observed attenuation. The experimental result is that high-frequency pressure perturbation is strongly attenuated with depth. Using a 3-D model Clarke and Waddington (1991) found that vertical perturbation pressure attenuation was enhanced by horizontal air flow when the surface forcing was spatially limited. Since the exposed portion of the snow pickets in our experiment generated a spatially-limited pressure field our experimental result qualitatively agrees with their theoretical result. From the pressure spectra in Fig. 2.12 it is clear that a small fraction of perturbation pressure energy resides at high frequencies, so strong attenuation of high-frequency pressure energy has a vanishingly small impact on spectrally-integrated attenuation with depth (i.e. the variance). Measured attenuation exceeds model predicted attenuation even if we assume an unreasonably low uniform snow permeability (e.g. 10^{-11} m^2, not shown) with a corresponding decrease in the *e*-folding depth.

2.6 Conclusions

We observed the relationship between wind and pressure at a data acquisition frequency of 10 Hz in an alpine snowpack to 1-m depth. The stationary pressure field that was formed by wind blowing over the exposed top 10 cm of a snow picket decreases with depth, consistent with Colbeck (1989) and Albert (2002). Since the stationary pressure field in our experiment was synthetic and because the shape of the

stationary pressure field depends on the shape of the topographic feature we broadly characterize this verification as order-of-magnitude agreement.

The thrust of this experiment was to separate stationary pressure from the perturbation pressure field so that we could assess the relationship between wind forcing and the vertical profile of perturbation pressure in snow. We have documented perturbation pressure attenuation with depth at high frequencies and derived empirical formulas to deterministically calculate the average perturbation pressure attenuation at two representative frequencies, 0.04 Hz and 0.4 Hz. At both these high frequencies the perturbation pressure field attenuated faster with depth than predicted by either Colbeck (1989) or Waddington and others (1996). The perturbation pressure attenuation difference between theory and measurement increased with frequency. This result agrees with the Clarke and Waddington (1991) result that found enhanced perturbation pressure attenuation when the surface forcing was spatially limited. In turn, this agreement underscores the importance of simulating windpumping as a 3-D process.

Since frequencies above 0.04 Hz contain a small fraction of the total spectral energy of the perturbation pressure field, attenuation at these high frequencies negligibly decreases the spectrally integrated pressure energy within 1 m of snow depth. Continuity in this trend towards lower frequencies suggests that attenuation decreases with decreasing frequency but remains greater than predicted by either of the two 1-D models considered in this paper. Although the fraction of perturbation pressure energy at high frequencies is small, differential spectral attenuation at high frequencies represents a signature that could be used to characterize the depth in snow that is perturbed by high-frequency turbulence. The lack of a robust similarity relationship between wind properties, perturbation pressure and permeability suggests that other parameters such as tortuosity, snow surface hardness and layering strongly affect perturbation pressure attenuation in snow. Explicit characterization of perturbation pressure energy for energy-rich lower frequencies remains a topic for future work.

2.7 Tables

Table 2.1. Case studies

Case	Date Range	Time Range CET	Time Span h
1	16 March	11:55-14:48	2.8
2	18 March	11:08-14:00	2.9
3	25 March	11:30-13:30	2
4	2 April	10:10-13:40	3.5
5	12 April	00:00-06:00	6
6	12-13 April	20:00-04:00	8

2.8 Figures

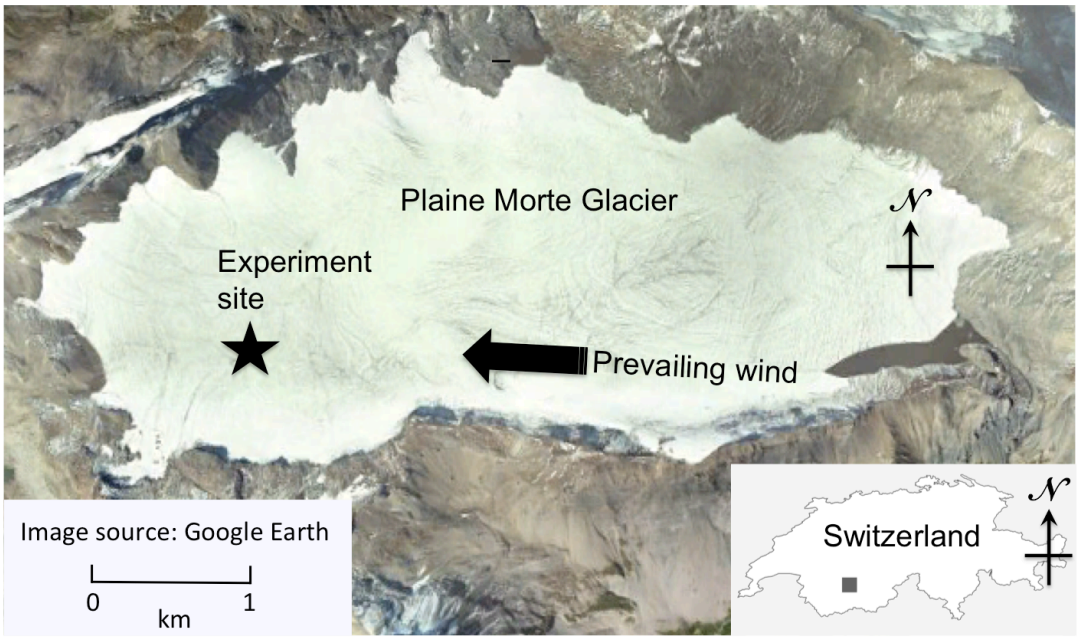

Figure 2.1. Plaine Morte Glacier, Switzerland (courtesy Google Earth) labeled with the experiment site (star). The bold arrow points in the direction of the prevailing wind.

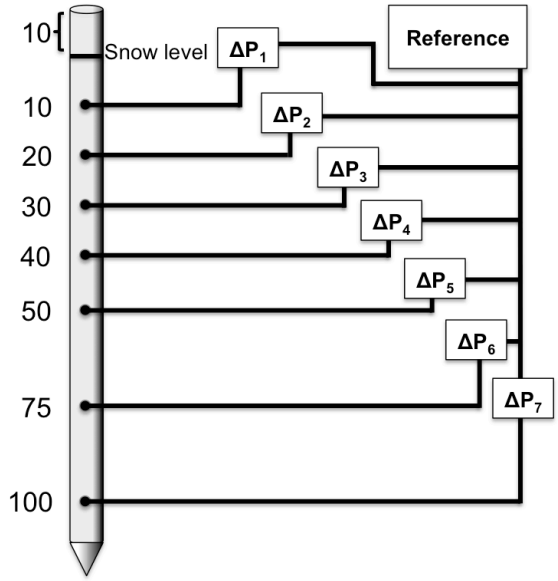

Figure 2.2. Schematic diagram of snow picket showing the most commonly used port locations (cm) and pressure reference.

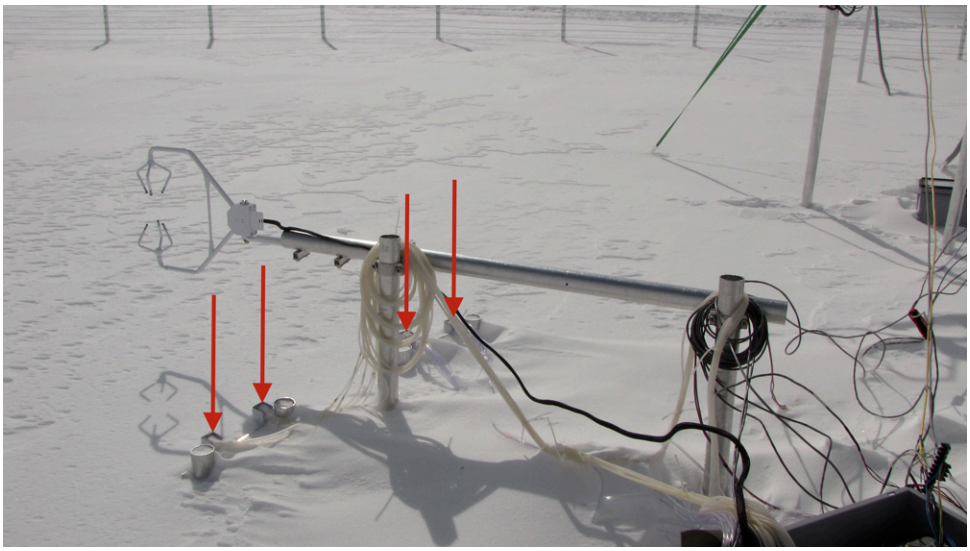

Figure 2.3. Campbell Scientific CSAT3 sonic anemometer poised above four snow pickets (only picket tops are visible below the red arrows) during the 25 March deployment (case 3).

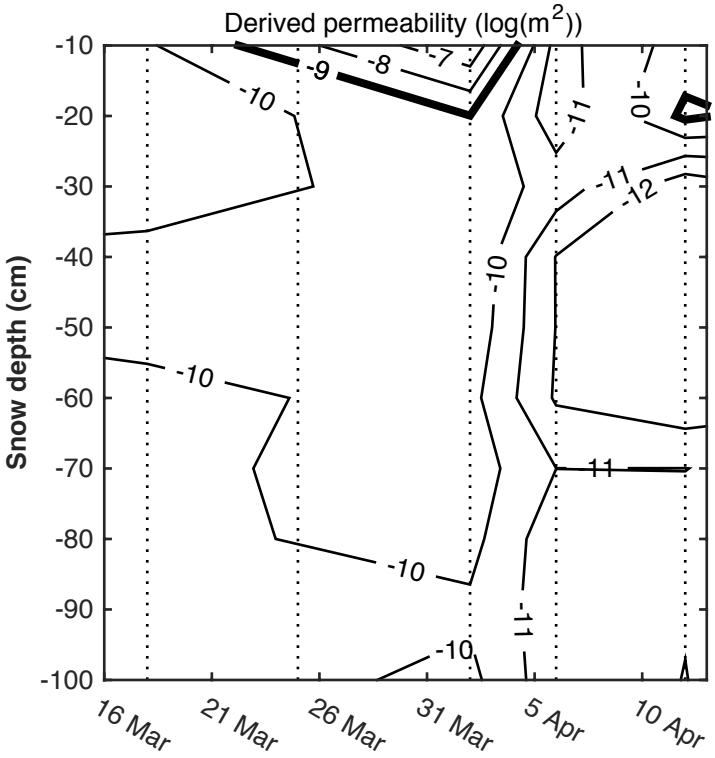

Figure 2.4. Derived snow permeability time-depth slice in $\log_{10}$ units. Vertical dotted lines indicate the dates that snowpits were measured. Snow permeability was derived from the Shimizu (1970) formula, based on measured grain size and snow density.

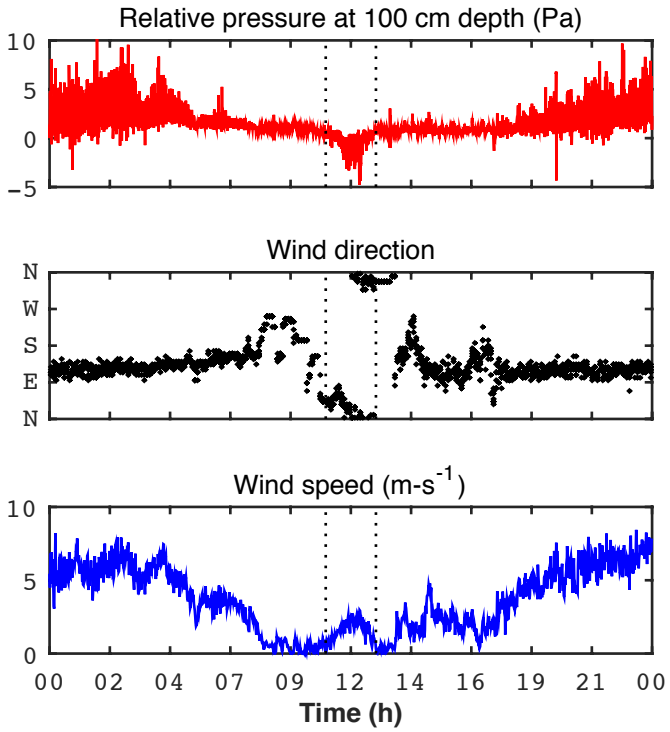

Figure 2.5. Relative pressure at 1-m depth, wind speed and wind direction are plotted for 12-13 April to show the directional dependence of relative pressure. Vertical dotted lines bracket the noon time frame during which wind direction changed considerably and the pressure response was evident at 1-m depth in dense snow.

Figure 2.6. Dug out pressure pickets (backside) on 11 April after a two-day deployment with warm daytime temperatures showing snow loss around the top of the picket but no direct air exposure below ~ 20 cm.

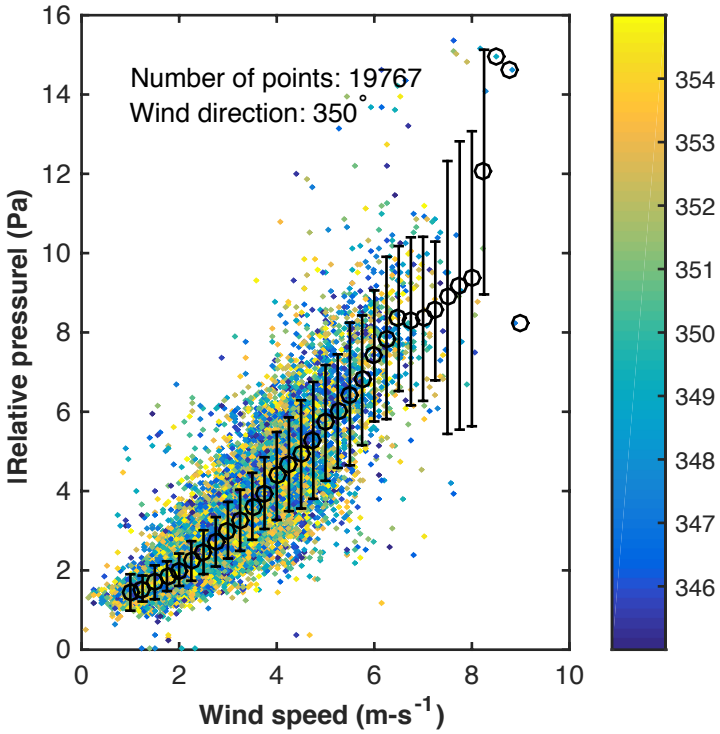

Figure 2.7. Pressure vs. wind speed bin-averaged at 20 cm depth in 0.25 m s^{-1} increments for data within ±5° of the prevailing wind direction. The colorbar indicates the wind direction in (°). Error bars signify one standard deviation below and above the mean bin-averaged wind speed, marked as circles.

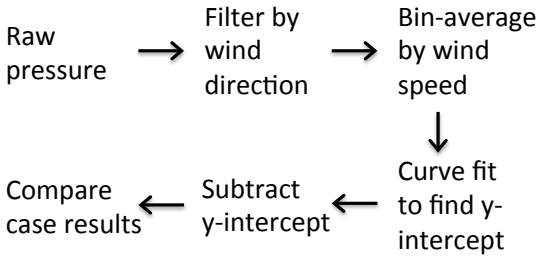

Figure 2.8. Flowchart showing steps taken to extract stationary pressure from pressure measurements.

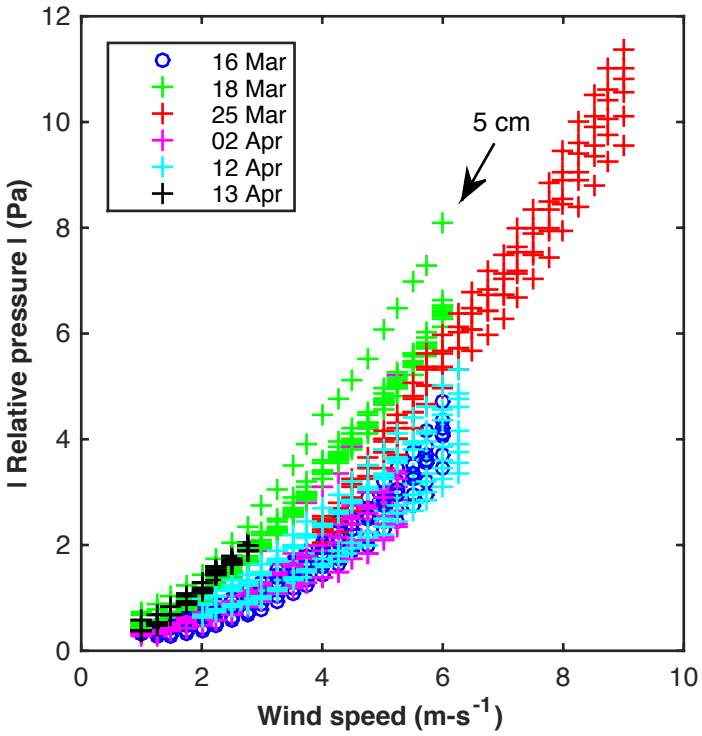

Figure 2.9. Stationary pressure vs. wind speed for pickets 3 and 4 at all depths and all cases. The difference in pressure response to wind forcing between all depths for a given case was small relative to the difference between cases because the snowpack differences between cases had a greater effect than snow depth for a given case. For a given case, the pressure response to wind forcing statistically decreased but rarely monotonically decreased. On 18 March the top measurement was at 5 cm rather than 10 cm and is indicated by an arrow.

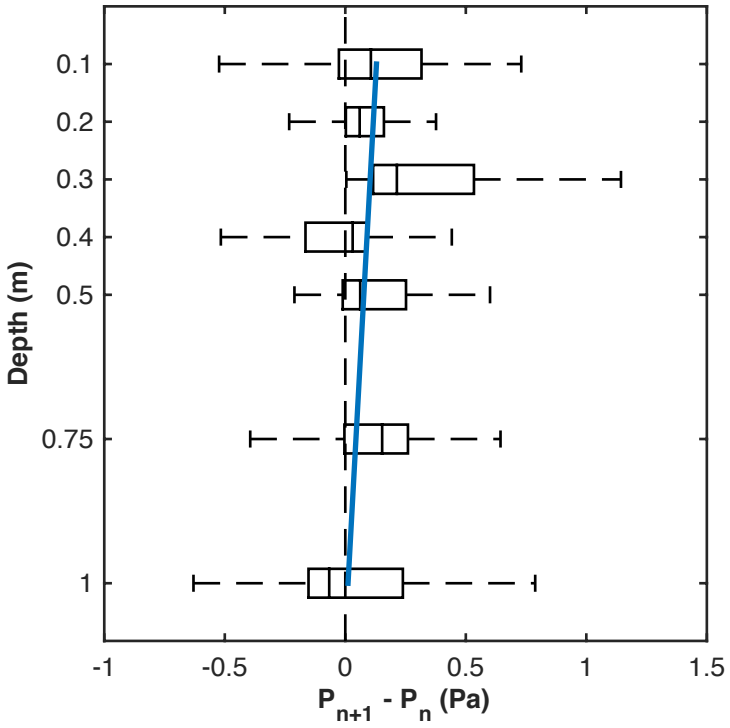

Figure 2.10. Stationary pressure attenuation with depth for pickets 3 and 4 using the data shown in Fig. 2.9.

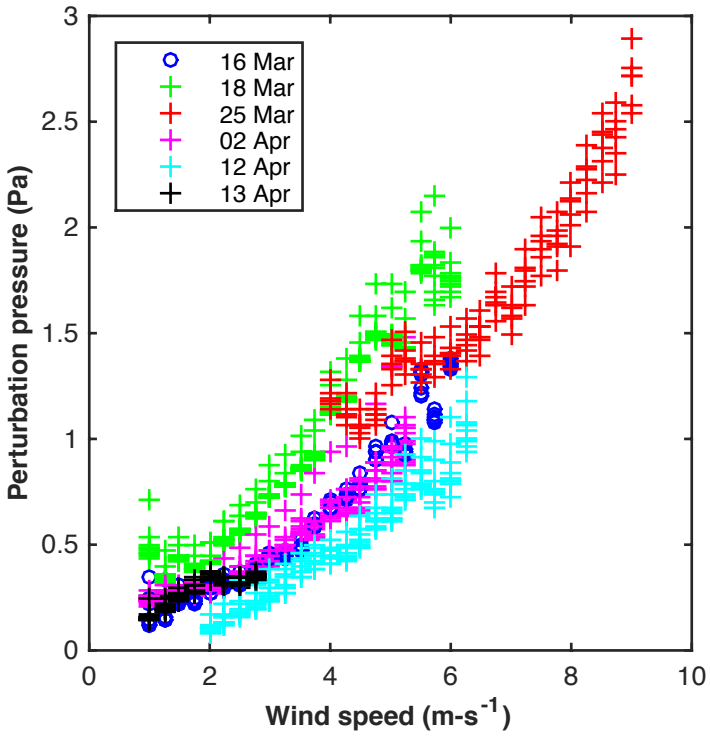

Figure 2.11. Perturbation pressure vs. wind speed for pickets 3 and 4 for all cases and all depths using the same pressure sensor data as shown in Figs. 2.9 and 2.10.

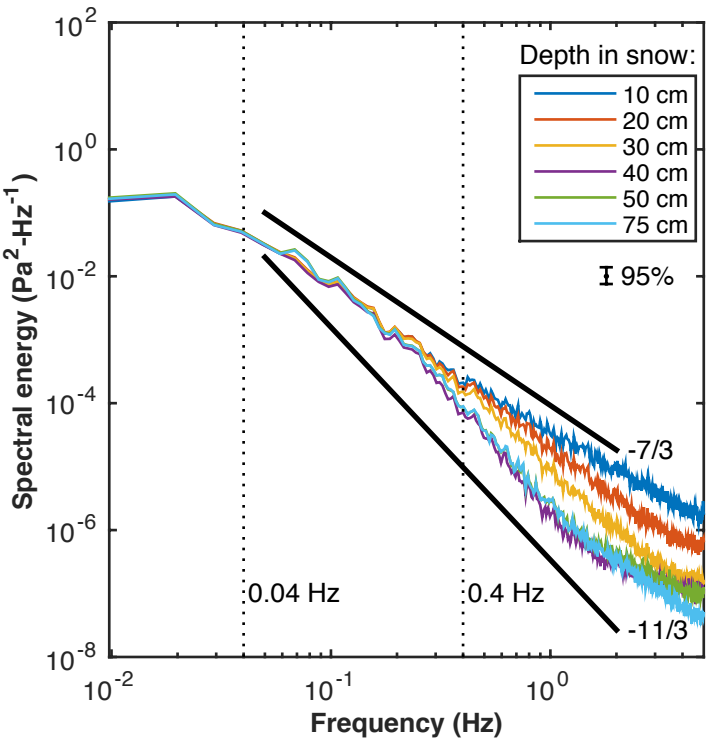

Figure 2.12. Picket #3 perturbation-pressure spectra for case 3 (25 March) at depths given in the legend. In this case, high-frequency perturbation attenuated monotonically with depth to the noise floor at ~ 40-cm depth. The 95% confidence interval is displayed below the legend.

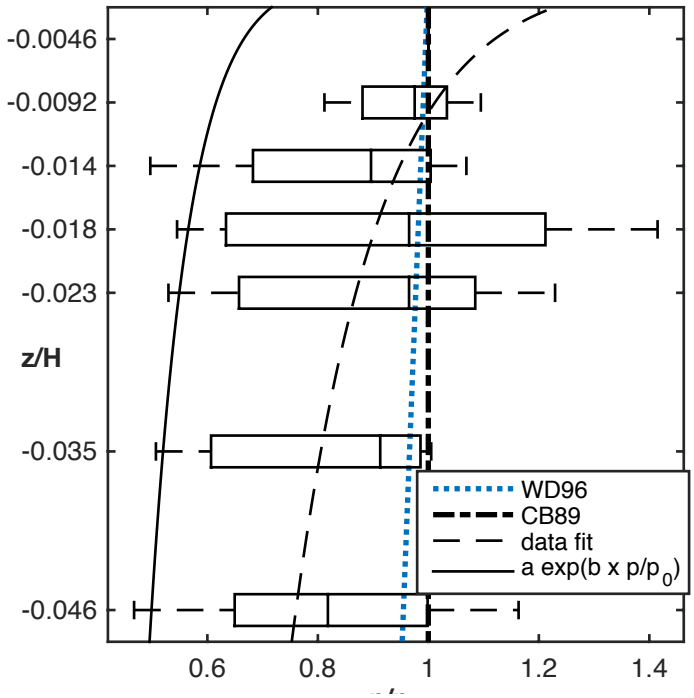

Figure 2.13. Measured and theoretical perturbation-pressure attenuation with depth at 0.04 Hz with depth scaled by the diffusion length scale. The horizontal axis is the perturbation pressure at a given depth divided by the reference (surface) perturbation pressure. The vertical axis is the depth divided by the diffusion length scale. The long-dashed curve shows measured perturbation pressure attenuation with depth using the 10-cm pressure as the reference pressure, p_0. The solid curve shows the attenuation calculated by extrapolating the tendency given by the long-dashed curve to the surface in order to determine a surface value for the reference pressure, p_0.

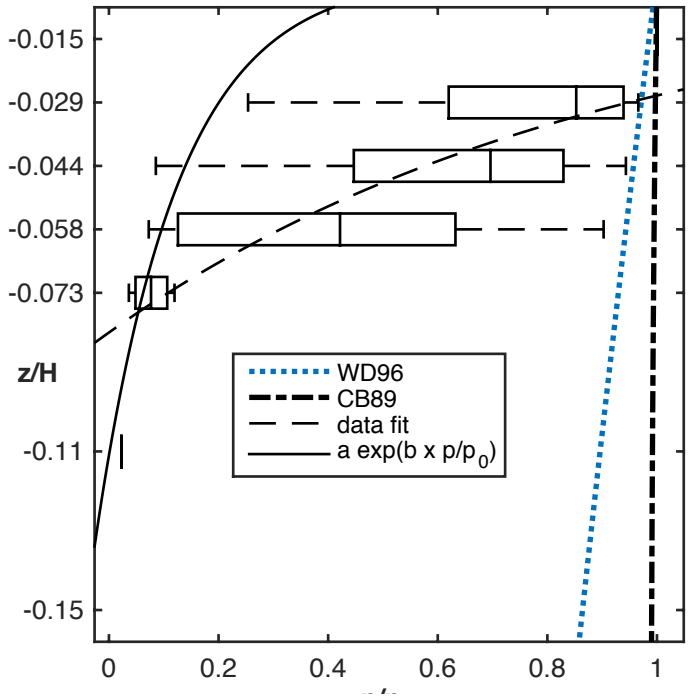

Figure 2.14. Measured and theoretical perturbation pressure attenuation with depth at 0.4 Hz with depth scaled by the diffusion length scale. The axes are the same as Fig. 2.13. The long-dashed and solid curves were computed by the same procedure as delineated in the Fig. 2.13 caption.

3 A low-cost acoustic permeameter

A low-cost acoustic permeameter

Stephen A. Drake[1], John S. Selker[2], Chad W. Higgins[2]

[1]CEOAS, Oregon State University, Corvallis, 97333, USA
[2]BEE, Oregon State University, Corvallis, 97333, USA

Submitted to:

Geoscientific Instrumentation, Methods and Data Systems

3.1 Abstract

Intrinsic permeability is an important parameter that regulates air exchange through porous media such as snow. Standard methods of measuring permeability are inconvenient to perform outdoors, fraught with sampling errors and require specialized equipment, while bringing intact samples back to the laboratory is also challenging. To address these issues, we designed, built, and tested a low-cost acoustic permeameter that allows computation of volume-averaged intrinsic permeability for a homogenous medium. Permeameter elements were designed for use in snow but the measurement methods are not snow-specific. The electronic components, consisting of a signal generator, amplifier, speaker, microphone and oscilloscope, are inexpensive and easily obtainable. The permeameter can be operated with a microphone either internally mounted or buried a known depth in the medium. The calibration method depends on choice of microphone positioning. For an externally located microphone, calibration was based on a low-frequency approximation applied at 500 Hz that provided an estimate of both intrinsic permeability and tortuosity. For an internally mounted microphone, calibration was based on attenuation at 50 Hz and returned only intrinsic permeability. We used reticulated foam of known permeability (ranging from 2×10^{-7} m^2 to 3×10^{-9} m^2) and estimated tortuosity to validate both methods. For the externally mounted microphone the mean normalized standard deviation of estimated parameters was 6% for permeability and 2% for tortuosity. The mean relative error from known measurements was 17% for permeability and 2% for tortuosity. For the internally mounted microphone the mean normalized standard deviation for permeability was 1.3%. Relative error is not given for this second method because the spline calibration yielded exact matches at the calibrated (known) data points but errors could amplify if environmental factors modify signal attenuation. Permeability determination for an externally mounted microphone is less sensitive to environmental noise than is the internally mounted microphone and is therefore the recommended method. The approximation using the internally mounted microphone was developed as an alternative for circumstances in which placing the microphone in the medium was not

feasible. Environmental noise degrades precision of both methods and is recognizable as increased scatter for replicate data points.

3.2 Introduction

Intrinsic permeability is the proportionality constant in Darcy's Law that describes the interconnectedness of air space in permeable media such as snow. It has long been recognized as an important parameter that regulates air exchange both within the snow pore space and between the atmosphere and the snowpack (Bader, 1939). Since permeability is difficult to measure directly, early efforts focused on developing empirical relationships that describe permeability as a function of more easily measured parameters such as snow density (Bender, 1957; Shimizu, 1970; Martinelli, 1971). These convenient formulations may be accurate for the specific snow conditions used to establish the empirical formula but often fail for other snow conditions (Domine et al., 2013). In an effort to obtain more accurate field measurements of permeability several experimental efforts employed vacuum flow-through devices (Conway & Abrahamson, 1984; Chacho & Johnson, 1987; Hardy & Albert, 1993; Albert et al., 2000; and Courville et al., 2007). However, flow-through measurements are time consuming and fraught with potential sampling errors and alteration of the sample from its native condition (Sommerfeld & Rocchio, 1993). Some sampling issues have been resolved by sample extraction and examination in a lab environment to measure pore space in terms of specific surface area by X-ray tomography and gas adsorption techniques (Kerbrat et al., 2008). But this multi-step process requires specialized equipment and still does not resolve issues of small-scale spatial heterogeneity and sample size representativeness (Albert, 2001).

In this paper, we describe the design, construction, and calibration of an *in-situ* active acoustic device that samples a measurement volume larger than that obtainable with current flow-through devices to acquire a volume-averaged estimate of intrinsic permeability. Active sampling methods of snow properties have been successfully applied in previous studies. For example, Albert et al. (2007) measured the evolution of an acoustic pulse, generated by firing a pistol blank, and compared the pulse shape with that of a simulated pulse to estimate volume-averaged

permeability of an Alaskan snowpack. Kinar and Pomeroy designed (2007) and improved (2015) upon an active acoustic device that infers properties such as snow water equivalent from the differential backscatter at frequencies between 20 Hz and 10 kHz. The two methods that we present are less sophisticated than either the Albert or Kinar methods but have the advantage that no specialized equipment is required. Our design borrows elements from Ishida (1965), Buser (1986), and Moore et al. (1991).

3.3 Method

3.3.1 Design and Assembly of the Acoustic Permeameter

We assembled an acoustic permeameter from commonly available parts (Fig. 3.1). A Heathkit Model IG-1275 signal generator produced a sine wave of a specified frequency and amplitude that was split and directed both to channel 1 of a Tektronix TDS 1001 oscilloscope and to a 4Ω Altec A4468 speaker. Electrical components were powered from a DC-AC inverter and 12V car battery. The speaker was screw-mounted onto a ring of 3/4-in-thick medium-grade plywood. An acoustic tube was constructed using 8-in diameter, schedule 40 PVC pipe. The acoustic tube was vertically mounted onto the plywood ring and secured with butterfly clamps. During measurement, the tube was placed on the medium of interest with the speaker facing downward such that sine waves emanating from the speaker would interrogate the medium. The subsequent acoustic response was captured by a Radio Shack™ unidirectional microphone (model 3303038, frequency range: 50 Hz-15 kHz) and directed to the second input channel on the oscilloscope. Frequency and amplitude of input and output signals were stored on the oscilloscope USB drive.

3.3.2 Acoustic Permeability Determination – External Microphone Method

The first method used to measure intrinsic permeability involved using an externally placed microphone (EM), where we placed the test media between the sound source and the microphone. The calibration setup for the EM method is similar to Fig. 3.1 but with the speaker mounted in an upward orientation and the microphone mounted directly above the centerline of the PVC tube, facing downward. Acoustic

intensity at a given frequency was measured with the microphone in open air to establish reference amplitude. Then a foam sample was placed over the end of the speaker tube and weighted at the edges to minimize sample vibration. At each applied frequency, attenuation and phase shift were determined by comparison with the reference measurement. We then utilized the low-frequency approximation in Moore et al. (1991, hereafter referred to as M91), to calculate permeability. In M91, estimates of tortuosity (τ) and effective flow resistivity (σ_{pe}) were iteratively adjusted until optimal agreement between the measured and modeled value for the propagation constant (k_b) at a given frequency (f) was obtained. Snow permeability (k) can then be computed from flow resistivity given knowledge or assumptions of the snow grain shape. The theoretical basis for the M91 low-frequency approximation is described in section 3.4 of this paper. An added benefit of this method relative to a flow-through permeameter is that it produces a measure of tortuosity as well as permeability.

3.3.3 Acoustic Permeability Determination – Internal Microphone Method

A second permeability measurement method employed the microphone mounted inside the acoustic tube, facing outward, at a fixed position (15 cm) from the open end. We refer to this as the IM method. We measured attenuation at 50 Hz relative to an open-air value with the open end of the acoustic tube snug against the test media. At this frequency, the wavelength of the emitted frequency is much greater than the length of the acoustic tube. Since the medium represents an acoustic barrier to the emitted waveform, the amplitude of the transmitted waveform was progressively retarded as permeability increased. Simultaneously, the amplitude of the reflected waveform, measured by the internally mounted microphone, increased. From Morse (1952, hereafter referred to as M52) the attenuation at a given frequency is a function of flow resistivity. Amplitude of the reflected waveform is inversely proportional to the amplitude of the transmitted waveform so permeability was computed as a function of the ratio between the initial amplitude and the reflected amplitude.

3.3.4 Flow-through Permeability Determination

We verified acoustic permeameter measurements with 5-cm-thick reticulated foam samples. The permeability of these foam samples was established with a flow-through permeameter similar to Albert et al. (2000) with the exception that we utilized three high-precision (Paroscientific 216B) absolute pressure sensors rather than two relative pressure sensors (Fig. 3.2). Using absolute pressure sensors rather than relative pressure sensors required a modification of Albert's method so we briefly describe our alternate method. For each foam type we cut a cylindrical section and spread a layer of petroleum gel around the cut edge. We then slid the cut foam into the double-walled permeameter until the inner face of the foam was flush against the inner wall of the permeameter as shown in Fig. 3.2. The gel sealed gaps between the foam and vessel wall. We cross-calibrated the three pressure sensors before initiating airflow through the permeameter. The three pressure sensors monitored atmospheric, inner cylinder, and outer cylinder pressures. Following Albert et al. (2000), we acquired the pressure drop across each foam sample at 8-12 flow rates while adjusting a valve to regulate the pressure between the inner and outer vessel to eliminate radial flow. We used the slope of the subsequent flow rate vs. pressure drop curve to derive permeability from Darcy's law valid for Reynolds numbers less than 1:

$$k = \frac{Q\ L\ \mu}{\Delta P\ A} \qquad (3.1)$$

where k is intrinsic permeability (m^2), Q is volumetric discharge (m^3-s^{-1}), A is the sample surface area (m^2), L is the sample height (m), ΔP is the pressure drop (Pa) and μ is dynamic air viscosity (kg-m^{-1}-s^{-1}). Our samples were distinct in properties from those published by Clifton et al. (2008) (Table 3.1), suggesting that intrinsic permeability of reticulated foam with the same specified pores per linear inch (PPI) but different manufacturers (here Regicell and FXI Corporation) must be determined experimentally. Permeability measured for the FXI samples in Table 3.1 span

expected snow permeability values ranging from lightly compacted snow (low permeability) to depth hoar (high permeability) (Arakawa et al., 2009).

3.4 Theory

In this section, we describe the theoretical basis for the two methods used to acoustically measure snow permeability.

3.4.1 Theory for the EM Method

The complex propagation constant for sound through permeable media can be written in general terms as:

$$k_b = a + ib \tag{3.2}$$

Coefficients of the propagation constant define the phase and magnitude of attenuation, respectively, and are defined in M91 as:

$$a = \frac{\pi\,\Delta\phi}{180\,d} \tag{3.3}$$

$$b = \frac{Attenuation(dB)\ln(10)}{20d} \tag{3.4}$$

where $\Delta\phi$ is the phase shift (in degrees) between a free air measurement and the in-snow measurement and d is the media thickness. We measure attenuation in terms of a voltage difference between the input (V_{IN}) and output signal (V_{OUT}) as:

$$Attenuation(dB) = 20\,log_{10}\left(\frac{V_{OUT}}{V_{IN}}\right) \tag{3.5}$$

Attenborough (1983) developed a four-parameter acoustic model that describes acoustic attenuation through permeable media. These four parameters: porosity,

effective flow resistivity, pore shape factor and grain shape factor collapse to two parameters in the low-frequency approximation given in M91:

$$k_b = 0.0079\sqrt{f}\left[9.10\tau f + i4\sigma_{pe}\right]^{0.5} \quad (3.6)$$

The M91 authors used Eq. (3.6) to calculate the propagation constant for a given tortuosity and flow resistivity and Eqs. (3.2-3.5) to calculate the propagation constant from phase shift and attenuation. Values for flow resistivity and tortuosity in Eq. (3.6) were iteratively adjusted until the difference between the propagation constant determined by these two methods was minimized. Due to environment-dependent nonlinear responses at both low and high frequencies the M91 authors obtained the best fit when they used well chosen point measurements rather than measurements over a range of frequencies. Similarly, our results are based on well-chosen point measurements. But instead of iteratively solving Eq. (3.6) we separate the real and imaginary parts to independently solve for tortuosity and effective flow resistivity:

$$\tau = \frac{[a^2 - b^2]}{[9.10][0.0079]^2 f^2} \quad (3.7)$$

$$\sigma_{pe} = \frac{ab}{2[0.0079]^2 f} \quad (3.8)$$

We then apply empirical calibrations to match derived tortuosity and effective resistivity with known values.

3.4.2 Theory for the IM Method

With the alternate configuration of the microphone placed inside the acoustic tube, Eqs. (3.2-3.8) are no longer applicable. Instead, we use an alternate theoretical basis to determine intrinsic permeability based on results described in M52. M52 found and Ishida (1965) verified a simple relationship between flow resistivity and signal attenuation:

$$\alpha = \beta\sqrt{\omega\sigma} \;\rightarrow\; \sigma = \frac{\alpha^2}{2\pi f} \times 10^n \qquad (3.9)$$

where α is an attenuation constant, β is an empirical constant, ω is the imposed angular frequency and σ is flow resistivity. As with the EM method, we fit a sine wave to the input and output signals to eliminate white noise and then determined the phase offset and attenuation between the input and output signals as a function of the input frequency. Instead of measuring the attenuation through the media, we measure the amplitude of the reflected waveform at 50 Hz. We take the amplitude of the reflected acoustic energy as an empirically-derived function of the transmitted acoustic energy. Using reticulated foam samples of known permeability, we relate the ratio of the reflected signal amplitude to initial signal amplitude with flow-through permeability measurements.

3.5 Results

3.5.1 Results for the EM Method

Having calibrated permeability of the reticulated foam samples with the flow-through permeameter we subsequently obtained acoustic measurements by the EM method. Three replicates were acquired for each foam sample at each frequency. After some experimentation, we opted to utilize data acquired at 500 Hz because this frequency lies within the valid range of frequencies for the low-frequency approximation (500 Hz to 2000 Hz) and because the 500 Hz results were more replicable than those acquired at higher frequencies.

In M91 flow resistivity and tortuosity were determined by iteratively finding the best fit between measurements given in Eqs. (3.2-3.5) and the theoretical prediction given in Eq. (3.6). Since we know *a priori* the foam tortuosity and permeability we compared the known effective flow resistivity with the effective flow resistivity computed from Eqs. (3.2-3.8). As in Albert (2007) and using a pore shape factor ratio (s_f) of 1, the effective flow resistivity as derived from permeability is:

$$\sigma_{pe} s_f^2 = \frac{\mu}{k} \qquad (3.10)$$

where μ is dynamic viscosity of the air. For the foam samples, we found that a linear fit resolved the difference between computed and known flow resistivity for a given permeability. In short, acoustically derived effective flow resistivity did not match the actual effective flow resistivity but deviated by a linear function from it. Therefore, from Eq. (3.10), computed flow resistivity is a linear function of permeability.

In Fig. 3.3 we plotted the results of three independent data sets, each data set corresponding to a different volume setting on the signal generator and rendered in a different color. For a given data set, the signal generator volume was established for the first data point and not changed for the remaining data points. Data corresponding to the blue/black/red data sets had initial imposed volume that associated to RMS signal input voltages of 1.3/2.3/5.6V, respectively. Plotted in log/log format, data points for each data set in Fig. 3.3 are roughly collinear and the slope of the best-fit line for a given data set is nearly parallel to the other two data sets but the data sets are not coincident (Fig. 3.4). This result indicates that as the amplitude of the imposed sine wave was increased, absolute attenuation of the signal also increased. Since the acoustically derived permeability is sensitive to the amplitude of the imposed waveform, it is therefore important to use the same amplitude waveform in the calibration as in subsequent permeability measurements. The relationship between σ_{pe} and k reversed at the highest permeability in Fig. 3.3. The reason for this reversal is possibly attributable to non-linearity in microphone response and represents an upper limit to the permeability that can be measured by this technique within the constraints of our experimental design. Triplicate data points were nearly coincident in most cases; however, the blue and black asterisks in Fig. 3.3 correspond to points that were more than a standard deviation removed from the other two points in the given triplicate measurement. Differences in the imposed amplitude for these two data points does not account for their deviation from the mean suggesting the source of error was environmental. These data were acquired outside in a relatively quiet but acoustically uncontrolled location so we attribute this error is to intermittent external

noise. It is therefore also important to acquire multiple data points for each measurement so that one can distinguish the impact of incidental, external noise.

Uncalibrated tortuosity calculated for different foam samples was nearly very similar but unrealistically high with an average of 17.7 and standard deviation of 1.54 between all of the samples. A slight but monotonic decrease in measured tortuosity with decreasing permeability accounted for most of the standard deviation as opposed to random scatter. For comparison, analogous data from Alvarez-Arenas et al. (2006), Kino et al. (2012) and references in Melon and Castagnede (1995) and Doutres and Atalla (2012) note that reticulated foam commonly has a narrow range of tortuosity from 1.03 to 1.06. Tortuosity of the FXI reticulated foam is not independently measured but shares other specifications with these other sources and likely has tortuosity in the same range.

We empirically compensate for the differences between the theoretical and experimentally derived values for tortuosity and effective flow resistivity. Our rationale is that the functional relationships between the theoretically and derived values for tortuosity and effective flow resistivity are the same so the differences in values can be resolved by a first-order calibration. Calculated tortuosity depended very weakly on media permeability so multiplying the calculated tortuosity by an empirically derived constant renders the theoretical value. On the other hand, calculated permeability varies linearly (on a log scale) with effective flow resistivity (as shown in Fig. 3.4) so a linear calibration is required to calculate permeability from measured effective flow resistivity. The multiplicative constant for tortuosity is found by dividing the mean known tortuosity by the mean derived tortuosity. The linear calibration relating effective flow resistivity to permeability is taken from the slope of the line in Fig. 3.4. In practice, one must calibrate the acoustic permeameter with media of known permeability and tortuosity to derive these multiplicative constants. Once these multiplicative constants have been determined for the acoustic permeameter, the tortuosity and permeability of other media can be derived without *a priori* knowledge of media tortuosity or permeability. For the 5.6V data set we find the multiplicative constant as: $\alpha = 0.057$. For the same data set a linear fit between measured flow resistivity and known permeability is given by:

$$log_{10}(k) = -2.0219 \times log_{10}(\sigma_{pe}) - 0.1764 \quad (3.11)$$

With these modifications, the M91 method obtains derived tortuosity ranging from 1.02 to 1.07 for the foam samples with a standard deviation of ±0.03. Percentage normalized standard deviation for permeability measurements ranged from 2.1% for the Z80 foam to 11.6% for the Z30 foam with a mean of 6.2% across all foam samples. We normalize the standard deviation because this error measure does not change when effective flow resistivity is calibrated with a multiplicative constant.

3.5.2 Results for the IM method

Applying Eq. (3.9) to results obtained with the microphone placed inside the acoustic tube at 50 Hz, 100 Hz, and 250 Hz yielded results shown in Fig. 3.5. Since we are measuring reflected acoustic energy rather than transmitted energy the result shown in Fig. 3.5 is an indirect (relative) measure of flow resistivity. Triplicates were acquired for each foam sample and these data were highly reproducible as shown by the close grouping of each triplicate. Data at these three frequencies were acquired on different days, each with a slightly different amplitude baseline (free air) setting, accounting for the horizontal displacement between curve fits. The percentage normalized standard deviation for 50 Hz measurements ranged from 0.08% for the Z50 sample to 5.8% for the highest permeability (Z10) sample. Since data at 50 Hz show improved precision relative to 100 Hz and 250 Hz data, as given by the wider domain of reflected signal amplitude, we use data at 50 Hz to compute permeability. The piecewise spline fit (black, in Fig. 3.5) describes the calibration between acoustically derived resistivity and the red dashed line delineates a smooth curve used to calibrate measurements to flow-through permeability. There is a measurable phase shift with decreasing permeability of the test media, however, M52 does not offer a relationship for tortuosity so none was attempted with this method. Microphone response limitations precluded measurements below 50 Hz.

3.6 Discussion

Derived permeability using the EM and IM methods are compared with the flow-through (known) permeability in Fig. 3.6. Intrinsic permeability for each foam sample is given in Table 3.1. Ideally, all measurements would fall on the diagonal line in Fig. 3.6 meaning that acoustically measured permeability equals known permeability for each foam sample. We find satisfactory agreement with known permeability for both acoustic methods. The average percentage error for the EM method was 17%. Since the IM method uses a spline fit the percentage error is zero. However, the curve fit is nonlinear so a small error in effective flow resistivity for a high permeability medium has a greater impact than the same error for a low permeability medium.

The EM and IM methods for determining permeability each have advantages and disadvantages. One advantage of the EM method is that the function relating effective flow resistivity to permeability is linear, unlike the more complicated relationship for the IM method. An advantage of a linear function is that a small error in measuring the x-coordinate yields an error that is invariant with relative magnitude when determining the y-coordinate, regardless of the magnitude of the measurement. This behavior is not true for non-linear functions such as the more complicated function employed in the IM method. A disadvantage of the EM method is that it is not valid for high permeability media over the range of parameters that we tested (e.g. 5 cm media thickness). The IM method suffers decreasing precision at high permeability because the slope of the curve is increasing but, unlike the EM method, the curve fit remains valid. Data acquired using the IM method was highly reproducible for all of our samples, which to some extent compensates for the slope-induced decrease in precision at high permeability. Another potential disadvantage of the EM method is that the microphone must be placed in the media to be measured. Depending on the circumstance, emplacement in the media may be difficult or impractical. Finally, a disadvantage of the IM method is that it is more empirical than the EM method, which may limit its applicability to different media types. Due to the linear functional form of the EM method, we suggest that it is the preferred method as

long as the media to be measured has a permeability that is within the valid range of measurements given by the calibration.

3.7 Conclusions

We conclude that it is feasible to derive intrinsic permeability with a low-cost acoustic permeameter by either the EM method or the IM method. This system returns an unambiguous, volume-averaged permeability consistent with snow densities ranging from lightly compacted snow to depth hoar. The EM method returned intrinsic permeability within 17% of flow-through measurements and within 2% of comparable tortuosity measurements. Measurement reproducibility by the IM method is very high such that the standard deviation between measurements is dwarfed by environmental factors such as background noise or inhomogeneities in the media of interest. These methods are relevant in studies for which an expedient volume average trumps a more detailed but time-consuming vertical profile that requires measuring multiple samples using a flow-through permeameter. One significant advantage of using these methods is that a particular frequency is measured rather than a broad spectrum. This feature obviates the need for specialized equipment used by other methods, such as a random noise generator and a spectral recorder/analyzer. Disadvantages of this system are that measurements are affected by environmental conditions such as background noise and wind.

3.8 Tables

Table 3.1. Regicell foam permeability from Clifton et al. (2008) and FXI foam permeability measured with a flow-through permeameter described in this paper.

Foam Type	Flow-through Permeability (m^2)
Regicell 10	160×10^{-9}
Regicell 30	39×10^{-9}
Regicell 60	6×10^{-9}
FXI Z10	206×10^{-9}
FXI Z20	137×10^{-9}
FXI Z30	47×10^{-9}
FXI Z50	15×10^{-9}
FXI Z80	3×10^{-9}

3.9 Figures

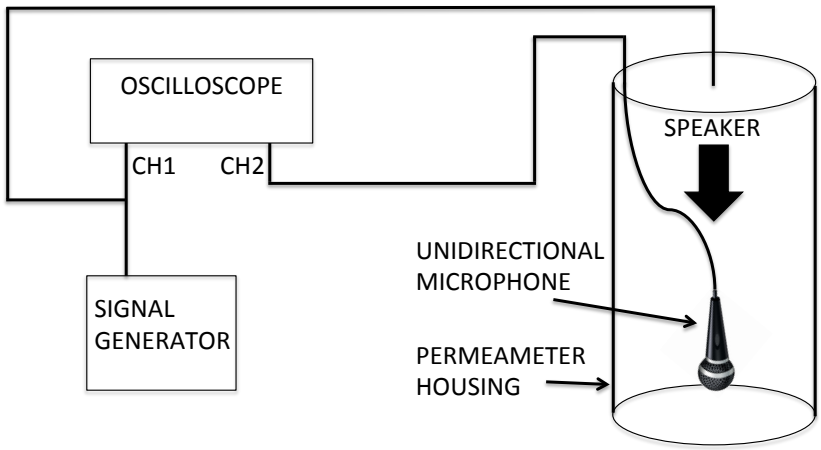

Figure 3.1. Acoustic permeameter schematic diagram.

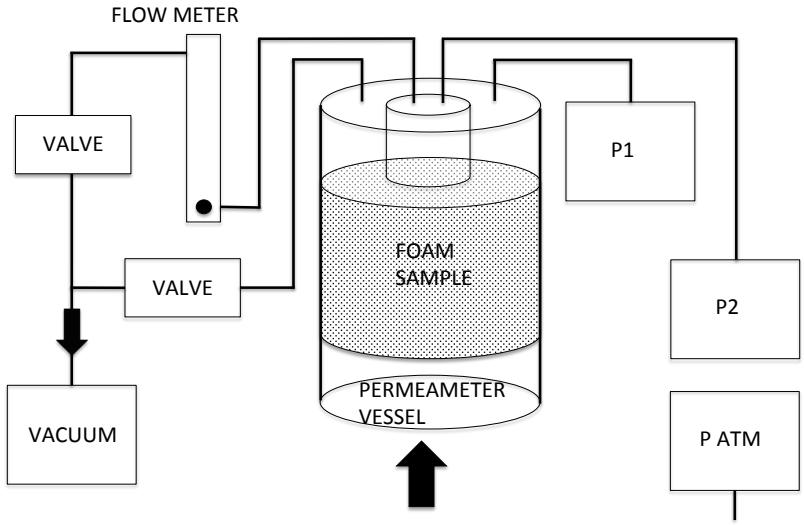

Figure 3.2. Flow-through permeameter with three absolute pressure sensors labeled P1, P2, and P ATM.

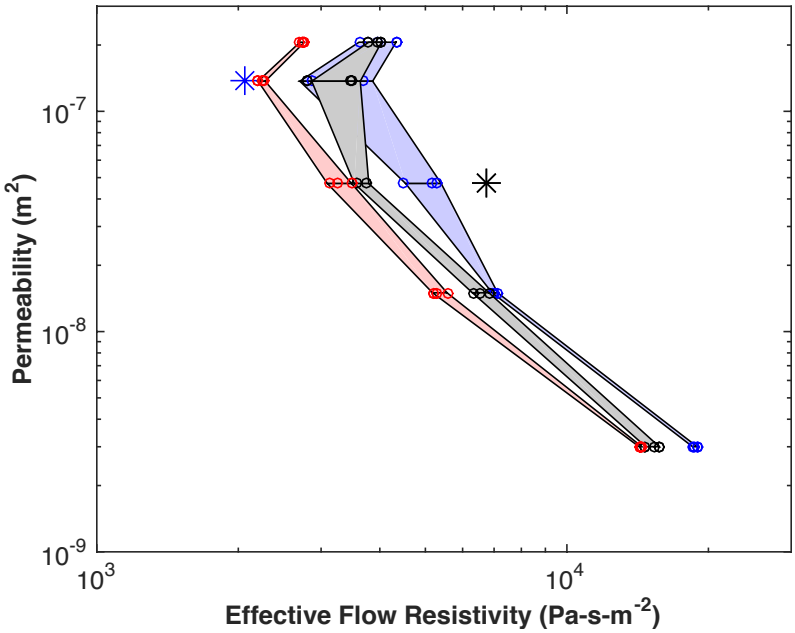

Figure 3.3. Comparison of acoustically derived permeability using M91 method at 500 Hz at three different initial conditions highlighted in blue, black and red corresponding to RMS signal voltages of 1.3/2.3/5.6 volts, respectively. Color-filled regions indicate data within one standard deviation of the mean. The asterisks indicate data points that exceeded one standard deviation from the mean (before they were excluded) and were thus excluded from subsequent analysis.

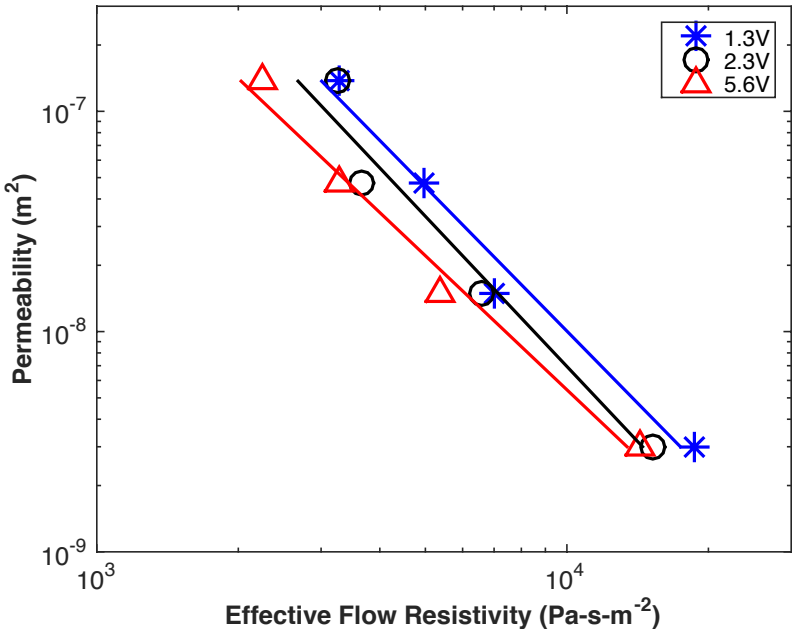

Figure 3.4. Linear regressions for data in Fig. 3.3 with the same color for each data set. R^2 values were 0.98 (blue), 0.98 (black) and 0.99 (red).

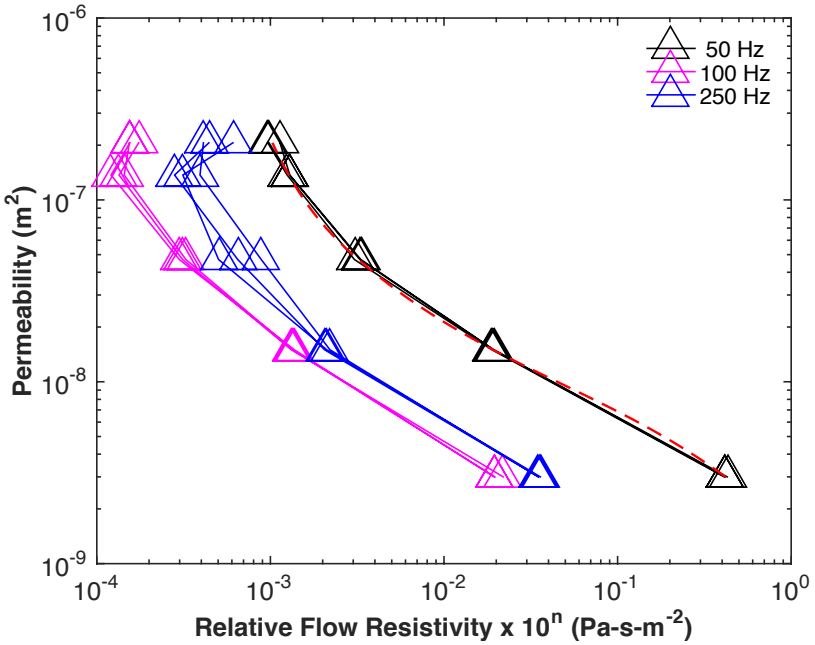

Figure 3.5. Flow-through permeability as a function of relative flow resistivity using the M52 method and Eq. (3.9) at 50 Hz, 100 Hz and 250 Hz. Three data points were acquired at each frequency and each foam type.

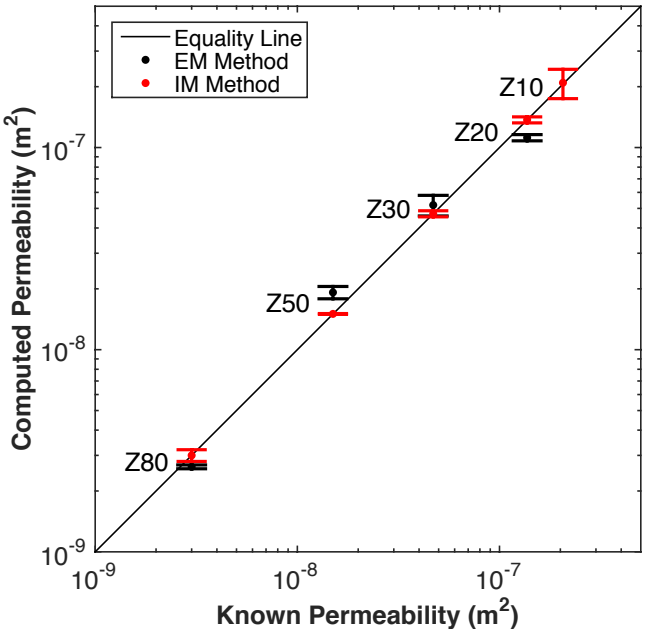

Figure 3.6. Comparing flow-through (known) permeability with the EM method at 500 Hz and the IM method at 50 Hz for foam samples given in Table 1. Z10 permeability was not computed by the EM method because k/σ_{pe} is nonlinear at high permeability, as shown in Fig. 3.3.

4 Wind ventilation of homogenous seasonal snow layers

Wind ventilation of homogenous seasonal snow layers

Stephen A. Drake[1], Eric Skyllingstad[1] and Chad Higgins[2]

[1]College of Earth, Ocean, and Atmospheric Sciences, Oregon State University
[2]Biological and Ecological Engineering, Oregon State University

To be submitted to:

The Cryosphere

4.1 Abstract

Atmospheric pressure changes do not stop at the permeable snow surface but rather propagate into it. These pressure changes range from high-amplitude, low-frequency events caused by synoptic weather systems to small amplitude, high-frequency events caused by turbulence. Processes that drive interstitial and near-surface air movement depend on the amplitude and frequency of atmospheric pressure changes. These processes are locally weak but geographically pervasive and temporally persistent so the cumulative impact may be significant over seasonal timescales. In this study we performed a set of field experiments to investigate the amplitude of mid-to-high frequency pressure changes as they vary with depth and permeability in a seasonal snowpack. We used four high-precision absolute pressure sensors to avoid bandwidth limitations encountered in a previous study using relative pressure sensors. We deployed the instruments in homogenous snow layers under windy conditions and captured monotonic decay of perturbation pressure energy with depth, thereby enabling calculation of spectral attenuation with depth. For a given wind forcing, surface perturbation pressure had greater amplitude than previously reported, accompanied by attenuation at high frequencies that was larger than theoretical predictions but in agreement with previous field measurements. Mid-frequency attenuation was lacking suggesting perturbation pressure at these frequencies can propagate deep into a homogenous snowpack. Applying these results to a simple vapor exchange model we theorize that mid-frequency pressure changes enhance mass flux between the snow and atmosphere in conditions with sufficient wind forcing and vapor pressure gradient.

4.2 Introduction

Wind generates turbulent eddies and topographically induced pressure fluctuations that initiate air exchange between the atmosphere and air space in permeable snow (Benson, 1962). Hydrostatic air exchange between the snow and atmosphere can theoretically enhance vapor exchange when there is a vapor pressure deficit between near-surface interstitial air and the air just above the snow surface.

The magnitude of vapor flux caused by hydrostatic pressure fluctuations is locally small and therefore difficult to measure directly so experimental evidence is scant. But this process acts over geographically vast regions so the integrated effect could be significant. The magnitude of vapor exchange enhancement caused by these pressure changes depends on the frequency and amplitude of the pressure fluctuations and how they attenuate with depth. Drake et al. (2016, hereafter referred to as D16a) found that high-frequency pressure changes preferentially decay with depth so the influence of high-frequency pressure changes is relegated to a thin surface snow layer. The absolute magnitude of pressure fluctuations at the snow surface as a function of wind characteristics is not known, however, nor is the attenuation of perturbation pressure for mid-to-low frequencies. In this paper, we investigate the relationship between wind forcing and pressure response in a homogenous surface snow layer with the goal of identifying the range of pressure fluctuations most likely to enhance surface vapor exchange.

The range of frequencies investigated in D16a was limited by the requirement of a reference pressure for the pressure sensors used in that study. In D16a, a reference pressure was required to intercompare measurements between relative pressure sensors. A common pressure sink used by all of the relative pressure sensors provided the reference pressure. The pressure sink must respond quickly enough that synoptic pressure changes do not exceed sensor measurement range yet slowly enough that high-frequency pressure changes are not inadvertently damped. These requirements limited the range of frequencies that could be examined with the relative pressure sensors used in D16a. In the set of experiments described in this paper, we instead utilized absolute pressure sensors with sufficient precision to capture the response of high-frequency pressure changes. Since these absolute pressure sensors are not range-limited for synoptic pressure changes, the range of detectable frequencies is limited rather by other factors such as time series length and stationarity of the snow state rather than instrumentation. Wind characteristics and the snowpack state may evolve over relatively short time periods so the absence of stationarity in the interaction between wind and the snowpack state constrains the frequency range that we analyze in this paper. With this time series constraint and the

constraint that the acquired time series must be subdivided and averaged to yield statistically significant results, we nevertheless extend the range of frequency analysis from 10s of seconds in D16a to ~ 2 minutes. In order to avoid the complicating influence of snow ice layers and stepwise changes in snowpack permeability, we deployed our equipment in a homogenous surface snow layer. The maximum depth for each deployment was therefore predetermined by snowpack layering state.

4.3 Method

To meet our goal of examining the influence of wind on interstitial pressure changes in snow we designed the setup shown in Fig. 4.1. A Campbell Scientific Irgason was mounted on a boom attached to a low-profile tower approximately 1 m above the snow surface. The Irgason transducer head was oriented into the wind 1.5 m upwind of the tower and leveled. 3-D wind speed and direction as well as CO_2 and water vapor concentrations were logged at 20 Hz on a Campbell Scientific CR-3000 logger. This logger was time-synchronized with a second CR-3000 logger by means of a GPS antenna and synchronizing software running on each logger. The second CR-3000 logged pressure measurements from four Paroscientific Model 216B pressure sensors at 20 Hz. These pressure sensors operated over a 300 hPa (800 hPa to 1100 hPa) range with 0.0001% resolution resulting in 0.03 Pa precision. Since the CR-3000 has only four high-speed serial ports and the GPS antenna required one of them, data from the fourth pressure sensor was acquired on a slower serial port resulting in intermittent data loss comprising approximately 0.02% of the record length. When performing spectral analysis, missing data was gap filled with data randomly chosen from nearby points in the time series. Inspecting the resultant spectra and noting that it did not unduly introduce artifacts such as spectral ringing verified this gap filling method.

Two-meter length tubing was attached to the pressure sensors at one end and then to a Y-fitting at the open end. A water trap was attached to one end of the Y-fitting to capture condensation that might otherwise drip into the pressure sensor inlet. A piece of tubing approximately 30 cm in length was attached to the other end of the Y-fitting for measuring the pressure signal. Before placing the open end of the tubing

in the snow a low-profile snowpit was excavated with a clean face oriented perpendicular to the prevailing wind. To ensure a tight fit, copper tube with outside diameter 2 mm smaller than the pressure sensor tubing was used to drill a horizontal channel approximately 20 cm long to a position directly under the sonic anemometer and the pressure sensor tubing was slotted into the open channel. After all tubing had been placed the snowpit was back-filled with surface snow and smoothed to match the original surface as closely as possible.

Pressure sensors were located downwind of the sonic anemometer on a foldup table that was pressed flat onto the snow to minimize their wind profile. With each deployment we collected data long enough to span a range of wind speeds and derive statistically significant results with a reasonable expectation that snowpack permeability did not significantly change over the data acquisition period. The tubing positions were verified at the end of each deployment by digging down to expose and remeasure the depth of the tubing ends. After each deployment we dug a partial snowpit in undisturbed snow several meters downwind of the pressure sensors so that we could characterize snowpack layering, snow density and snow grain characteristics. When conditions allowed we obtained bulk measurements of near-surface snow permeability with an acoustic permeameter as described in Drake et al. (2016b). Otherwise we estimated near-surface snow permeability by snow density and snow grain characteristics per Shimizu (1970).

We acknowledge the difficulty of obtaining statistically significant perturbation pressure measurements in a turbulent environment and heed the warning in Monin & Yaglom (1975) as quoted by Alberson et al. (1998):

‘‘*...the application of the theory of locally isotropic turbulence to the study of pressure fluctuations is slightly more questionable than other applications of the theory; it is possible that comparatively far regions of the flow make non-negligible contributions to the pressure fluctuations at a point.*’’

In this experiment, a sonic anemometer measured wind characteristics within the several-liter volume contained between transducer heads. Point pressure measurements were simultaneously acquired at different depths in the snowpack. Pressure perturbations propagate at the speed of sound, which is approximately 330

m/s (at sea level). So a pressure sensor acquiring data at 20 Hz would capture the integrated perturbation pressure field of all sources within a ~17-m radius volume above the sensor. Each measurement captures wind characteristics within a small volume and pressure changes within a much larger volume so we anticipate a poor correlation between high-frequency wind and high-frequency pressure changes. These physical limitations motivated us to mount the sonic anemometer closer to the surface than one might typically when acquiring near-surface wind characteristics. Bulk wind statistics vary less over the same domain so we anticipate an improved correlation between time-averaged wind characteristics (speed, direction, turbulence intensity) and pressure changes. The arrows in Fig. 4.2 relative to the geometry of our equipment schematically show the conundrum caused by the mismatch between wind and pressure changes.

4.4 Results

Previous experiments have shown that seasonal snow permeability tends to increase with decreasing snow density (Shimizu, 1970) so we chose three sites at different elevations to capture the in-snow response to wind for a broad range of snow permeability. Besides elevation, these sites were chosen based on criteria that emphasized exposure to wind, developed snowpack (1 m minimum depth), untrammeled snow surface and accessibility. We deployed the experiment at Hogg Pass, Oregon (elevation: 1468 m) for cases 1-5, Dutchman Flat SnoPark (sic) (elevation: 1905 m) for cases 6 and 7, and Storm Peak Lab, Steamboat, Colorado (elevation: 3220 m) for cases 8-14. The experimental setup described in the methods section was deployed 9 times for time periods ranging from 50 min to 50 h. In most cases the time period used for analysis was defined by time periods over which the wind maintained a prevailing direction. Longer deployments were subset to account for periods of data loss, step changes in wind direction and changes in snow conditions. Easy access combined with expensive equipment precluded unattended data acquisition with the upside that we could closely monitor snow conditions. Deployments are organized as cases in Table 4.1.

4.4.1 Perturbation pressure variability in homogenous layers

4.4.1.1 Effect of wind speed and averaging length on perturbation pressure

We first examine the effect of averaging time length on perturbation pressure magnitude for a representative case. In Fig. 4.3a we plotted the detrended 12-cm deep perturbation pressure from case 13 for 20-Hz pressure measurements minus the 1-second mean (orange) and 1-minute averaged pressure minus the 10-minute mean (blue). Longer averaging intervals yield larger pressure changes because lower frequency pressure changes have greater amplitude. Comparing wind speed in panel (b) with perturbation pressure in panel (a), we see that the absolute value of high-frequency perturbation pressure increases with wind speed but a correlation between mid-frequency perturbation pressure (1-minute fluctuations) and wind speed is less distinct. The positive correlation between increasing wind speed and increasing high-frequency perturbation pressure qualitatively agrees with a formula put forth in CB89 (Eq. 10), repeated here:

$$P = 0.0327\, e^{0.383M}, \qquad (4.1)$$

where P is perturbation pressure magnitude in Pa and M is wind speed in m-s^{-1} at 5-m height. Using wind speed measured by the sonic anemometer at 1-m height and estimating 5-m wind speed by assuming a log wind profile we used Eq. (4.1) to compute perturbation pressure, plotted in black in Fig. 4.3a. For this case and all other cases the perturbation pressure computed using Eq. (4.1) under-predicted measured values. Eq. (4.1) was based on 10-Hz data so it should yield values greater than the 20-Hz measurements yet they are smaller as shown in Fig. 4.3a. We also note that Eq. (4.1) describes a single-valued perturbation pressure value for a given wind speed whereas the data describe a distribution of perturbation pressures at a given wind speed.

The value of each constant used in the empirical formula shown in Eq. (4.1) depended upon the environmental conditions in which the data were acquired. We seek a method of diagnosing perturbation pressure that is more sensitive to the wind forcing and pressure response under varying environmental conditions that also

describes the distribution of perturbation pressures most likely to occur at a given wind speed. This distribution can then be used to estimate the effect of wind forcing on other processes, such as vapor flux enhancement by hydrostatic pressure changes. In Fig. 4.4 we plotted the distribution of perturbation pressure for case 4 using different averaging timescales varying from 1 s (Fig. 4.4a) to 1000 s (Fig. 4.4d) and note a Gaussian distribution that systematically flattens with averaging time. This flattening with averaging time behavior was observed for all cases and can be described by the standard deviation (σ_p) for a Gaussian distribution centered about zero:

$$f(P) = \frac{1}{\sigma_p \sqrt{2\pi}}\ exp\left(\frac{-P^2}{2{\sigma_p}^2}\right), \qquad (4.2)$$

where P is bin-averaged perturbation pressure. We applied a Gaussian curve fit to each averaging interval shown in Fig. 4.4 for each data set. The results are plotted in Fig. 4.5 with each symbol scaled by average wind speed for that deployment. In Fig. 4.5 the standard deviation of perturbation pressure increases with averaging interval, consistent with results previously discussed in regards to Fig. 4.3a. For the 1-s averaging interval data in Fig. 4.5 there is a high correlation between wind speed and bin-averaged pressure. This correlation decreases with increasing averaging interval and is not evident above the 100-s averaging interval, suggesting that high-frequency pressure fluctuations are driven by variations in wind whereas lower-frequency pressure variations are predominantly driven by other factors (such as synoptic scale pressure changes).

For the four deployments at the Hogg Pass site we plotted the 1-s averaging interval value for σ_p versus average wind speed (for that deployment) in Fig. 4.6. The dashed line in Fig. 4.6 is a power law curve fit to the data of the form:

$$\sigma_p = a\ (M)^b, \qquad (4.3)$$

where M is 3D wind speed and with fitting parameters $a = 0.055$ and $b = 2.558$. With Eq. (4.3), one can use the average wind speed for a given deployment to diagnose the standard deviation of perturbation pressure and then use Eq. (4.2) to generate an estimate of the perturbation pressure distribution for that wind forcing. An advantage of this method over Eq. (4.1) is that it diagnoses a distribution of perturbation pressure, which is more realistic than a mono-valued relationship between wind forcing and perturbation pressure response. For a given wind speed, Fig. 4.5 shows that the 1-s averaged perturbation pressure response was smaller at Dutchman Flat and Storm Peak Lab compared with Hogg Pass and suggests that the coefficients in Eq. (4.3) are site specific. A topic for future consideration is to attempt a scaling relationship that would generalize Eq. (4.3) for different sites.

In Fig. 4.7a bin-averaged perturbation pressure measured at the snow surface, computed as deviations of 20-Hz measurements from a 1-s mean, is plotted vs. wind speed. This high-pass filtering procedure limits the scale of motions that we examine to the highest frequencies resolvable by the sonic anemometer. Bin-averaged perturbation pressure is plotted against wind speed for one case from each deployment. All cases show a superlinear increase in perturbation pressure with increasing wind speed (panel a) and increasing scatter between cases as wind speed increases. Bin-averaged perturbation pressure for the same data is plotted against the square root of the vertical velocity variance (i.e. standard deviation, σ_w) in Fig. 4.7b. Note that bin-averaging by wind speed as in panel (a) yields a different range than bin-averaging by σ_w as in panel (b) because it is possible to have relatively large vertical velocity variance associated with low wind speed and vice versa. Data points are therefore arranged in different bins so bin-averaged perturbation pressure has a different range when plotted with respect to wind speed than it does with respect to σ_w.

Pressure measurements in cases 8 and 11 were taken at 19 cm depth, beneath a 1-cm thick ice lens, yet have a similar pressure response to wind forcing compared to other cases at the same location. This result shows that turbulence affects perturbation pressure and corresponding air movement even below an ice barrier. Cases 8 and 11 had the highest wind speeds, accounting for the largest perturbation

pressure magnitudes shown in Fig. 4.7. The large perturbation pressure offset between cases when σ_w is zero in Fig. 4.7b indicates that pressure perturbations are driven by horizontal as well as vertical components of turbulence so three dimensional wind speed is a better scaling factor to diagnose bin-averaged perturbation pressure than either horizontal wind speed or σ_w. The magnitudes of the bin-averaged pressure perturbations in Fig. 4.7 were very small (less than 1 Pa) for several reasons. As shown in Fig. 4.3a, the highest frequency perturbations had the smallest amplitude. When we bin-averaged these small amplitude perturbations to produce Figs. 4.7a and 4.7b, the infrequent, relatively large magnitude high-frequency perturbations are subsumed in the averaging process. We also note that case 8 was the only case with a bin-averaged horizontal pressure gradient that systematically increased with wind speed (not shown). Even so, the horizontal bin-averaged pressure gradient was very small, 0.09 Pa-m^{-1} at 10 m-s^{-1}, so it was barely discernable even with high precision instrumentation.

In Fig. 4.8 we plotted the distribution of pressure perturbations with increasing averaging lengths for the same data shown in Fig. 4.3a. Relatively few high-frequency perturbations shown in Fig. 4.8 have much amplitude (green line) whereas quite a few low-frequency pressure perturbations have significant amplitude (blue line). For high-frequency pressure changes, only the infrequent high amplitude events, corresponding to the tail of a Gaussian distribution, generate sufficient displacement to potentially affect vapor exchange at the snow surface. Not coincidentally, the cumulative distributions in Fig. 4.8 approach the cumulative distribution for a Gaussian distribution with shape dependent on standard deviation of the distribution. In the discussion section of this paper we examine the likelihood that perturbation pressure frequency and amplitude conspire to enhance vapor exchange between the atmosphere and snowpack.

4.4.1.2 Spectral attenuation dependence on averaging interval

In Fig. 4.9 we plotted the spectral attenuation for case 13 with an averaging interval of ~ 10 minutes (panel a) and ~ 2 minutes (panel b). For 10-minute averaging, frequency bandwidth is increased towards lower frequencies at the

expense of precision over the range of frequencies that are described in the 2-minute averaged spectra. At lower frequencies the spectral power at depth may slightly exceed the spectra power at a shallower position. This behavior is difficult to discern in Fig. 4.9 because the traces appear to converge at lower frequencies on these log-scale plots. The reason for this low-frequency energy crossover is not known although we offer several possible explanations. For one, perhaps this result is accurate and more energy within a narrow spectral band exists deeper in the snow than at a shallower depth. It has been shown theoretically (Colbeck, 1989), Waddington et al. (1996) and experimentally (Drake et al., 2016) that perturbation pressure energy decays with depth through a homogenous snow layer so the source of this energy is it not directly from above but rather has a horizontal component. Another possible explanation is that the resolution of our time series has been reached. Multiple averaging intervals are needed to increase the precision of the spectra and this limit is exposed in the low-frequency end of the spectra. Longer time series risk invalidating the assumption of stationarity in snow state, which could also corrupt the spectra at low frequencies. Finally, it is possible that we have reached the threshold of precision of the pressure sensors. The low-frequency phenomenon of deeper layers containing slightly more energy than shallower layers is not likely a windpumping signal because we expect the integrated perturbation pressure field to decrease exponentially with depth even if for particular frequencies it does not (CB89, Waddington, 1996). In any case, once the spectra no longer monotonically decay with depth we cannot discriminate an attenuation signal. For this reason, the frequency range for which we can discriminate attenuation is limited to the lowest frequency for which the attenuation remains monotonic with depth.

Our goal is to find an averaging interval long enough to capture data for which monotonic attenuation with depth is found and yet short enough to maximize precision. We found an averaging interval of 2 minutes captures the range of frequencies for which attenuation is monotonic for all cases. This is an improvement over D16a, for which the response time of the pressure sink limited the spectral resolution to 10s of seconds. In the next section we leverage the finding that high

frequencies monotonically decay with depth in homogenous layers to find the spectral attenuation with depth as a function of permeability.

4.4.1.3 Effect of snow permeability

The effect of snow permeability on the perturbation pressure field within the snow is evident by comparison of the spectra for high permeability case 1 (Fig. 4.9b) and low permeability case 7 (Fig. 4.10). These spectra were generated by averaging 2048-point FFTs of detrended 20 Hz pressure data resulting in a spectral bandwidth of 1.7 (~2) minutes. Even with weaker winds for case 1 (see Table 4.1), differential attenuation at high frequencies as given by the vertical spread between pressure traces is greater for case 1 than for case 7. Also, the instrument noise floor is reached at the 40-cm depth in high permeability case 1 but at 6-cm depth for low permeability case 7. This result indicates that high-frequency pressure perturbations more readily propagate into highly permeable snow and also attenuate more slowly with depth in high-permeability snow than in denser, low-permeability snow. This finding was reported in D16a but monotonic attenuation with depth is consistently evident in homogenous layers studied in this experiment whereas this finding was not consistently true for heterogeneous layering reported in D16a. Monotonic perturbation pressure decrease with depth allowed us to compute spectral attenuation with depth as a function of snow permeability.

4.4.1.4 Spectral attenuation for homogenous snow layers

The integral of the pressure spectra is equal to the pressure variance (Stull, 1991). For homogenous layers, pressure spectra logarithmically decrease with increasing frequency (Figs. 4.9 and 4.10) so the magnitude of the integrated pressure variance is dominated by the lowest few frequencies. Comparison of spectra in Fig. 4.9a using a 10-minute averaging interval with Fig. 4.9b using a 2-minute averaging interval shows the tradeoff between precision and bandwidth. The longer averaging interval in panel (a) resolves lower frequencies than the shorter averaging interval in panel (b) at the expense of precision in the resolved frequencies. Since the 2-minute

averaging interval resolves the low-frequency kink point at which attenuation is not resolvable, we use 2-minute averaging for subsequent spectral analysis.

We want to find the relative spectral attenuation over small changes in frequency so that we can decipher the frequencies for which relative spectral attenuation is strongest. This information is important for validating theoretical models that diagnose spectral attenuation of perturbation pressure in homogenous snow layers. In order to determine the relative attenuation over each narrow range of frequencies, Δf, we therefore need to normalize power for each Δf by the power for that same Δf at a shallower depth in the snow. The ratio of the power for these two depths gives the relative attenuation for that frequency band in that snow layer. In Fig. 4.11 we plotted the spectral attenuation for snow layers for high (case 1) and low (case 7) permeability cases. Note that for dense snow (in panel *b*), spectral attenuation is weaker than for case 1 but only because little high-frequency energy propagates into the snow in the first place (see also Fig. 4.10). Measureable attenuation is absent in the lowest frequencies shown in these spectra for all cases, including cases 8-12 for which an ice lens strongly attenuated high-frequency energy. Increasing spectral power above ~ 4 Hz in Fig. 4.11 in both panels is likely due to a combination of energy aliased from lower frequencies as well as a dearth of high-frequency energy present at the snow surface, causing subsequent attenuation to be small. Spectral attenuation for homogenous snow layers is summarized in Fig. 4.12 for all cases. The curves in Fig. 4.12 suggest a similarity relationship. We leave a derivation of this similarity relationship for future work.

4.4.2 Spectral attenuation for inhomogeneous snow layers

Although this paper examines perturbation pressure attenuation specifically in homogenous layers, we present a case study of heterogeneous layering for contrast. In Fig. 4.13 the spectra for an inhomogeneous snow layer (case 9) is plotted, for which data were acquired beneath an ~ 1-cm thick ice lens overlain by 8 cm of densified snow and 7 cm new snow. The effect of the ice lens was to strongly attenuate high frequencies and amplify mid frequencies relative other cases. The processes causing the behavior displayed in the case 9 spectra are beyond the scope of the paper. The

point is, this example highlights how changes in snow layers can complicate the relationship between permeability and snow layering and provides further justification for narrowing the scope of this paper to homogenous layers.

4.5 Discussion

4.5.1 Potential for sublimation enhancement

We can apply the above analysis to address the question of to what degree near-surface pressure changes enhance vapor exchange between the atmosphere and snowpack.

4.5.1.1 Vapor exchange due to synoptic pressure changes

We consider a simplified example similar to that given in CB89 in which the air above the snow is isothermal and imagine an adjustable mass on top of an atmospheric air column to simulate atmospheric pressure changes. Then the air column will expand and contract by Boyle's Law:

$$P_1 \tilde{v}_1 = P_2 \tilde{v}_2 \;\rightarrow\; \tilde{v}_2 = \frac{P_1 \tilde{v}_1}{P_2} \qquad (4.4)$$

Plugging in approximations that span a realistic range of synoptic pressure changes we have:

$$\tilde{v}_2 = \tilde{v}_1 \frac{1030mb}{990mb} = 1.04\, \tilde{v}_1 \qquad (4.5)$$

So the pressure and volume of air in the snow will change by upwards of 4% between high and low pressure systems. For small changes in pressure and height, air density and gravity can be considered constant so the hydrostatic equation dictates that a 4% change in pressure that equates to a 4% change in the thickness of the air layer in snow:

$$dp = -\rho g\, dz \;\rightarrow\; \frac{dp}{dz} = const\,. \qquad (4.6)$$

For a 1-meter deep snowpack a 4% depth change corresponds to only a 4 cm change in the hydrostatic depth of the air column. A rough estimate for the water vapor lost in one 3-day synoptic cycle for a 4-cm deep air layer with 50% relative humidity at 0 °C is given by the Clausius-Clapyron and ideal gas equations. The vapor pressure of the air layer above the snow in this case is:

$$e = e_s - e_a = \ 6.11mb - (0.5)(6.11mb) \approx 3mb, \qquad (4.7)$$

where we have assumed that the interstitial air is saturated per Pomeroy & Brun (2001). The number of moles of water vapor within the 4-cm deep column over a $1m^2$ area is:

$$n = \ \frac{e\tilde{v}}{RT} = \frac{(300Pa)(0.04m^3)}{(8.314\,Jmol^{-1}K^{-1})(273K)} = 5.29 \times 10^{-3}mol - m^{-2} \qquad (4.8)$$

This gives an areal mass of:

$$\frac{mass}{area} = (5.29\ x\ 10^{-3}mol - m^{-2})(18\ g - mol^{-1}) \qquad (4.9)$$
$$= \ 9.52\ x\ 10^{-2}g - m^{-2}$$

and a vapor loss rate of:

$$\frac{9.52\ x\ 10^{-2}g - m^{-2}}{3\ days} \approx \ \ 3\ x\ 10^{-2}g - m^{-2}day^{-1} \qquad (4.10)$$

At this rate, it would take over 40,000 years for a moderately dense, 1-m deep snowpack to sublimate by this process. So, it is clear that synoptic-scale hydrostatic changes have a negligible effect on vapor exchange for a seasonal snowpack.

4.5.1.2 Vapor exchange due to high-frequency pressure changes

Absent other forces, hydrostatic compensation of a 10 Pa perturbation such as that evident for 1-minute averaged data in Fig. 4.3a would cause a relatively large vertical displacement:

$$\frac{dp}{\rho g} = \frac{5\ Pa}{(1.1\ kg - m^{-3})(9.8\ m - s^{-1})} \approx 50cm \qquad (4.11)$$

However, the mean free path of a water molecule in the range of atmospheric pressures is on the order of tens of nanometers, so an impulsively driven water vapor molecule would have many collisions before it travelled far enough to affect water vapor exchange. Instead, we need to consider the magnitude of vertical displacements due to bulk hydrostatic adjustment above the snow. As CB89 suggested, each percentage change in surface pressure would lead to an equivalent percentage change in vertical displacement in the snowpack. For a 1-meter deep snowpack, a 10 Pa change would cause a bulk vertical displacement of:

$$\frac{(10Pa)(1m)}{(100000Pa)} = 0.1mm\ . \qquad (4.12)$$

This is a small displacement but it is on the order of the 0.24 mm aerodynamic roughness length of fresh snow (Gromke et al., 2011) so it is not unreasonable to speculate that hydrostatic changes of 10 Pa would move near-surface air to a height of nonzero wind speed at which point is could be entrained into the surface layer of the atmosphere. In this case water vapor exchange would be enhanced in the presence of a positive vapor pressure deficit gradient in the surface layer.

Synoptic pressure changes are too slow to impact vapor exchange between a seasonal snowpack and the atmosphere. On the other hand, high-frequency pressure changes are fast enough but appear to have insufficient magnitude to enhance vapor exchange. For example, the maximum pressure perturbation for 20-Hz data averaged over a 1 s interval in Fig. 4.3.a is 6 Pa (see also Fig. 4.8). Using Eq. (4.12), the

corresponding vertical displacement is 0.06 mm, which is too small to influence vapor exchange rate. We therefore consider middle frequencies for which it may be possible that pressure perturbations have sufficient magnitude and frequency to enhance sublimation. In Fig. 4.8 we plotted the accumulated fraction of data points for which the perturbation pressure equals a given value for case 13. We determined the deviation from the mean for a one-second interval using 20 Hz data, for a 10-second interval using 1-second averaged data, for a 100-second interval using 10-second averaged data, and for a 1000-second interval using 100-second averaged data. The data showed that perturbation pressure increased with averaging interval. In Fig. 4.8, nearly all high-frequency (e.g. 20-Hz) perturbations have amplitude below 1 Pa. As the averaging interval increased the fraction of data points that exceed a given threshold, say 5 Pa, increases.

4.5.2 A simple model of vapor exchange enhancement

We consider a simple model of vapor exchange between the atmosphere and surface that is controlled by surface/atmosphere vapor pressure deficit and by a mixing length scale. The mixing length scale describes the vertical displacement that vapor at the snow surface must translate to reach a height where wind is nonzero (such as the aerodynamic roughness height). In this simplified model, wind-generated pressure changes cause vertical air displacement that, if sufficiently large, give surface air sufficient vertical displacement that wind can mix out the saturated near-surface air, resulting in upward flux of water vapor. An example is demonstrated in Fig. 4.14 for a mixing length of 0.2 mm and distribution of pressure perturbations given in Fig. 4.8. At each frequency, we determined the fraction water vapor molecules with amplitude that exceeds the mixing length threshold. We then use Eqs. (4.7) through (4.10) to find the relative sublimation rate enhancement. For these cases studies, vapor flux enhancement was strongest for periods ranging from 300 s to 1400 s (~ 5-20 min). Higher amplitude turbulence and/or smaller aerodynamic roughness length pushes the range of maximum vapor flux towards shorter periods.

Surface/atmosphere water vapor exchange involves a complex set of processes not captured by this simplified model. These processes must be accurately

simulated in order for us to accurately estimate the pressure pumping contribution of water loss to the atmosphere in conditions of a positive vapor pressure deficit. The result of this simplified model is that water vapor flux enhancement by pressure pumping is feasible and the range of pressure changes that most significantly contribute to this process depends on wind forcing, which determines the spectral distribution of perturbation pressure.

4.6 Conclusions

We found that wind-induced, high-frequency pressure perturbations have a distribution with maximum amplitude that exceeds the value given in CB89 by an order of magnitude. D16a concluded that high-frequency pressure perturbations also attenuate more with depth than given by the theory in CB89. So the net result is that high-frequency pressure perturbations have greater magnitude than predicted but also attenuate more with depth than predicted rendering their zone of influence to a thin layer near the surface. For all cases, perturbation pressure had a Gaussian distribution over the range of analyzed averaging intervals (ranging from 1 s to 10000 s). The standard deviation of the perturbation pressure distribution increased with averaging interval. Bin-averaging perturbation pressure reveals functional relationships with wind speed and vertical velocity variance relative to a point cloud of high-frequency measurements. However, for a given wind forcing only a small fraction of pressure perturbations have significant amplitude. So the process of bin-averaging conceals the pressure perturbations with sufficient amplitude to affect exchange processes.

We deduce that in windy conditions mid-frequency (10s of seconds to minutes) pressure changes have sufficient magnitude to enhance vapor exchange between the atmosphere and snowpack when there is a vapor pressure deficit in the air above the snow. We refer to this increase in vapor exchange an “enhancement” because this process is not typically considered as a cause of vapor exchange. The magnitude of this vapor exchange enhancement depends on the distribution and magnitude of pressure changes, roughness length and vapor pressure deficit gradient. More study is required to better constrain these variables such that we can gauge the

magnitude of vapor exchange enhancement for various snow and meteorological conditions.

4.7 Tables

Table 4.1. Case numbers, associated dates and sensor heights relative to the surface for each deployment.

Case	Date	1-m Average Wind Speed $m\text{-}s^{-1}$	1-m Standard Deviation $m\text{-}s^{-1}$	Permeability	PT1 cm	PT2 cm	PT3 cm	PT4 cm
1	Feb 21, 2014	1.82	0.69	high	-60	-40	-20	0
2	Mar 1, 2014	1.36	0.83	mid	+105	0	-6	-6
3	Mar 8, 2014	1.64	0.86	mid	0	-3	-5	-45
4	Mar 14, 2014	2.51	1.27	mid	-40	-2	-4	0
5	Mar 24, 2014	0.65	0.42	mid	-1	-2	-5	-10
6	Apr 3, 2014	2.16	1.25	Low	-4	-8	-15	-30
7	Apr 4, 2014	2.68	1.30	Low	0	-3	-6	-12
8	Mar 23, 2015	5.92	2.42	Variable	-21	-19	-16	-17
9	Mar 23, 2015	rimed	rimed	Variable	-21	-19	-16	-17
10	Mar 24, 2015	3.48	1.02	Variable	-21	-19	-16	-17
11	Mar 24, 2015	5.99	2.02	Variable	-21	-19	-16	-17
12	Mar 24, 2015	rimed	rimed	Variable	-21	-19	-16	-17
13	Mar 26, 2015	3.68	1.04	High	0	-2	-7	-12
14	Mar 27, 2015	3.50	0.92	High	0	-2	-7	-12

4.8 Figures

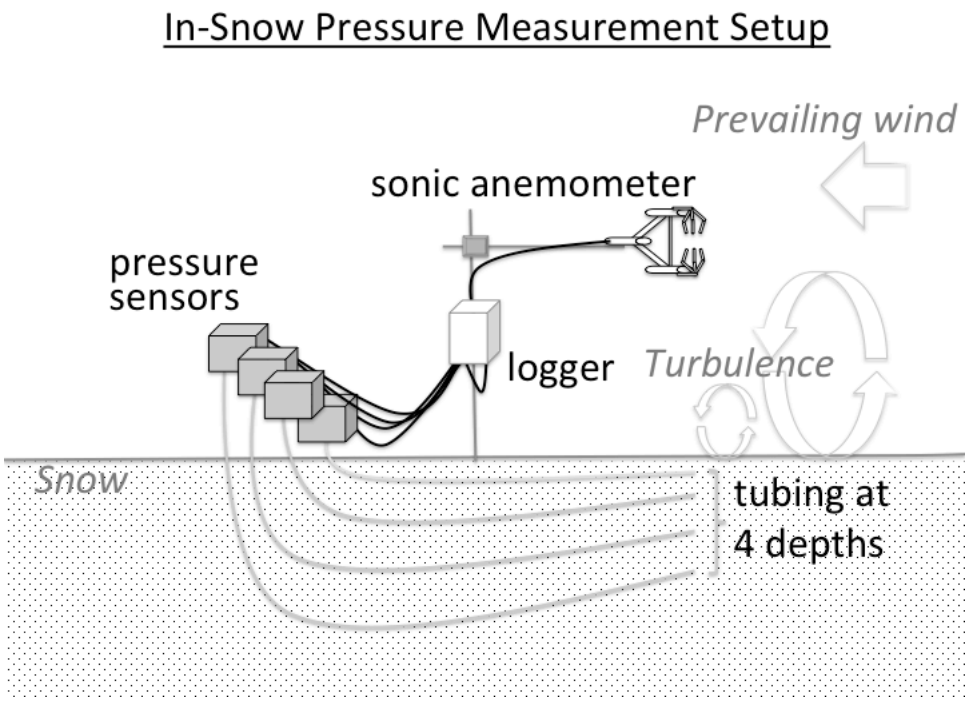

Figure 4.1. Schematic of experiment setup showing a sonic anemometer oriented into the prevailing wind and tubing for pressure sensors positioned in the snow below the sonic transducers.

Possible Noise Scenario

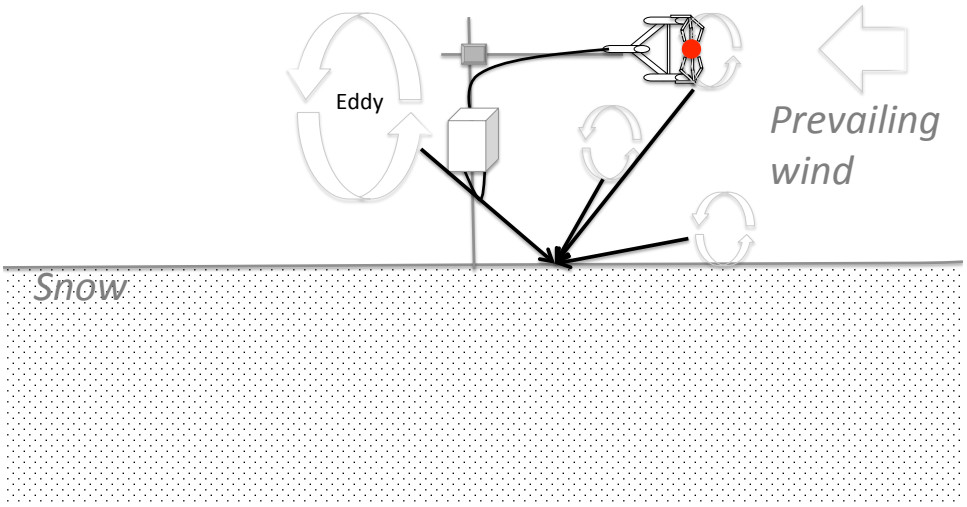

Figure 4.2. Schematic showing how wind is measured within a small volume (red dot) while pressure perturbations may emanate from turbulent eddies not co-located to the wind measurement.

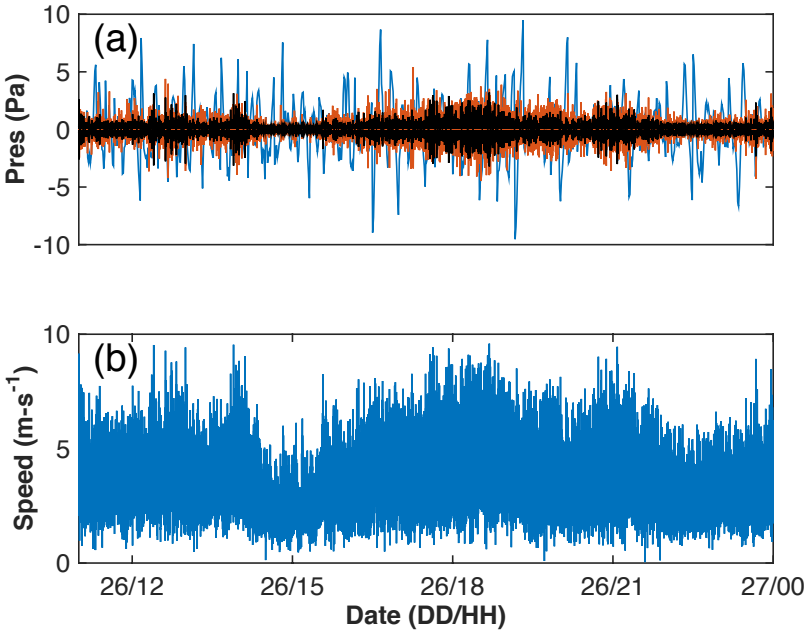

Figure 4.3. In panel (a) perturbation pressure for 20-Hz measurements relative to a 1-second mean (orange) and 10-second averages relative to a 1-minute mean (blue) measured at 12cm depth for case 13. Colbeck Eq. 10 is plotted in black. Wind speed at 20 Hz is plotted in panel (b).

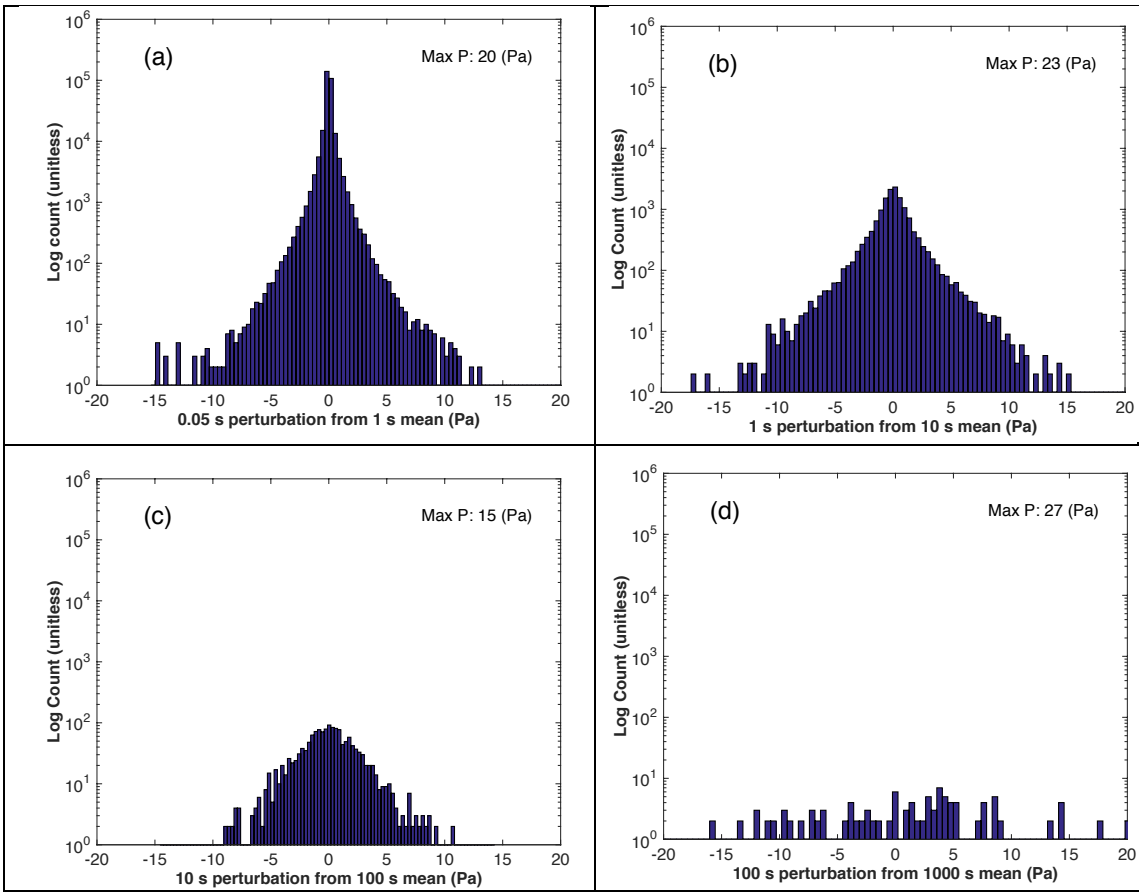

Figure 4.4. Log-scale histograms of perturbation pressure computed for 1-s (panel *a*), 10-s (panel *b*), 100-s (panel *c*), and 1000-s (panel *d*) averaging times for case 4. The single maximum pressure perturbation for each distribution does not change appreciably with averaging interval for case 4, however, the fraction of perturbations with large magnitude does increase with averaging time span for all cases.

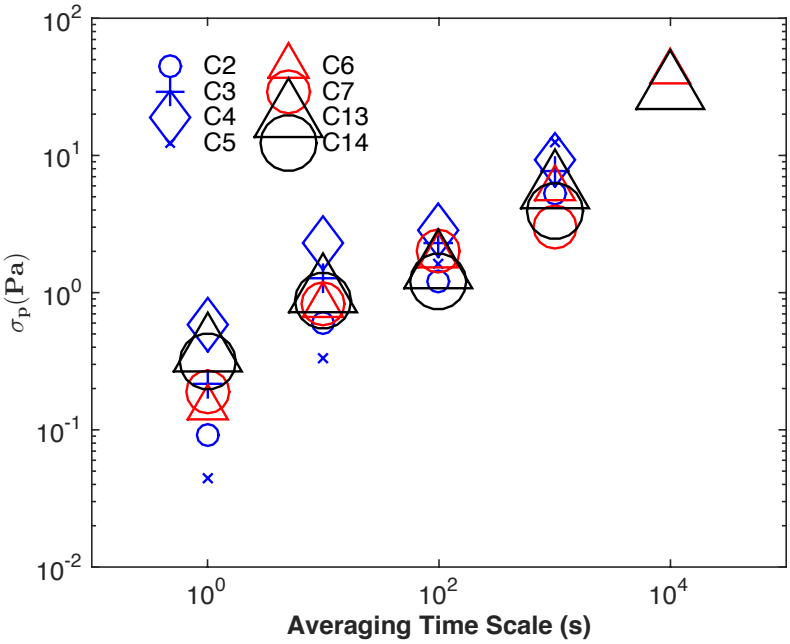

Figure 4.5. For each case, σ_p derived from a Gaussian curve fit is plotted vs. averaging time interval. Symbol size represents relative mean wind speed for each deployment. Wind speed correlates with σ_p for averaging time intervals less than 10^2 s.

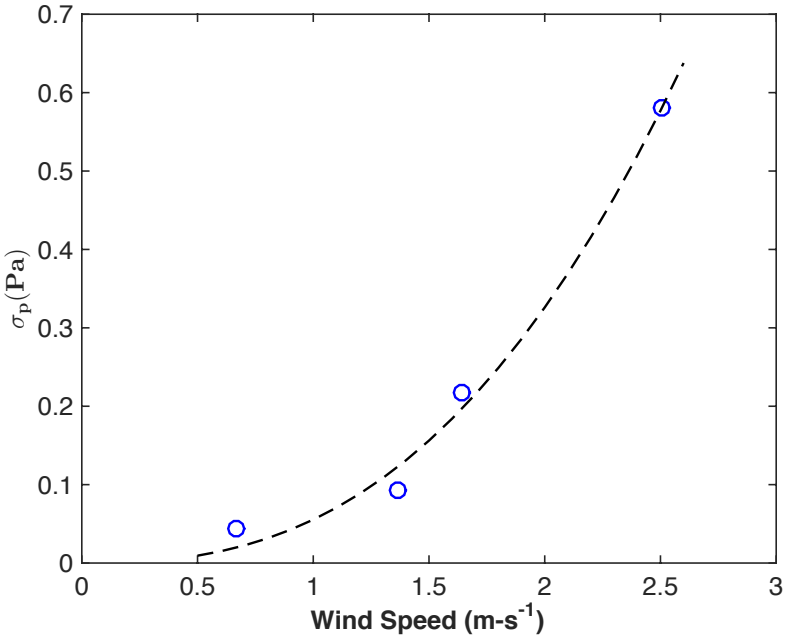

Figure 4.6. Using Hogg Pass cases 2-5, the standard deviation of perturbation pressure with 1-s averaging interval (leftmost points in Fig. 4.5) is plotted against wind speed. A power law curve given by the dashed line has the form given by Eq. (4.3).

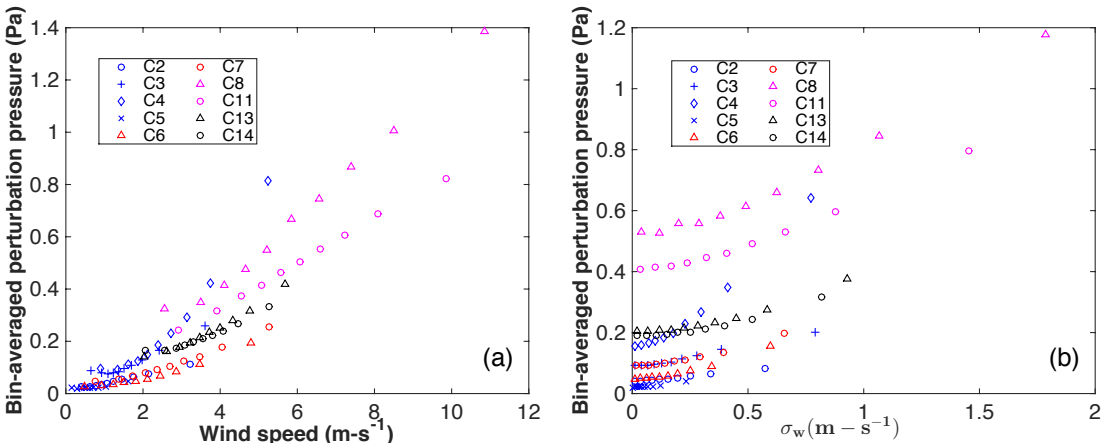

Figure 4.7. Surface bin-averaged perturbation pressure vs. bin-averaged wind speed (panel a) and vs. bin-averaged σ_w (panel b) for representative cases from each site. Cases are color coded by site with blue (Hogg Pass), red (Dutchman Flat) and black (SPL). SPL cases for which the pressure was measured under an ice lens are colored magenta.

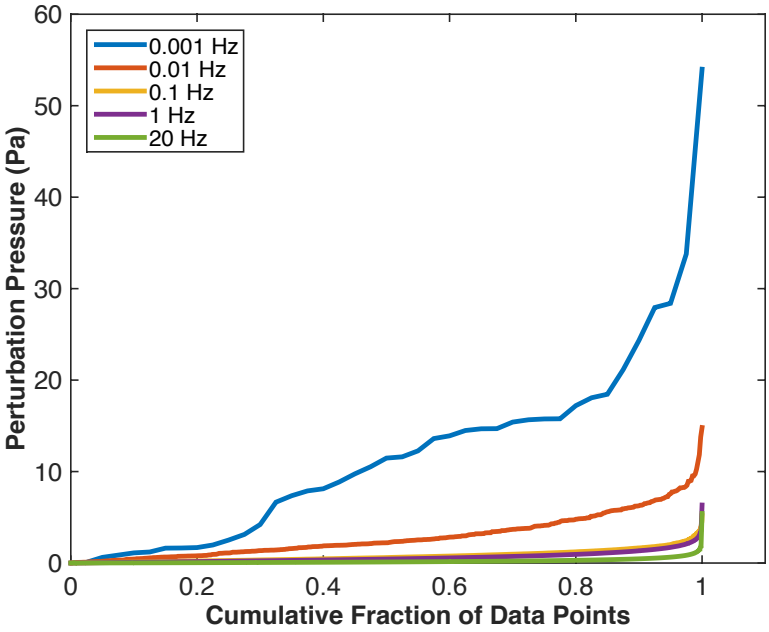

Figure 4.8. For case 13, cumulative distributions of perturbation pressure are plotted for each data frequency given in the legend. Longer averaging intervals have larger the pressure perturbations and therefore more data points above a given threshold.

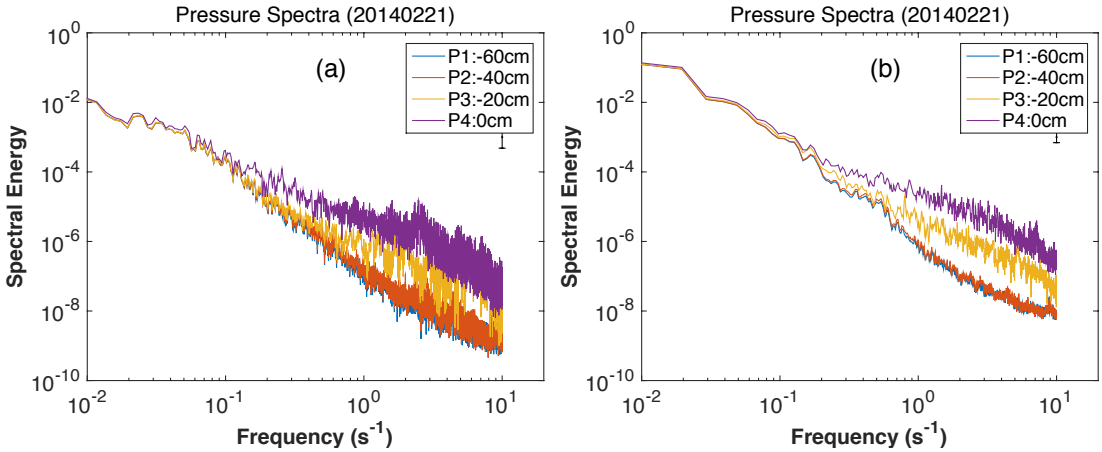

Figure 4.9. Comparison of spectra using a 10-minute averaging interval (panel a) with the same data (case 1) using a 2-minute averaging interval (panel b). A longer averaging interval spans more frequencies (at lower frequencies) but is noisier.

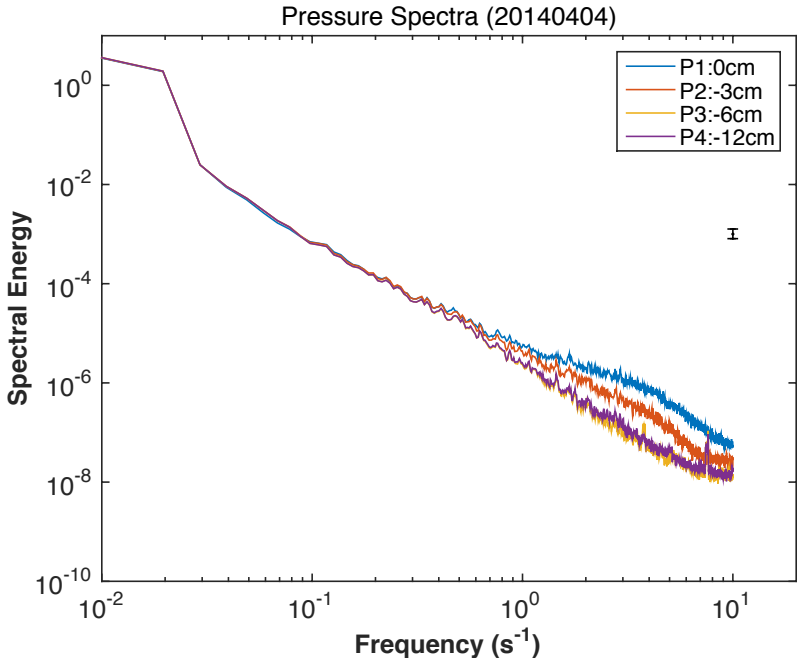

Figure 4.10. Compared with a high permeability case (Fig. 4.9), the spectra for this low permeability case shows less differential attenuation with depth because the bulk of high-frequency energy is attenuated at the snow surface. Relatively more energy is evident at 20-cm depth in Fig. 4.9 than at 12-cm depth for this low-permeability case.

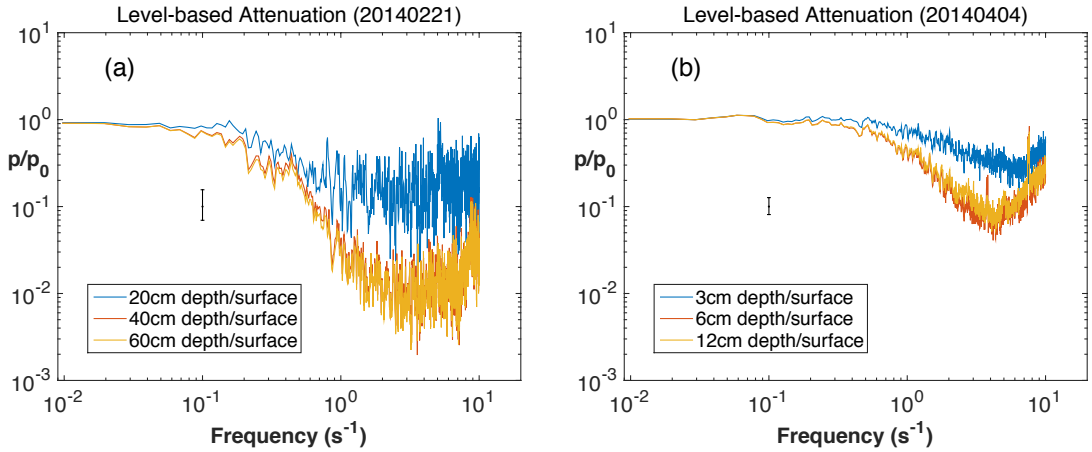

Figure 4.11. Spectral attenuation for snow layers defined in the legend for high-permeability (panel a) and low-permeability (panel b) deployments. Attenuation in panel (b) is less than in panel (a) because less energy passes into the snowpack.

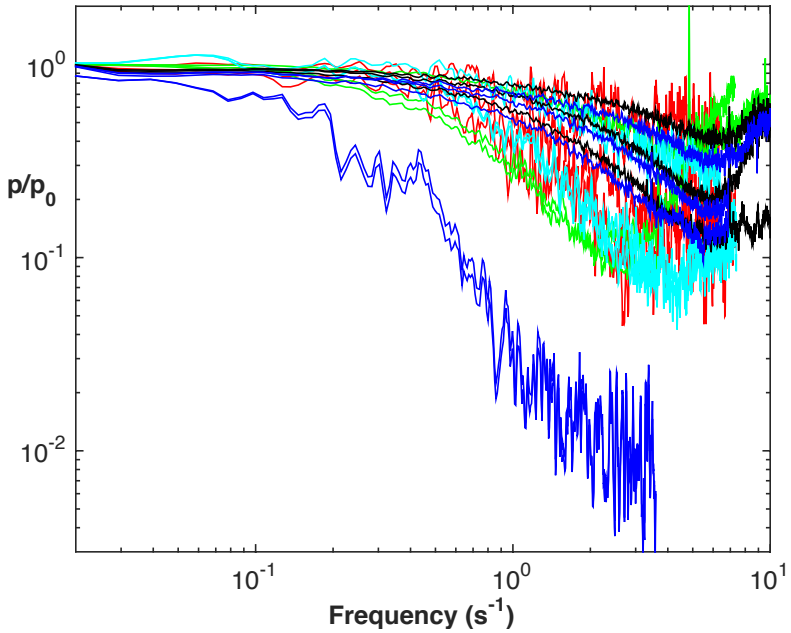

Figure 4.12. Layer attenuation summary for all cases indicates a similarity relationship with steeper spectral slope for deeper measurements in more permeable snow.

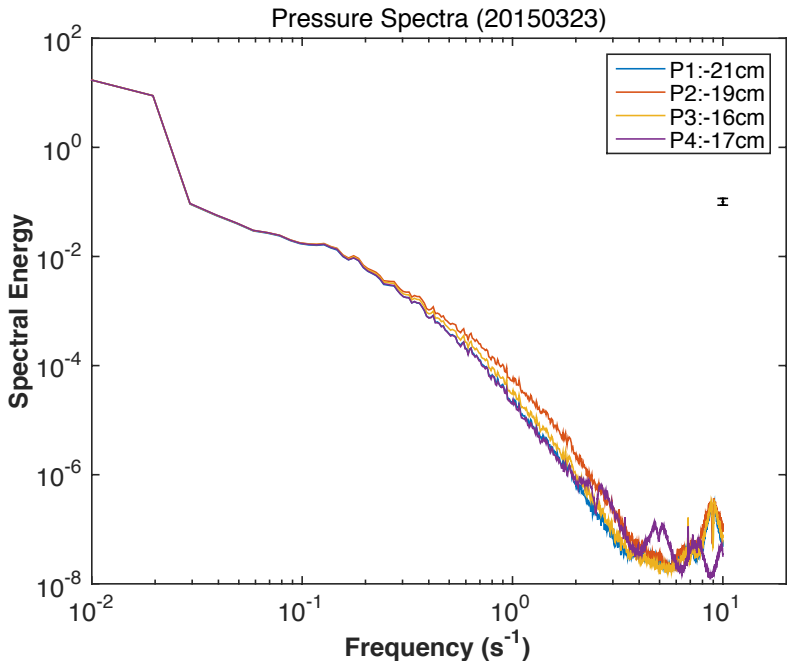

Figure 4.13. High frequencies are lacking in all four measurements below an ice lens even though the snow above the ice lens is highly permeable. Aliasing causes a slight increase in spectral energy near the Nyquist frequency (10 Hz).

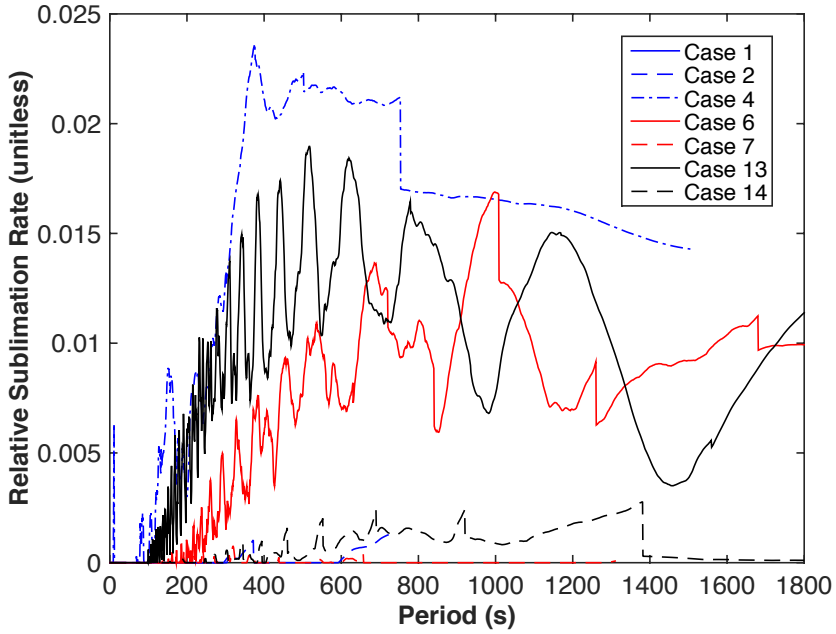

Figure 4.14. Model depiction of relative sublimation enhancement as a function of frequency for a 0.2 mm roughness length and 1% vapor pressure deficit.

5 A trace gas method of evaluating wind-enhancement of interstitial air movement in snow

A trace gas method of evaluating wind-enhancement of interstitial air movement in snow

S. A. Drake[1], J. S. Selker[2], and C. W. Higgins[2]

[1]College of Earth, Ocean and Atmospheric Sciences, Oregon State University.
[2]Biological and Ecological Engineering, Oregon State University.

To be submitted to:

Geophysical Research Letters

5.1 Abstract

Snow is a porous and permeable medium that regulates trace gas fluxes between the atmosphere and soil. Wind blowing over snow can enhance gas transport through interstitial pore space and increase gas exchange between the atmosphere, snow and subnivian soil. This process has important implications for mobility of chemically and radiatively active trace gases having sources under the snow, such as CO_2 and CH_4, and near the snow surface, such as HCHO and OH. However, processes driven by wind forcing as a function of snow properties are poorly constrained. In a set of field experiments we injected a dilute mixture of 1% carbon monoxide and nitrogen of known volume into a seasonal snowpack and measured plume evolution with a distributed array of thin film sensors. Measuring plume evolution as a function of wind forcing we found that the plume orients streamwise, even in dense snow, when the wind direction standard deviation is small. The plume centroid of mass propagates downwind along the prevailing wind direction suggesting a physical process that has a streamwise directional component that is not consistent with topographic forcing. We interpret this result as the effect of enhanced streamwise dispersion caused by turbulent features propagating downwind.

5.2 Introduction

Wind stimulates air movement through interstitial space in permeable seasonal snow (Bowling and Massman, 2011). However, the dominant physical process that generates air movement in snow under windy conditions is unclear. There are several competing hypotheses. One hypothesis states that wind blowing over surface roughness features generates localized pressure gradients and air in snow moves in response to these wind-induced pressure gradients (Colbeck, 1989). Experimental evidence supporting this hypothesis includes a publication by Albert and Hardy (1995), who measured a thermal response in snow to ventilation produced by a fan on the snow surface. They attributed the air movement to the quasi-stationary pressure field generated by the fan rather than by shear-driven turbulence. An alternate hypothesis by Clarke et al. (1987) states that turbulent pressure changes above the snow induce air movement in the snowpack. In a wind tunnel experiment

lacking roughness features, Sacratov and Sato (2000) concluded that turbulence enhanced air movement in snow. They did not specifically distinguish between shear-driven momentum exchange and shear-driven pressure changes as the process that causes air movement. Clifton et al. (2008) performed a wind tunnel experiment designed to isolate the effects of wind shear on ventilation. They concluded that shear directly affects only the top few millimeters of highly permeable snow and an even thinner layer in low permeability snow so wind does not "blow through the snow". They did not measure pressure changes in the medium and thus did not address the question of whether shear can create in-snow pressure gradients that would induce air movement.

Determining the dominant process that causes in-snow air movement is not merely a semantic exercise because the different processes can have different effects. If topographic features are the dominant cause of airflow in snow, circulation patterns develop in response to the amplitude and wavelength of the surface features, and snow-atmosphere exchange is enhanced within these circulation patterns (Colbeck, 1989; Albert, 2002). In contrast, on a flat snowfield lacking surface features, turbulently driven circulation patterns are transient. Turbulent eddies advecting in a preferred direction can produce transient streamwise pressure gradients that theoretically could induce streamwise airflow in snow, although this process has not been verified experimentally (see Fig. 5.1). As opposed to topographic features, turbulence will mobilize gas molecules broadly across the near-surface snowpack rather than preferentially in localized circulations. Since snow is permeable, larger-scale horizontal atmospheric pressure gradients do not stop at the snow surface so an in-snow horizontal pressure gradient could also induce Darcian flow aligned with the pressure gradient. Therefore, our intention is to address the question: does interstitial air movement have a directional response to wind and, if so, what is the dominant process causing this response?

Bowling and Massman (2011) found that molecular diffusion is the dominant process for CO_2 exchange through permeable snow. Results from a diffusion model assuming isotropic media with a diffusion constant of 2.56×10^{-5} $m^2 s^{-1}$ consistent with snow (from Huwald et al., 2012) are shown in Fig. 5.2a. An instantaneous

release at the origin spreads in time and the red dots mark the locations of point measurements at 15 cm, 30 cm and 45 cm from the origin. Half-hour time series of concentrations at these three locations are shown in Fig. 5.2b. These point measurements in time delineate "breakthrough curves" that have a distinctive shape with a rapidly rising concentration to a peak followed by gradual decay. In a purely diffusive environment the breakthrough curve of each successively distant point from the location is contained within curves defined by closer points as in Fig. 5.2b. Isotropic molecular diffusion spreads a plume in all directions but the centroid of mass remains stationary over time. On the other hand, advection translates the centroid. In Figs. 5.2c and 5.2d we have imposed an advective flow of 0.5 mm-s^{-1} oriented along the x-axis. The corresponding set of breakthrough curves in Fig. 5.2d shows that the curves cross at some point in time when advection is sufficiently fast. By comparing breakthrough curves derived from field experiments with simulations of diffusion we can determine the relative influence of non-dispersive processes. In this idealized description we do not account for snow heterogeneity, which enhances diffusion in regions of lower porosity, potentially leading to centroid displacement.

5.3 Materials and Methods

5.3.1 Instrumentation

We chose carbon monoxide (CO) as a tracer because its molecular weight is very close to that of air, so it is nearly neutrally buoyant. Additionally, CO can be safely handled, has low background concentration and low water solubility. This latter consideration is important because snow grains are often coated with a thin film of liquid water, even at sub-freezing temperatures. Neutral buoyancy ensures that gravitational effects do not influence plume evolution. A mixture of 1% CO in 99% N_2 provided sufficient concentration for the sensor network yet even at this low concentration CO can cause insalubrious side-effects in large volumes, necessitating small volume releases. The measurement network was comprised of 28 thin-film Applied Sensor MLC carbon monoxide sensors with detection range spanning four orders of magnitude (from 0.5 to 500 ppmv). To measure CO gas at well-known

positions in the snow, seven CO sensors were mounted in 15-cm intervals on each of four tapered poles. The poles were inserted into the snow at predefined positions forming a regular sensor grid. Silicone tubing strung down the center of each pole to an outlet opposite the CO sensors provided a means to deliver the CO gas to a well-known position in the snow. This same system was also used in Huwald et al. (2012), and we refer readers to that document for a thorough explanation of materials, manufacturing and wiring requirements.

Data from the 28 CO sensors were acquired on two synchronized Campbell Scientific CR-1000 loggers at 1-minute intervals. Release volume was measured with an Aalborg GFM17 Mass Flowmeter (range 0-15 SLPM) for cases 1 through 12 and with a Precision Sample Magnum Series 500 ml gas tight syringe for cases 13 through 15. The CO gas was delivered fast enough relative to the 1-minute measurement interval to approximate an instantaneous release. During each deployment four snow poles were arranged in either a vertical or horizontal orientation as shown in Fig. 5.3 such that we could capture either horizontal or vertical dispersion characteristics in snow with a given deployment. A Campbell Scientific Irgason ultrasonic anemometer captured 3D wind components at 20 Hz. One-minute averages were computed during post-processing the high-frequency data.

5.3.2 Site description

The system was deployed at three locations: Santiam Pass, Oregon (elevation: 1468 m); Dutchman Flat SnoPark, Oregon (elevation: 1905 m); and Storm Peak Lab (SPL), Mt. Werner, Colorado (elevation: 3220 m). These sites span a range of wind forcing and snow permeability regimes. The Santiam Pass and Dutchman Flat sites were nearly flat, while the SPL site was perched on a hill that sloped to the west (~ upwind) at our location. For each deployment we first setup a low-profile tower and mounted and leveled the sonic anemometer with the sonic transducer head oriented into the prevailing wind. During setup we were careful not to disturb the snow on the windward side of the tower. We carefully dug a low-profile snowpit, exposing a clean face into which we pushed the poles. Horizontal placements (arranged in a horizontal plane) required a shallower, broad snowpit whereas a narrow, deep snowpit sufficed

for vertical placements (placed horizontally but stacked vertically). Once the poles were placed, we backfilled the snowpit with fresh snow and smoothed the surface to match the surrounding, undisturbed snow level. AS-MLC CO sensors are both temperature and humidity sensitive so we allowed ~ a half hour for the temperature of the sensors to equilibrate with their environment before the initial release. Huwald et al. (2012) noted leakage around the pole perimeter that manifested as enhanced dispersion along the pole axis for some releases that was exacerbated in low-density snow. We also observed indication of minor leakage for some cases but most cases were performed in relatively high-density snow that seated snugly against the pole minimizing leakage.

5.3.3 Analysis methods

We used two methods to analyze the results. First, we applied calibration coefficients to voltage measurements and derived concentration for each sensor at each time step. Using a solution of the advection/diffusion equation for a point source in a horizontal velocity field then gives diffusion evolution:

$$C(x,y,z,t) = \frac{M}{4\pi t\sqrt{4\pi t D_x D_y D_z}} \exp\left[-\frac{\left((x-x_1)-Ut\right)^2}{4tD_x} - \frac{((y-y_1)-Vt)^2}{4tD_y} - \frac{(z-z_1)^2}{4tD_z}\right] \quad (5.1)$$

If we assume horizontal snow homogeneity (constant $D_{x,y}$) then we can differentiate Eq. (5.1) with respect to time and set this result equal to zero to find the streamwise advection velocity:

$$\sqrt{U^2+V^2} = \sqrt{\frac{r^2-6Dt_{MAX}}{t_{MAX}^2}} \quad (5.2)$$

for zero wind velocity:

$$D = \frac{r^2}{6t_{MAX}} \qquad (5.3)$$

Eq. (5.3) permits calculation of the horizontal diffusion coefficient as a function of the time required between the release time and the maximum measured concentration at each sensor location assuming zero air velocity in snow. Non-zero interstitial air velocity manifests as an enhanced diffusion coefficient. We computed the diffusion coefficient for each sensor and subtract these values from those given by Eq. (5.3) for a diffusion simulation to derive a residual that is an approximation of wind-driven dispersion enhancement. This technique comprises the second analysis method and has the advantage that absolute concentration is irrelevant so the result is insensitive to error in sensor calibration.

5.4 Results

5.4.1 Deployment description

This analysis is based on 12 releases selected from 5 different snow conditions detailed in Tables 5.1 and 5.2. These data were culled from a larger data set comprising 24 releases in 10 different snow conditions. Quality control criteria causing exclusion of some data included weather-related equipment problems such as snow/rain/riming causing transmission loss for the sonic anemometer, excessive leakage around the release pole, leakage at a tubing fitting and excessive icing/wetting/temperature changes of CO sensors. The dual requirements that the CO sensors needed to be free of ice and also experience minimal temperature swings for optimal operation restricted deployments to no more than several hours. Between deployments the sensors were dried-out to return them to an optimal operational state. Before each deployment we opened the case containing the poles to allow their temperature to equilibrate with the air temperature and minimize thermally driven temperature swings upon placement that would affect concentration measurements. While preparing to deploy the equipment we would assess the prevailing wind direction so that we could insert the poles oriented approximately perpendicular to the prevailing wind direction.

5.4.2 Break-through curves

In Fig. 5.4a we plotted the results of a large volume release on April 19, 2014 (case 11) accompanied by low wind and high-density snow. The breakthrough curves are smooth and indicative of diffusion-dominated dispersion similar to Fig. 5.2b. A subtle but telltale advection signature of breakthrough curves crossing is evident in Fig. 5.4a as compared with Fig. 5.2b (molecular diffusion only) and Fig. 5.2d (molecular diffusion and advection). This result shows that an advection signature is evident even for dense snow. The breakthrough curve in Fig. 5.4b is indicative of a measurement transect further downstream of the release point as manifested by the more diffuse peaks and turbulence-roughened curves. The plume in this release is advecting at an angle to the pole geometry because the highest concentration is at the 75 cm position rather than the 45 cm position.

5.4.3 Time to peak concentration

In Fig. 5.5 we show three cases where we've plotted the time required to reach the maximum concentration for each sensor as given from Eq. (5.3). As previously mentioned, this method eliminates the requirement of calibrating the concentration and to some degree compensates for errors associated with changing temperature or state of the CO sensors. For each case, a wind barb placed at the release point shows the average wind direction over the release timespan. The plume in Fig. 5.5a is roughly circular as would be expected for a diffusion-dominated dispersion yet may show preferential streamwise dispersion. From this plot it is difficult to discern an advective signature and we address that topic below. Plume dispersion in Fig. 5.5b shows unambiguous streamwise alignment but again it is difficult to discern preferential downwind propagation of the plume. Fig. 5.5c shows preferential along-pole propagation near the release point transitioning to streamwise alignment with time. We associate the initial preferential dispersion along the pole axis to leakage around the pole perimeter and the later streamwise alignment due to the influence of wind. This leakage problem was noted in Huwald et al. (2012) and is an impediment to studying plume propagation in high permeability snow using pole-mounted sensors.

5.4.4 Centroid of mass

In a purely diffusive environment the centroid of mass remains stationary (Fig. 5.2a) but moves with the flow in an advective environment (Fig. 5.2c). We determined the centroid of mass location at each time step as an indicator of an advective signature. In Fig. 5.6 we plotted the position of plume centroid relative to release position for case 4. The red asterisk marks the release point and black dots mark sensor positions. Circles delineate centroid position for each minute and the circle diameter is a relative measure of the plume standard deviation. Centroid positions in Fig. 5.6 are plotted starting one minute after the release. We do not account for the mass that advects out of the measurement network because we lack measurements needed to simultaneously constrain the relative mass loss in the vertical direction relative to the horizontal direction. Instead, we assume that the centroid position in the horizontal plane is accurate over the short timespan between the initial release and the time at which mass starts to advect out of the measurement network.

Initial centroid position for case 4 is located approximately 10 cm from the actual release point. For large releases the sensor nearest the release point saturates and returns NaN values so this incorrect initial position is a manifestation of missing data. After the release the centroid propagates from the release position in a downwind direction for approximately 10 minutes. In this time period, some of the plume mass has propagated vertically out of the sensor network plane but has not yet passed horizontally outside of the grid (Fig. 5.5b) so centroid propagation reflects the direction of interstitial air movement. After ~ 13 minutes, the calculated centroid position is driven by the location of mass still in the horizontal plane and within the sensor network and the centroid of mass appears to stall. For the time span between minute 3 and minute 13 the center of mass advected 6 cm giving an average velocity of 1.0×10^{-4} m-s^{-1}, which is slightly slower than 1.2×10^{-4} m-s^{-1} reported by Huwald et al. (2012) for higher permeability snow. Except for case 10, this result is consistent with other releases and shows that the plume center of mass advects preferentially downstream. An ice layer just above the CO sensors in case 10 caused more complex dispersion pattern (not shown). We attribute the dispersion pattern in case 10 to enhanced flow along low-resistance pathways in the snow matrix.

Movement of the centroid of mass is plotted for case 2 in Fig. 5.7. For this case, the CO sensors were inserted horizontally and aligned in a vertical plane so that we could identify a preferred vertical component in plume dispersion. After the release the centroid of mass moved upwards initially. After approximately 10 minutes the upward movement stalled and the centroid of mass slowly drifted downwards. We interpret the downward motion due to unaccounted for mass loss out of the top of the sensor network giving the impression of downward motion. Preferential upward dispersion is consistent with both a diffusion coefficient that increases with decreasing density and also with wind driven ventilation. The centroid of mass translated 7mm in 8 minutes giving an advection velocity of 1.5×10^{-4} m-s^{-1}. The plume therefore moved upwards (at 1.5×10^{-4} m-s^{-1}), which was faster than it moved downwind (at 1.0×10^{-4} m-s^{-1}). The relative magnitudes of vertical diffusion vs. advection are indeterminate from these measurements, however, because the plume was slightly buoyant. That is, the molecular weight of air is about 29 g-mol^{-1} (depending on water vapor concentration) whereas the N_2/CO mixture had a molecular weight of 28 g-mol^{-1}.

5.5 Conclusions

Even in dense snow, advection can enhance plume dispersion below the snow surface. Over flat reaches with a prevailing wind, a subsurface plume aligns in a streamwise orientation suggesting turbulence rather than topography as the driving mechanism for enhanced dispersion in our case studies. Horizontal advection velocity was found as 1.0×10^{-4} m-s^{-1} for case 4, which was less than the 1.2×10^{-4} m-s^{-1} value found in a previous study in lower density snow. In low-density, well-ventilated snow an ice layer can inhibit dispersion in a preferred direction but wind-induced pressure changes still stimulate air movement along low-resistance pathways.

5.6 Tables

Table 5.1. Summary of cases used for this analysis. Wind speed is at 1-m nominal height. Layer snow density is the average snow density for the layer between the snow surface and picket depth.

Case Id	Date	Release Id	Orientation	Layer Snow Density kg m^{-3}	Average wind speed m s^{-1}
1	14 Mar 2014	R3	vertical	439	1.84
2		R4			1.72
3		R5			1.86
4	04 Apr 2014	R3	horizontal	249	2.33
5		R4			2.45
6		R5			2.57
7	19 Apr 2014	R4	horizontal	430	0.70
8		R5			0.34
9		R6			1.00
10	24 Mar 2015	R1	horizontal	Variable, ice layer	3.91
11	26 Mar 2015	R1	horizontal	227	3.26
12		R2			2.92

Table 5.2. Summary of snow picket orientation for each case.

Case Id	Date	Orientation	Picket Order	Picket Distance cm	CO Sensor depth cm
1 2 3	14 Mar 2014	vertical	P3, P2, P4, P1	19,19,19	10, 10, 24, 40
4 5 6	04 Apr 2014	horizontal	P3, P2, P4, P1	11.5, 13.5, 16	6.8, 7.0, 6.0, 6.8
7 8 9	19 Apr 2014	horizontal	P3, P4, P1, P2	15.0, 17.6, 17.0	9.0, 9.6, 9.0, 9.0
10	24 Mar 2015	horizontal	P1, P2, P3, P4	15.5, 14.5, 15.0	21, 19, 16, 17
11 12	26 Mar 2015	horizontal	P1, P4, P2, P3	19, 19, 18	18, 19, 19, 19

5.7 Figures

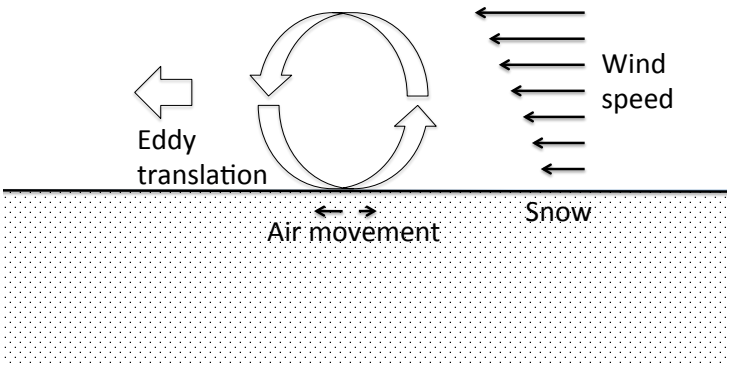

Figure 5.1. Idealized sketch showing preferential streamwise air movement in snow that was induced by a downwind propagating eddy.

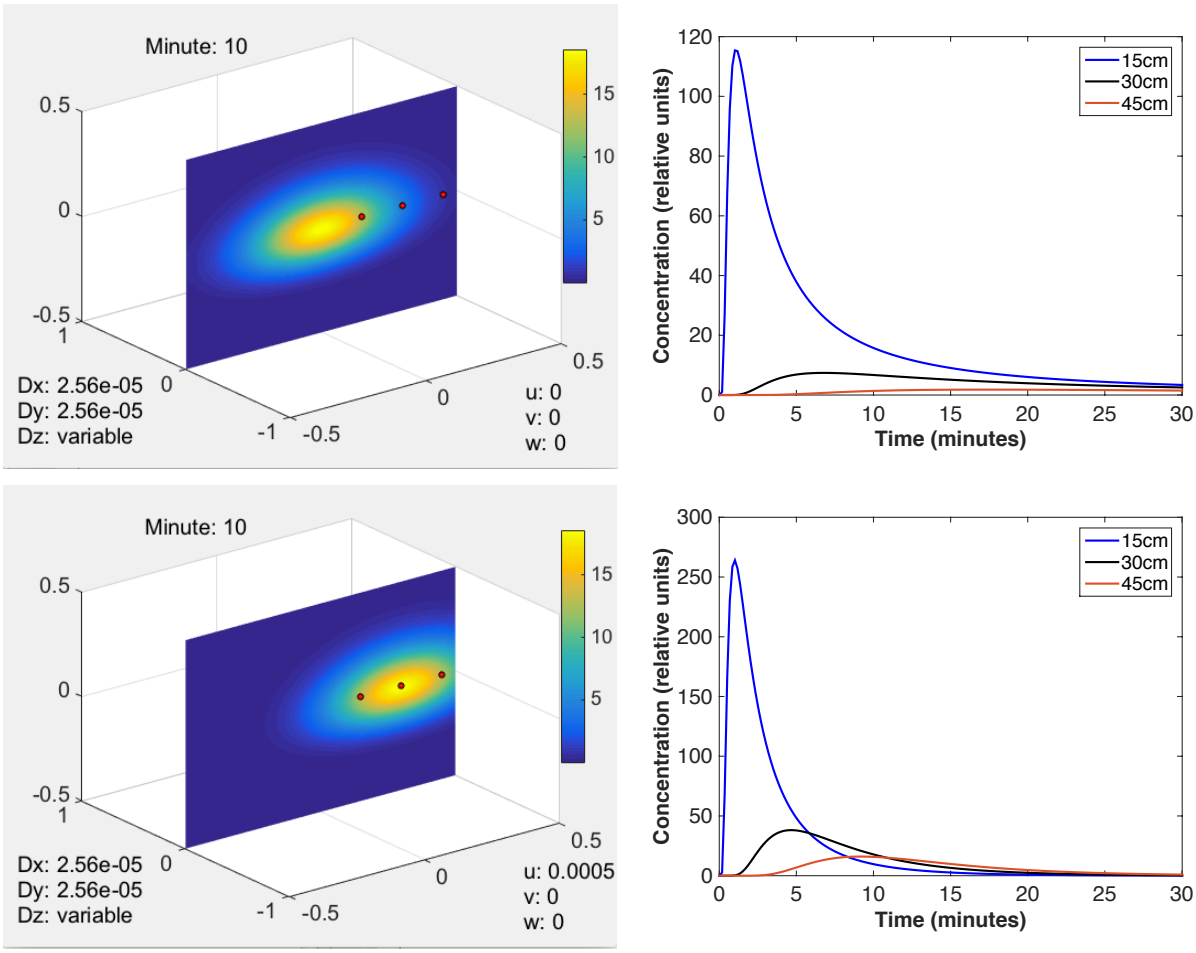

Figure 5.2. Simulated plume dispersion for a purely diffusive case (panel a, upper left) and the associated breakthrough curve (panel b, upper right) and for an diffusive/advective case (panel c, lower left) with associated breakthrough curve (panel d, lower right). For the diffusive/advective scenario, plume concentration is greater at the 30-cm position than the 15-cm position after 10 minutes.

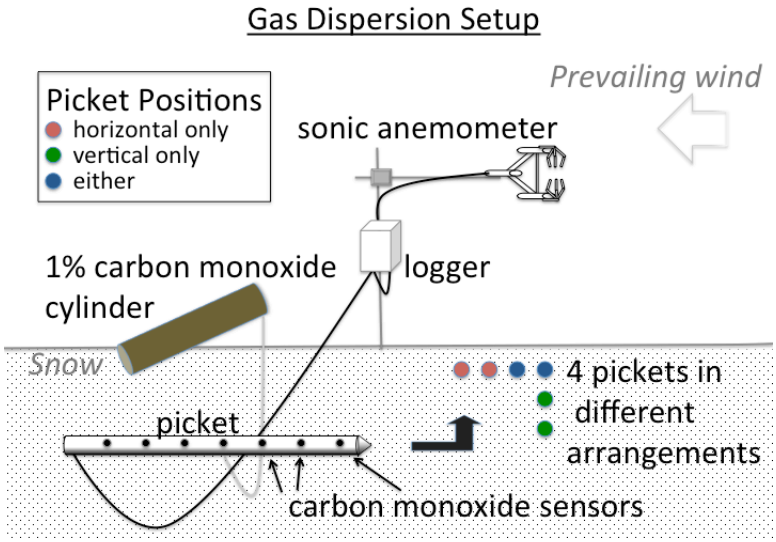

Figure 5.3. Diagram of the experimental setup showing the location of the sonic anemometer and snow poles.

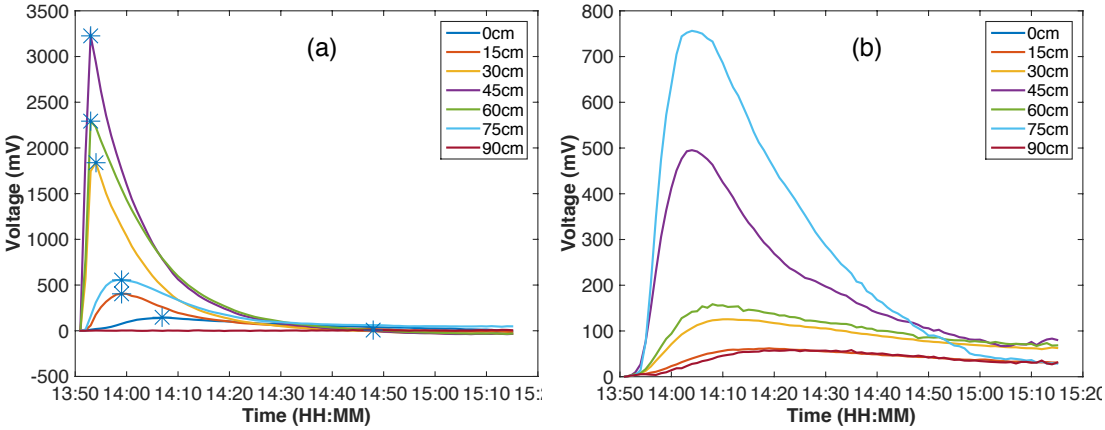

Figure 5.4. Near-field break-through curves for case 8 (panel a) and far-field break-through curves (panel b). Asterisks in panel (a) highlight time of maximum concentration at that position.

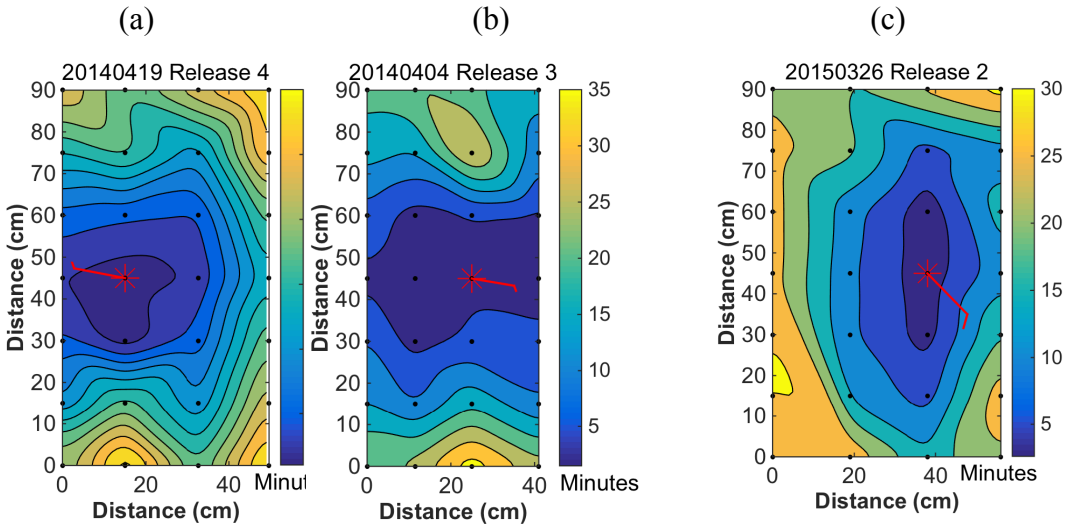

Figure 5.5. Time to maximum concentration color-filled by minutes from release time for case 7 (a), case 4 (b) and case 12 (c). An advection signal is weak in case 7 because the snow is denser, the poles are deeper and winds lighter than for cases 4 or 12.

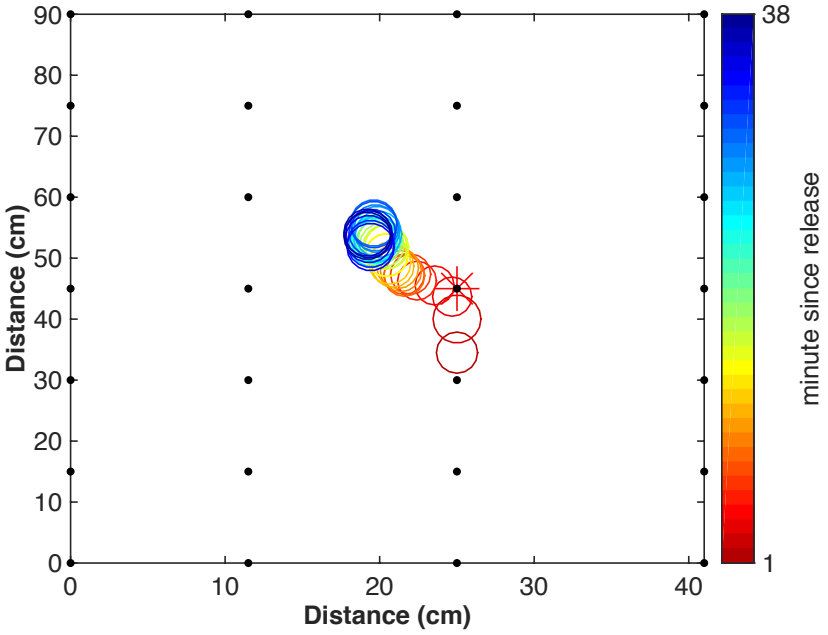

Figure 5.6. Centroid of mass plotted for case 4 (also in Fig. 5.5b), color-coded by minute since release. Release position is marked by a red asterisk and approximate sensor positions in this horizontal arrangement are marked as black dots.

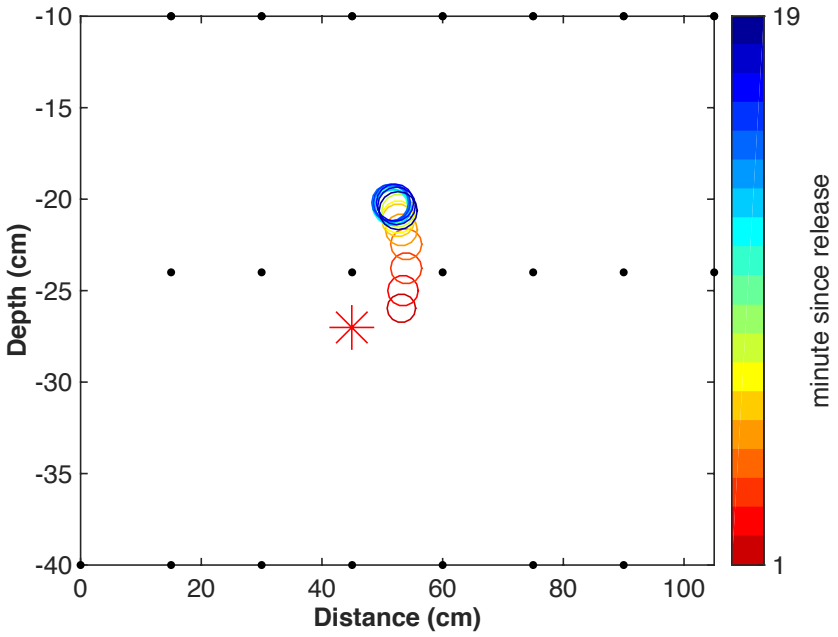

Figure 5.7. Centroid of mass plotted for case 2 color-coded by minute since release. Release position, located on the opposite side of the pole from the sensors, is marked by a red asterisk and approximate sensor positions in this vertical arrangement are marked as black dots.

6 Conclusions

6.1 Summary of Key Findings

Turbulent windflow over topographic features generates a quasi-static pressure field and a superimposed turbulent pressure field. In chapter 2 we isolated the quasi-static pressure field from the turbulent pressure field and examined the attenuation of each pressure field with depth in snow. We found that the topographically-generated, quasi-static pressure field attenuated with depth consistent with Albert (2002). The main thrust of this paper was to determine the attenuation with depth of turbulently generated pressure changes because they are more difficult to measure so their impact is less understood. We found greater attenuation of the turbulent pressure field with depth than either CB89 or WD96 predicted. The attenuation discrepancy between theory and measurements increased with frequency of the pressure change. The relative pressure sensors used in this experiment limited the range of frequencies that we could resolve, however. This paper shows a high-frequency problem for the CB89 and WD96 theories that may or may not extend to mid-to-low frequencies.

Since wind affects interstitial air movement through snow pore space, intrinsic permeability measurements are pertinent but acquiring these data is time consuming. To expedite permeability measurements we developed a prototype acoustic permeameter that measures the power of an emanated acoustic pulse and the backscattered power. This endeavor is described in chapter 3. Utilizing a low-frequency approximation developed by Moore et al. (1991), which relates acoustic attenuation with flow resistivity, we found theoretical and measured values for flow resistivity. The theoretical value for flow resistivity did not match the known flow resistivity of the test media but rather varied from the known values by smooth functions. We calculated these functions for two orientations of the permeameter microphone such that we could derive surface snow permeability in an expedited manner during field deployments.

In chapter 4 we applied lessons learned from chapter 2 to examine the frequencies for which hydrostatic adjustment could enhance vapor exchange between the atmosphere and interstitial pore space in snow. One of the lessons learned in

chapter 2 was that snow layering strongly modifies the interaction between wind and the in-snow perturbation pressure field. For this reason, we concentrated our efforts on thinner, homogenous snow layers when measuring perturbation pressure attenuation with depth. Unlike the experimental design in chapter 2, the low-profile experimental design in chapter 4 reduced, as much as possible, flow modification caused by the equipment. This experimental methodology and utilizing high-precision absolute pressure sensors produced perturbation pressure measurements in snow of the highest quality to date known by the author. We found that high-frequency perturbation pressure has greater amplitude than predicted by a formula relating wind speed with perturbation pressure given in CB89. Consistent with the findings in chapter 2, we found that attenuation of high-frequency pressure perturbations is also greater than CB89 and WD96 predictions.

For the case studies examined in chapter 5, a smooth relationship between 3-component wind velocity was found and the spread of this function was attributed to differences in snow permeability and atmospheric state. From the spectral distribution of perturbation pressure we computed water vapor enhancement by each frequency assuming a mixing length threshold on the order of snow aerodynamic roughness length.

In chapter 5 we found that a neutrally buoyant plume released in the snow may align in a streamwise manner under conditions of a prevailing wind direction. Downwind translation of the plume centroid indicated that wind direction is evident in the flow direction in snow although enhanced upwind dispersion was also evident. Preferential upward vertical diffusion limited the timespan over which centroid position derived in a horizontal plane was indicative of the plume direction. We attribute the measured dispersion pattern to eddies that translate downwind slower than the wind speed although we did not directly measure these wind features.

6.2 Future directions

At the top of the list of future directions is the need to measure the relationship between wind forcing and the vertical profile of perturbation pressure in snow/firn. Long term (months to years) measurements are needed to extend the low-

frequency resolution and precision of perturbation pressure attenuation in snow. These measurements need to be acquired under conditions that maximize stationarity of the snow conditions to minimize convolution of changing snow conditions with spectral perturbation pressure response. With these measurements we could address questions regarding the role of wind in deep firn mixing in low accumulation zones. In turn, this knowledge could be applied to improving paleoclimate analyses using ice cores.

The snow permeameter prototype is a promising development that needs further refinement. Active acoustic sensing of snow is in its infancy and has promise to provide data that is more representative over a larger volume than current measurements that utilize small sample sizes. A logical improvement would be to apply lessons learned from the Kinar and Pomeroy (2015) device with those given in chapter 3. Presently, the Kinar acoustic sensor is optimized to determine snow/water equivalent (SWE) by detecting pore space fraction. Perhaps it could be adapted to also determine permeability.

Much needs to be learned about the process of vapor exchange between the snow and air above it. Straightforward application of Monin-Obhukov theory in chapter 4 indicates that it is feasible for hydrostatic changes in atmospheric pressure to enhance vapor exchange. This process is poorly understood, however, and even less is known about the more complicated process of turbulent exchange. Direct application of Monin-Obhukov theory to permeable media such as snow is awkward. The aerodynamic roughness length of snow is small but positive, indicating that wind speed should be zero some small distance above the snow. But the displacement length is negative (Clifton et al., 2008), indicating that wind propagates some small distance into the snow. These two measures are useful for specific circumstances but are incompatible when paired together in permeable media applications.

7 Bibliography

Albert, D. G.: Acoustic waveform inversion with application to seasonal snow covers, J. Acoust. Soc. Am., 109, 91–101, 2001.

Albert, D. G., Decato, S. N. and Carbee, D.L.: Snow cover effects on acoustic sensors, Cold Reg. Sci. and Technol. 52, 2, 132–145, doi:10.1016/j.coldregions.2007.05.009, 2007.

Albert, M. R.: Effects of snow and firn ventilation on sublimation rates. Ann. Glaciol., 35, 52–56, 2002.

Albert, M. R., Shultz, E. F. and Perron, Jr. F. E.: Snow and firn permeability at Siple Dome, Antarctica, Ann. Glaciol., 31, 353–356, 2000.

Albert, M. R., and Hardy, J. P.: Ventilation experiments in a seasonal snow cover, in Biogeochemistry of Seasonally Snow-Covered Catchments, edited by K. A. Tonnessen, M. A. Williams, and M. Tranter, Int. Assoc. of Hydrol. Sci. Press, Inst. of Hydrol., Wallingford, U. K., pp. 41–49, 1995.

Álvarez-Arenas, T. E. G., de la Fuente, S. and Gómez, I. G.: Simultaneous determination of apparent tortuosity and microstructure length scale and shape: Application to rigid open cell foams, Appl. Phys. Lett., 88, 221910, doi: 10.1063/1.2208921, 2006.

Arakawa H., Izumi K., Kawashima K. and Kawamura T.: Study on quantitative classification of seasonal snow using specific surface area and intrinsic permeability, Cold Regions Science and Technology, 59, 163–168, 2009.

Attenborough, K.: Acoustical characteristics of rigid fibrous absorbents and granular materials. J. Acoust. Soc. Am., 73, 785-99, 1983.

Bachelor, G. K.: Pressure fluctuations in isotropic turbulence. Proc. Camb. Phil. Soc., 47, 359-374, 1951.

Bader, H.: Der Schnee und Seine Metamorphose, Beitrag zur Geologie der Schweiz, Geotechnishe Serie, Hydrologie, Lieferung, 3, Bern, 1939.

Bartlett S. J. and Lehning M.: A theoretical assessment of heat transfer by ventilation in homogeneous snowpacks. Water Resour. Res., 47, W04503, doi:10.1029/2010WR010008, 2011.

Bender, J. A.: Air Permeability of Snow, Research report (U.S. Army Snow, Ice, and Permafrost Research Establishment), 37, 1957.

Bowling, D. R., and Massman, W. J.: Persistent wind-induced enhancement of diffusive CO2 transport in a mountain forest snowpack, J. Geophys. Res., 116, G04006, doi:10.1029/2011JG001722, 2011.

Bou-Zeid, E., Higgins, C., Huwald, H., Meneveau, C., and Parlange, M. B.: Field study of the dynamics and modelling of subgrid- scale turbulence in a stable atmospheric surface layer over a glacier, J. Fluid Mech., 665, 480–515, 2010.

Buser, O.: A rigid-frame model of porous media for the acoustic impedance of snow, J. Sound Vib., 111 (1), 71–92, 1986.

Chacho, E. F. and Johnson, J. B.: Air permeability of snow, EOS (Transactions of the AGU) 68: 1271, 1987.

Clarke, G. K. C., Fisher D. A. and Waddington, E. D.: Wind Pumping: A Potentially Significant Heat Source in Ice Sheets, The Physical Shape of Ice Sheet Modelling, Vancouver Symposium, Int. Assoc. Hydrological Sciences Publ. no. 170, 169 – 180, 1987.

Clarke, G. K. C. and Waddington, E. D.: A three-dimensional theory of wind pumping, J. Glaciol., 37, 89-96, 1991.

Clifton, A., Manes, C., Ruedi, J. D., Guala, M. and Lehning, M.: On shear-driven ventilation of snow, Boundary Layer Meteorol., 126, 249–261, doi:10.1007/s10546-007-9235-0, 2008.

Colbeck, S. C.: Air movement in snow due to windpumping. J. Glaciol., 35, 209–213, 1989.

Conway, H. and Abrahamson, J.: Air permeability as a textural indicator of snow, J. Glaciol., 30, 106, 1984.

Courville, Z. R., Albert, M. R., Fahnestock, M. A., Cathles, L. M. and Shuman, C. A.: Impacts of an accumulation hiatus on the physical properties of firn at a low-accumulation polar site, J. Geophys. Res., 112, F2, doi:10.1029/2005JF000429, 2007.

Domine, F., Morin, S., Brun, E., Lafaysse, M. and Carmagnola, C. M.: Seasonal evolution of snow permeability under equi-temperature and temperature-gradient conditions, The Cryosphere, 7, 1915–1929, www.the-cryosphere.net/7/1915/2013/, doi:10.5194/tc-7-1915-2013, 2013.

Doutres, O. and Atalla, N.: A semi-empirical model to predict the acoustic behaviour of fully and partially reticulated polyurethane foams based on microstructure properties, in: Proceedings of the Acoustics 2012 Nantes Conference, Nantes, France, 23-27 April 2012, 1956-1960, 2012.

Doyle, G., Rice. C. W.: Influence of high-frequency ambient pressure pumping on carbon dioxide efflux from soil. Agricultural Forest Meteorology 124:193-206, 2004.

Drake, S. A., Huwald, H., Parlange, M. B., Selker, J. S., Nolin, A. W., and Higgins, C. W.: Attenuation of wind-induced pressure perturbations in alpine snow. J. Glaciol., In Press.

Drake, S. A., Selker, J. S., Higgins, C. W.: A low-cost acoustic snow permeameter, to be submitted to Geosci. Instrum. Method Data Syst., Submitted.

Elliot, J. A.: Microscale pressure fluctuations measured within the lower atmospheric boundary layer, J. Fluid Mech., 53, no. 2, 351-383, 1972.

Finger, D., Hugentobler, A., Huss, M., Voinesco, A., Wernli, H. R., Fischer, D., Weber, E., Jeannin, P. Y., Kauzlaric, M., Wirz, A., Vennemann, T., Hüsler, F., Schädler, B., and Weingartner, R.: Identification of glacial melt water runoff in a

karstic environment and its implication for present and future water availability. Hydrol. Earth Syst. Sci., 17, 3261-3277, doi:10.5194/hess-17-3261-2013, 2013.

Hardy, J., and Albert, D.: The permeability of temperate snow: Preliminary links to microstructure, Proc. Eastern Snow Conf., 50, 149-156, 1993.

Hutterli, M. A., Rothlisberger, R. and Bales, R. C.: Atmosphere-to-snow-to-firn transfer studies of HCHO at Summit, Greenland, Geophys. Res. Lett., 26(12), 1691-1694, 1999.

Huss, M., Voinesco, A. and Hoelzle, M.: Implications of climate change on Glacier de la Plaine Morte, Switzerland. Geogr. Helv., 68, 227–237, doi:10.5194/gh-68-227-2013, 2013.

Huwald, H., Selker, J. S., Tyler, S. W., Calaf, M., van de Giesen, N. C. and Parlange M. B.: Carbon monoxide as a tracer of gas transport in snow and other natural porous media. Geophys. Res. Lett., 39, L02504, doi:10.1029/2011GL050247, 2012.

Ishida, T.: Acoustic properties of snow, Low Temperature Science, Series A: Physical Sciences 20, 23–63, 1965.

Kerbrat, M., Pinzer, B., Huthwelker, T., Gäggeler H. W., Ammann, M. and Schneebeli, M.: Measuring the specific surface area of snow with X-ray tomography and gas adsorption: comparison and implications for surface smoothness, Atmos. Chem. and Phys., 8, 1261-1275, 2008.

Kawamura K., Severinghaus, J. P., Ishidoya, S., Sugawara, S., Hashida, G., Motoyama, H., Fujii, Y., Aoki, S. and Nakazawa, T.: Convective mixing of air in firn at four polar sites. Earth Planet. Sci. Lett., 244, 672–682, doi:10.1016/j.epsl.2006.02.017, 2006.

Kinar, N. J. and Pomeroy, J. W.: Determining snow water equivalent by acoustic sounding, Hydrol. Process., 21, 2623-2640. doi:10.1002/hyp.6793, 2007.

Kinar, N. J. and Pomeroy J. W.: SAS2: The system for acoustic sensing of snow, Hydrol. Process., 29, 4032-4050 doi:10.1002/hyp.10535, 2015.

Kino, N., Nakano, G. and Suzuki, Y.: Non-acoustical and acoustical properties of reticulated and partially reticulated polyurethane foams, Appl. Acoust., 73.2, 95–108, 2012.

Kyaw, T. P. U., Ideris, J., Matista, A., Rolston, D. E., Hsiao, T. C., Kochendorfer, J., Wharton, S., Pyles, R. D.: Pressure Pumping Effects on Soil Efflux Measurements of CO_2, Soil Carbon and California's Terrestrial Ecosystems Final Report, 2006.

Liston, G.E., and Sturm M.: The role of winter sublimation in the Arctic moisture budget, Nordic Hydrology, 35, no. 4., 325-334, 2004.

Maier, M., Schack-Kirchner, H., Aubinet, M., Goffin, S., Longdoz, B. and Parent, F.: Turbulence effect on gas transport in three contrasting forest soils. Soil Science Society of America Journal, 76, no. 5, 1518-1528, 2012.

Martinelli, M. Jr.: Physical properties of alpine snow as related to weather and avalanche conditions, U.S. Dept. Of Agriculture, Forest Service Research Paper RM-64, 1971.

Melon, M. and Castagnede, B.: Correlation between tortuosity and transmission coefficient of porous media at high frequency, J. Acoust. Soc. Am. 98, 1228, 1995.

Merbold, L., Steinlin, C. and Hagedorn, F.: Winter greenhouse gas fluxes (CO2, CH4 and N2O) from a subalpine grassland. Biogeosciences 10, no 5, 3185-3203, 2013.

Moore, H. M., Attenborough, K., Rogers, J. and Lee, S.: In-situ acoustical investigations of deep snow. Appl. Acoust., 33, 281–301, 1991.

Morse, R. W.: Acoustic propagation in granular media, J. Acous. Soc. Am., 24, 696-700, 1952.

Paterna, E., Crivelli, P. and Lehning, M.: Decoupling of mass flux and turbulent wind fluctuations in drifting snow, Geophys. Res. Lett., 43, doi:10.1002/2016GL068171, 2016.

Pinzer, B. R, Schneebeli, M. and Kaempfer, T. U.: Vapor flux and recrystallization during dry snow metamorphism under a steady temperature gradient as observed by time-lapse micro-tomography. The Cryosphere, 6, 1141–1155, doi:10.5194/tc-6-1141-2012 , 2012.

Rinaldi, A.P., Vandemeulebrouck, J., Todesco, M. and Viveiros, F.: Effects of atmospheric conditions on surface diffuse degassing. Journal of Geophysical Research: Solid Earth, 117(B11), 2012.

Severinghaus, J. P., Albert, M. R., Courville, Z. R., Fahnestock, M. A., Kawamura, K., Montzka, S. A., Mühle, J., Scambos, T. A., Shields, E., Shuman, C. A., Suwa, M., Tans, P., Ray, F. and Weiss, R. F.: Deep air convection in the firn at a zero-accumulation site, central Antarctica. Earth and Planetary Science Letters, 293, 359-367, 2010.

Shimizu, H.: Air permeability of deposited snow, Contrib. Inst. Low Temp. Sci. Ser. A 22, 1-32, 1970.

Sommerfeld, R. A. and Rocchio, J. E.: Permeability measurements on new and equitemperature snow, Water Resour. Res., 29, 2485–2490, 1993.

Sokratov, S. A., and Sato, A.: Wind propagation to snow observed in laboratory, Ann. Glaciol., 31, 427–433, doi:10.3189/172756400781820020, 2000.

Town, M. S., Warren, S. G., Walden, V. P. and Waddington, E. D.: Effect of atmospheric water vapor on modification of stable isotopes in near-surface snow on ice sheets, J. Geophys. Res., 113, D24303, doi:10.1029/2008JD009852, 2008.

Van Atta C. W. and Wyngaard, J. C.: On higher-order spectra of turbulence. J. Fluid Mech., 72, 13-38, 1975.

Waddington E. D., Cunningham J. and Harder S. L.: The effects of snow ventilation on chemical concentrations. Chemical Exchange Between the Atmosphere and Polar Snow, NATO ASI Series Volume 43, pp 403-451, 1996.

8 Appendix

8.1 Paroscientific 216-B Sensor Calibration

Sensor sensitivity was tested several times throughout the experiment campaign to verify that the sensor behavior did not change appreciably. I include only the last test on February 14th, 2016 in this document. For this test, all four pressure sensors were connected to the same outlet tubing to insure they experienced the same pressure changes over the 25-minute time period of the test (Fig. 8.1). The open tubing end was attached to a tripod at an elevation of 1m above the ground to measure turbulently-generated pressure perturbations. The standard deviation of the measurements over this time period was: P1=0.1192 hPa, P2=0.1189 hPa, P3=0.1191 hPa and P4=0.1191 hPa. In Fig. 8.1, pressure for P2 was offset by 0.05 hPa so that it did not overlap with the P4 trace but other sensor measurements have their natural, uncalibrated offset.

In this study we use pressure sensors to resolve pressure perturbations so an absolute calibration is not necessary. Nevertheless, I performed an absolute calibration to verify their operation over a large range of pressures. Data for this calibration were acquired with the CAPA array placed in a car while I drove from a mid elevation site (Baker City, OR, elevation: 1051m) to a high elevation site (Anthony Lakes Ski Area, elevation: 2164m) and then to Corvallis (elevation: 72m). The pressure sensors were placed inside the car and the intake caps were removed exposing them to atmospheric conditions and pressure perturbations within the car. These pressure perturbations were deemed minimal relative to hydrostatic changes as the elevation changed.

Data were acquired on March 29, 2015 on my return trip from Colorado. In Fig. 8.2, sensors P2, P3 and P4 are plotted against P1. From panels (a), (b) and (c), it is clear that sensors P1, P3 and P4 operate across a wide range of pressures without step changes or inconsistencies. However, as shown in panel (d), sensor P2 shows evidence of hysteresis on the order of several Pascals. This deviation is greater than factory specs. This behavior is due to residual water that settled into the intake tube on the last day of the Storm Peak Lab experiment. This water was not fully purged

until I returned to Corvallis. Subsequent sensitivity tests (next section) indicate that purging the intake tubing returned the sensor to its normal response characteristics. In any case, it would be prudent to test for hysteresis in the future, especially in circumstances where absolute pressure measurements are required. Time series plotted in Fig. 8.3 show the effect of water in the inlet tubing for sensor P2 relative to the other sensors.

8.1.1 Paroscientific 216-B pressure sensor sensitivity

In this experiment we measure very small amplitude pressure changes and need to be able to resolve the difference between a real measurement and sensor noise. This sensitivity experiment was designed to inter-compare instrument noise. On February 4th, 2016 in the NewAg Lab I placed the pressure sensors on a 5"-thick foam to minimize vibrations and interconnected the tubing so that all sensors would measure the same input pressure signal. I stuffed 80 PPI reticulated foam into 1 in. of the intake tubing for all of the sensors to partially attenuate background noise. Data was acquired on a data card the CAPA logger (CR3000) from approximately 15:00 to 18:45 and plotted in Fig. 8.4. The absolute pressure is not calibrated in Fig. 8.4 with the natural offset allowing one to view the four data traces. Even with foam attenuating the input pressure signal the effect of the building air conditioner on the input signal. The air condition turns off for the night at approximately 17:00. After that, intermittent disturbances introduce pressure fluctuations. For sensitivity analysis, I chose the time period between approximately 20:00 and 22:25, which corresponds to a range of time lacking overt pressure changes due to human or mechanical intervention.

For the time period 20:00-22:25, I subdivided the data into 8699 segments of 20 points each (corresponding to 1-second in time) and found the standard deviation independently for each of these segments. These standard deviation values were then averaged to obtain the noise level for each sensor. The results are shown in Table 8.1. The standard deviation of each sensor is ±0.052 Pa. This narrow range of standard deviation between sensors indicates that we do not need to perform statistics to compensate for differences between sensors. This result should be considered as a

conservative estimate because the background perturbation pressure field was not perfectly still. The zoomed-in image in Fig. 8.5 shows the magnitude of the noise over a narrow window around 21:00. It is clear from Fig. 8.5 that the noise level is much less than one Pascal.

8.1.2 Sensitivity to measured amplitude to tubing diameter

For one deployment at Steamboat Springs I placed the snow pickets just below a thick (~ 1 cm) layer of ice. Rather than leaving the free-end of the pressure sensor tubing exposed, it was attached to the 45-cm position on each snow picket. The spectra from this deployment showed that both high and mid-frequency energy was limited relative to data collected from other deployments. Since the tubing diameter on the snow pickets is much smaller (inside diameter: 3.45 mm) than the regular tubing (inside diameter: 6.35 mm), this sensitivity study is to determine whether the tubing diameter affects the measured pressure spectra.

On February 15th, 2016 I arranged 3 snow pickets as shown in Fig. 8.6. Pressure sensors and snow pickets were connected as: PT1-P1, PT2-P2+0.05 hPa, PT3-P3, P4 is attached to large tubing and is taped to PT1 in the picture. Only P2 has a wire over the inlet. The tubing ends were not collocated but were near enough in proximity that they captured very similar pressure changes, as time series in Fig. 8.7 indicates. As before, the pressure measured by P2 was offset by 0.05 hPa so that it did not overlap with the P4 trace but other sensor measurements have their natural, uncalibrated offset. The pressure spectra for P1, P2, and P3 show nearly identical traces to P4, indicating that tubing diameter did not unduly affect the measured pressure. This result suggests that high and mid-frequency energy missing in the Steamboat deployment was not caused by tubing diameter but was rather a real phenomenon.

8.2 Tables

Table 8.1. Pressure sensor standard deviations.

Sensor	Standard Deviation
P1	5.1244×10^{-4} hPa
P2	5.1358×10^{-4} hPa
P3	5.1571×10^{-4} hPa
P4	5.2212×10^{-4} hPa

8.3 Figures

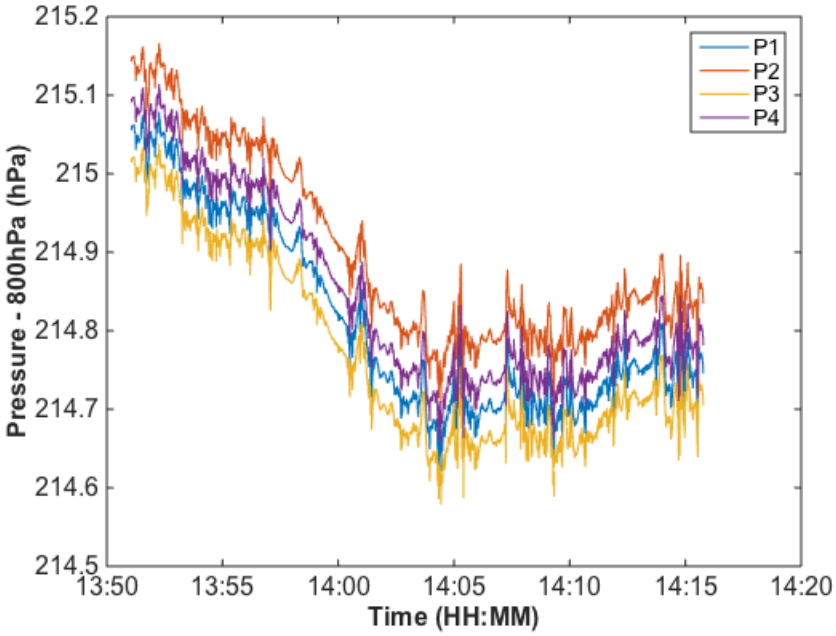

Figure 8.1. 25-minute time series of data acquired with four Paroscientific 216B pressure sensors with inlet tubing configured to measure a common source.

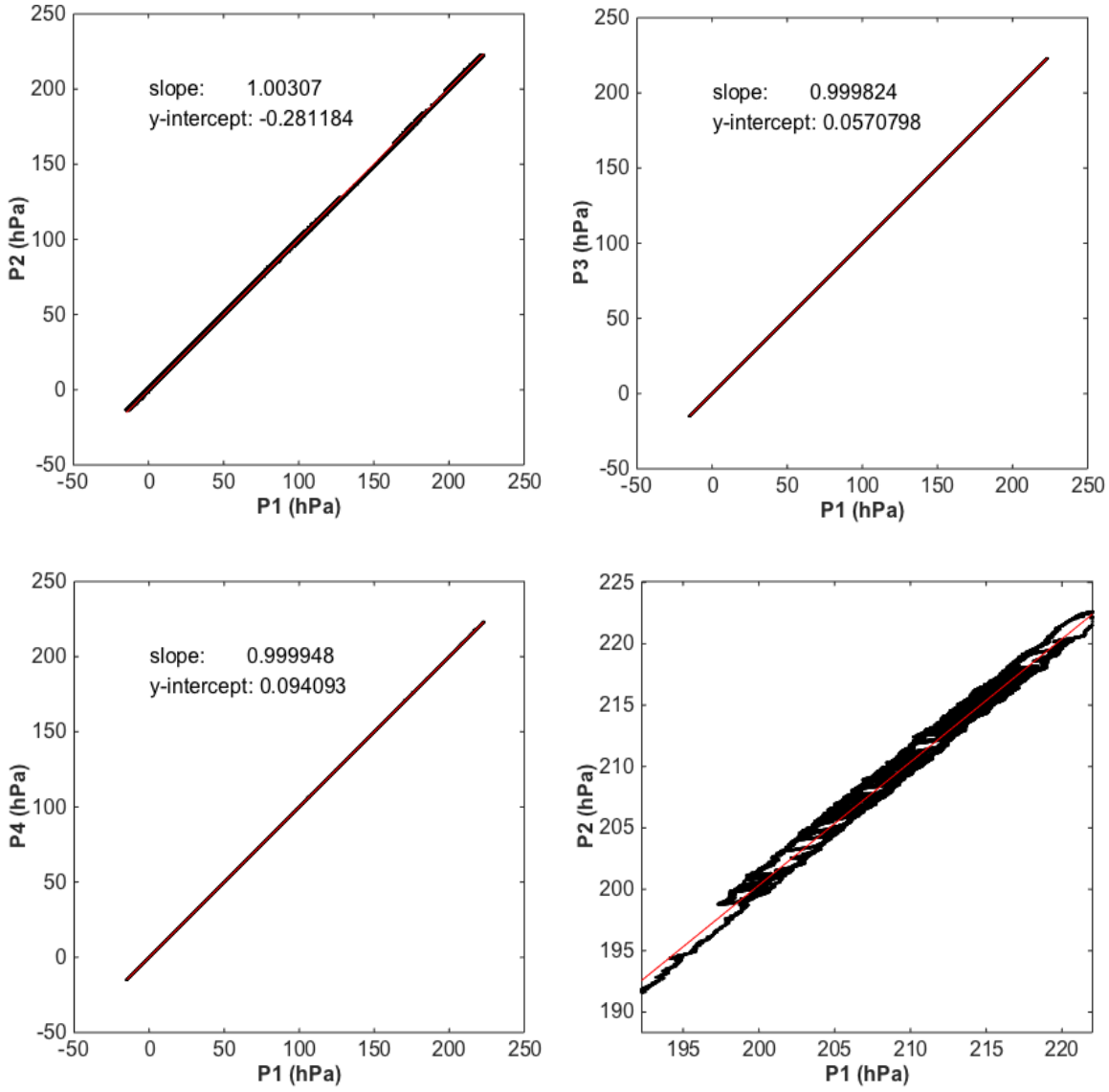

Figure 8.2. Comparison of Paroscientific 216B pressure sensors over a broad range of pressures (panels $a - c$). Panel (d) is a zoomed-in view of panel (a), showing the effect of a drop of water in the inlet tubing for sensor P2.

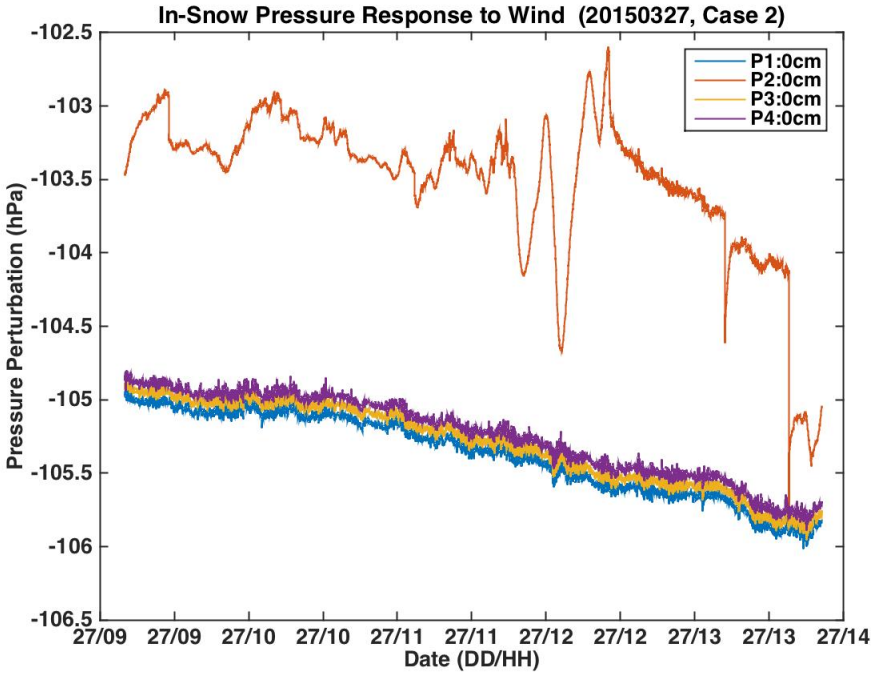

Figure 8.3. Time series showing the effect of a drop of water in the inlet tubing for sensor P2.

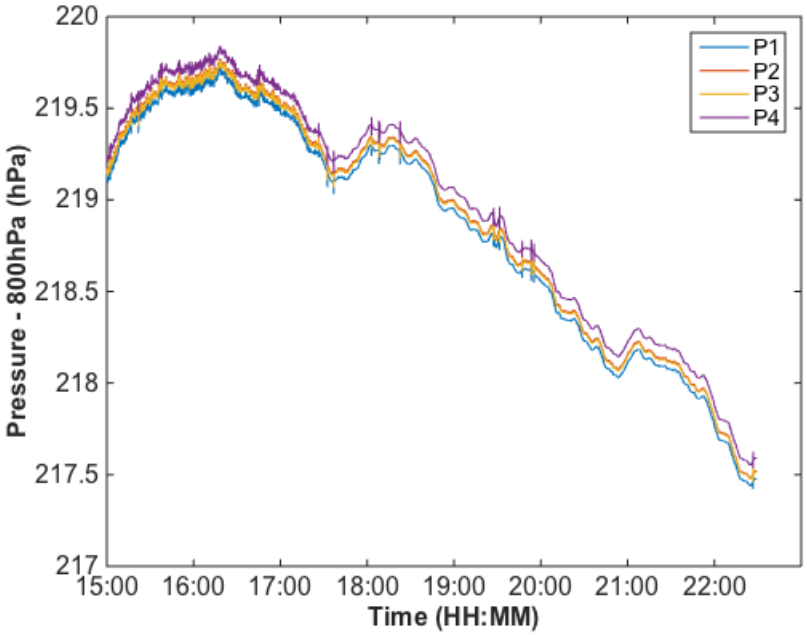

Figure 8.4. Time series of pressure data acquired overnight in the NewAg lab.

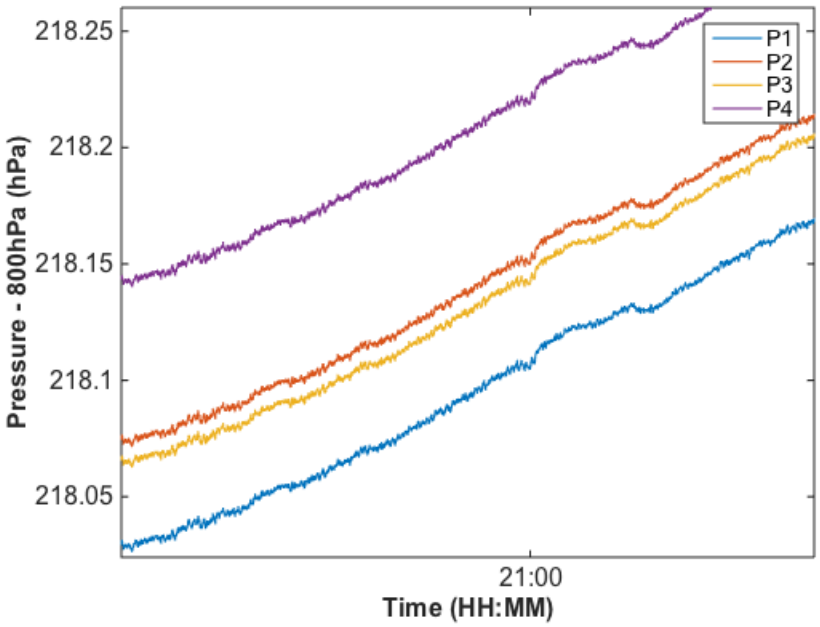

Figure 8.5. Short time series of pressure data shown in Fig. 8.4.

Figure 8.6. Arrangement of pressure sensor inlets for tubing sensitivity test.

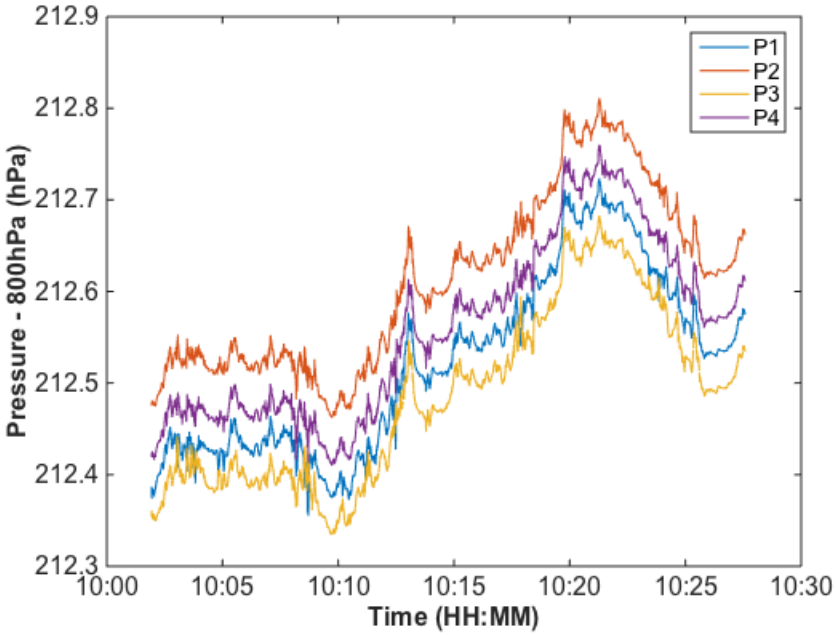

Figure 8.7. Time series acquired with pressure sensor inlets as shown in Fig. 8.6.